

# Multimodal eye's optical quality (MEOQ)

Zur Erlangung des akademischen Grades eines

## **DOKTOR-INGENIEURS**

von der Fakultät für

Elektrotechnik und Informationstechnik  
des Karlsruher Instituts für Technologie (KIT)

genehmigte

## **DISSERTATION**

von

M.Sc. Carlos Enrique García Guerra  
geb. in Mexiko-Stadt, Mexiko

Tag der mündlichen Prüfung: 29.07.2016

Hauptreferent: Prof. Dr. Wilhelm Stork (KIT, Karlsruhe)  
Korreferent: Prof. Dr. Jaume Pujol (UPC, Terrassa)





This document is licensed under the Creative Commons Attribution –  
Non Commercial – Share Alike 3.0 DE License  
(CC BY-NC-SA 3.0 DE): <http://creativecommons.org/licenses/by-nc-sa/3.0/de/>



# ¡Gracias!, Gràcies!, Thanks!, Danke!

Este trabajo es el punto final de un viaje lleno de pequeñas historias y grandes personas que han contribuido en múltiples formas a moldear este sueño hasta convertirlo en realidad.

La aventura comenzó hace ya algunos cuantos años. Me acuerdo bien que me ayudaste primero a elegir el rumbo y luego a no dejarme caer en el camino. Reímos, lloramos, paseamos y nos disfrutamos. Gracias Elizabeth por unirte al viaje, por acompañarme y por apoyarme cada vez que lo necesito. Sigamos caminando juntxs hacia nuevos sueños y destinos.

A ti sólo te he visto en fotos, pero ya eres parte central de un nuevo recorrido. Y de repente una pequeña ajonjolí viene para darle un nuevo sabor y color a nuestras vidas. Estamos ansiosxs por conocerte y tenerte en nuestros brazos. Gracias por adelantado por todas esas sonrisas que nos traerás y por con nosotrxs crecer y hacer camino.

No he sido el único que ha salido hacia nuevos destinos. Esa huella que me dejaron muy marcada desde pequeño me ha servido como base para definir lo que soy y lo que consigo. La distancia es el mal mayor de este viaje y las pequeñas charlas por teléfono no llenan para nada el hueco que tengo reservado para ustedes en mi corazón. ¡Que nunca se les olvide que lxs quiero! Gracias Angie y Enrique por estar allí y por siempre alentarme y servir de guía en mi travesía hacia mis objetivos.

También ustedes han crecido. La distancia y la diferencia horaria hace que a veces no lo escuchen: ¡lxs quiero y lxs extraño! Han sido cuatro años de risas perdidas y de muchos domingos sin hacer nada juntos. Cada paso de ustedes lo tomo como mío; aunque no lo parezca, caminamos juntos. Lili, Ele y Cáquela, gracias por quererme y por preocuparse por mí mientras he andado hasta llegar al final de este destino.

Con ustedes inició todo mucho antes del inicio de este viaje. Primero formaron a mis papás y luego su experiencia en la vida fueron muy buenas enseñanzas para mí. Tengo recuerdos muy bellos en los que ustedes son mis protagonistas principales. Algunas se han ido, pero desde Pijijiapan o desde un poco más arriba sé que siempre se preocupan por mí y que velan mis recorridos. Gracias abuelitas Ale, Marina y Angelita por siempre quererme a mí y a las que ahora caminan conmigo.

---

La verdad es que he estado muy bien acompañado en esta travesía. Ha habido muchas personas con las que he compartido muchas aventuras y desventuras. Nuestras charlas han servido para liberar el estrés y lo que hemos vivido me ha enseñado mucho sobre la importancia de la amistad y del compartir. Lxs quiero como si fueran parte de mi familia. Gracias Kath y Luis por todos esos momentos juntos y por todo este apoyo mutuo e incondicional en nuestros caminos. Gracias Anne-Chri, Juan Carlos, Gaby, Angel y Eva por todo lo que hemos compartido. Gracias Xana, José, Francisco y Carlos por apoyarme tanto en mi más reciente andar hacia éste y otros de mis nuevos destinos.

En esta aventura ha habido también horas de mucho trabajo y gente que me ha guiado con sus consejos para poder llegar al final del camino. Gracias Mikel por toda tu ayuda y por las aventuras que hemos compartido; fuera y dentro del CD6 has sido siempre un amigo. Gracias Jaume, primero por creer en mí para desarrollar este proyecto, luego por toda tu ayuda y supervisión a largo del proyecto y por último por tu apoyo a mis proyectos personales al final de este destino. Gracias Montserrat por todo lo que aprendí de ti sobre el mundo al que me metía al inicio de esta aventura.

Siempre que lo he necesitado, he recibido ayuda de muchas personas. Sin vosotrxs, mi andar hubiera sido mucho más lento y difícil. Gracias Anna, Ciscu y Ferrán por las charlas que me hacían entender mejor lo que buscaba. Gracias Fermín y Xavi por hacer mis ideas realidad en electrónica y mecánica. Gracias Rosa, Cristina, Maite por ayudarme a lidiar con temas administrativos.

This story was not only written in Spanish and Catalan, but also in German and English. During six months I had the opportunity to share knowledge and experiences with great people in Karlsruhe. Thanks to Marcia, Nico, Thorsten, Frank and Kai for the coffee breaks/chitchats that we shared during that time. Thanks to Wilhelm for his support as supervisor in this project. Thanks to Juranna for all her help with the paperwork that is allowing me to reach this dream.

Sometimes we need more than good intentions to fulfill our dreams. I would like to thank the Ministerio de Ciencia e Innovación (MICINN) and the European Union for their support to this project; and the Education, Audiovisual and Culture Executive Agency (EACEA) for the fellowship within the framework of the Erasmus Mundus Joint Doctorate EUROPHOTON-ICS.

A todos y todas: ¡Gracias! Este viaje no hubiera sido lo mismo sin ustedes.





# Abstract

Within the visual system, the optics of the eye is responsible for forming images of external objects on the ocular fundus for its photo-reception and neural interpretation. However, the eye is not perfect and its capabilities may be limited by aberrations and scattering. Therefore, the quantification of optical factors affecting the eye is important for diagnosis and monitoring purposes. In this context, this document summarizes the work done during the implementation of the Multimodal Eye's Optical Quality (MEOQ) system, a measurement device that integrates a double-pass (DP) instrument and a Hartmann-Shack (HS) sensor to provide not only information on aberrations, but also on scattering that occurs in the human eye. A binocular open-view design permits evaluation in natural viewing conditions. Furthermore, the system is able to compensate for both spherical and astigmatic refractive errors by using devices of configurable optical power. The MEOQ system has been used to quantify scattering in the human eye based on differences between DP and HS estimations. Moreover, DP information has been employed to measure intraocular scattering using a novel method of quantification. Finally, the configurable properties of the spherical refractive error corrector have been used to explore a method for reducing speckle in systems that rely on reflections of light in the ocular fundus.

**Keywords:** *optical quality, double-pass technique, Hartmann-Shack sensors, multimodal system, binocularity, refractive error compensation, scattering, speckle.*

# Kurzfassung

Innerhalb des visuellen Systems ist die Optik des Auges verantwortlich für die Abbildung externer Objekte auf dem Fundus des Auges, damit Licht umgewandelt und neural interpretiert wird. Dennoch ist das Auge nicht perfekt und seine Möglichkeiten sind durch Abbildungsfehler und Streuung begrenzt. Daraus ergibt sich, dass die Quantifizierung der optischen Faktoren, welche das Auge betreffen, wichtig für die Diagnose und Überwachung sind. Innerhalb dieses Rahmens fasst dieses Dokument die Arbeit zusammen, welche die Implementierung eines System zur multimodalen Bestimmung der optischen Qualität des Auges (MEOQ), bestehend aus einem Doppelpass-Instument (DP) und einem Hartmann-Shack-Sensor (HS), beschreibt, um nicht nur Informationen über Abbildungsfehler, sondern auch über Streuung im menschlichen Auge zu erhalten. Ein biokulares Freisicht-Design ermöglicht natürliche Sehverhältnisse. Darüberhinaus ist das System in der Lage sphärische und astigmatische Brechungsfehler mit einem Gerät einstellbarer optischer Leistung zu korrigieren. Das MEOQ System wurde genutzt um Streuung im menschlichen Auge mit Hilfe der Unterschiede der Abschätzungen des DP und des HS zu quantifizieren. Darüberhinaus wurden die DP Informationen angewandt um intraokulare Streuung durch eine neue Methode der Quantifizierung zu messen. Schließlich wurden die konfigurierbaren Einstellungen des sphärischen Brechungsfehlerkorrektor genutzt um eine Methode zur Reduzierung von Speckle in Systemen, welche auf Reflektionen von Licht vom Fundus des Auges basieren, zu untersuchen.

***Schlüsselworte:** Optische Qualität, Doppelpass Technik, Hartmann-Shack Sensoren, Multimodales Systemm, Brechungsfehler-Kompensation, Streuung, Speckle.*

# Resumen

Dentro del sistema visual, la óptica del ojo es responsable de la formación de imágenes de objetos externos en el fondo de ojo para su fotorrecepción e interpretación neuronal. Sin embargo, el ojo no es perfecto y sus capacidades pueden verse limitadas por la presencia de aberraciones o de luz dispersa. De esta manera, la cuantificación de los factores ópticos que afectan al ojo resulta importante para fines de diagnóstico y de monitoreo. En este contexto, el presente documento resume el trabajo realizado durante la implementación del sistema Multimodal Eye's Optical Quality (MEOQ), un dispositivo de medición que integra un instrumento de doble paso (DP) y un sensor de Hartmann-Shack (HS) para proporcionar no sólo información sobre aberraciones, sino también en la dispersión que se produce en el ojo humano. Un diseño binocular de campo abierto permite evaluaciones en condiciones visuales naturales. Además, el sistema es capaz de compensar tanto errores refractivos esféricos como astigmáticos mediante el uso de dispositivos de potencia óptica configurable. El sistema MEOQ se ha utilizado para cuantificar la dispersión en el ojo humano basándose en las diferencias entre estimaciones de DP y HS. Además, la información de DP se ha empleado para medir la dispersión intraocular utilizando un nuevo método de cuantificación. Por último, las propiedades configurables del corrector de refracción esférica se han utilizado para explorar un método para la reducción de ruido speckle en sistemas basados en reflexiones de luz en el fondo ocular.

**Palabras clave:** *calidad óptica, técnica de doble paso, sensores Hartmann-Shack, sistema multimodal, binocularidad, compensación de errores refractivos, dispersión, ruido speckle.*

# Resum

Dins del sistema visual, l'òptica de l'ull és la responsable de la formació d'imatges d'objectes externs en el fons d'ull per a la posterior fotorecepció i interpretació neuronal. No obstant, l'ull no és perfecte i les seves capacitats es poden veure limitades per la presència d'aberracions o de dispersió de la llum. D'aquesta manera, la quantificació dels factors òptics que afecten a l'ull és important per a finalitats de diagnòstic i monitoratge. En aquest context, aquest document resumeix el treball realitzat durant la implementació del sistema Multimodal Eye's Optical Quality (MEOQ). Aquest, és un dispositiu de mesura que integra un instrument de doble pas i un sensor de Hartmann-Shack per proporcionar no només informació sobre aberracions, sinó també sobre la dispersió que es produeix en l'ull humà. Un disseny binocular de camp obert permet avaluar l'ull en condicions visuals normals. A més, el sistema és capaç de compensar tant errors refractius esfèrics com astigmàtics utilitzant dispositius de potència òptica configurable. El sistema MEOQ s'ha utilitzat per quantificar la dispersió en l'ull humà basant-se en les diferències observades entre les dues tècniques. Cal afegir que la informació de doble pas ha permès mesurar la dispersió intraocular amb un nou mètode de quantificació. Finalment, les propietats configurables del corrector de refracció esfèric s'han utilitzat per explorar un mètode per a la reducció de speckle en sistemes basats en reflexions de llum al fons ocular.

***Paraules clau:** qualitat òptica, tècnica de doble pas, sensors de Hartmann-Shack, sistema multimodal, binocularitat, compensació d'errors refractius, dispersió, speckle.*

# Contents

<b>List of figures</b>	<b>xi</b>
<b>List of tables</b>	<b>xviii</b>
<b>List of abbreviations</b>	<b>xix</b>
<b>1 Introduction</b>	<b>1</b>
1.1 Objectives of the project . . . . .	6
1.2 Organization of this document . . . . .	9
<b>2 State of the art</b>	<b>11</b>
2.1 Objective determination of the optical quality . . . . .	12
2.1.1 Technique based on the analysis of retinal images . . . . .	12
2.1.2 Techniques based on the estimation of wavefront slopes . . . . .	15
2.1.3 Techniques based on phase diversity . . . . .	21
2.1.4 Technique based on measurements of longitudinal aberrations . . . . .	22
2.1.5 Eye assessment using binocular systems . . . . .	23
2.1.6 Eye assessment using multimodal systems . . . . .	25
2.2 Quantification of scattering in the human eye . . . . .	26
2.2.1 Methods based on the double-pass technique . . . . .	26
2.2.2 Methods based on the Hartmann-Shack technique . . . . .	28
2.2.3 Methods based on multiple techniques . . . . .	29
2.2.4 Other methods . . . . .	31
2.3 Speckle reduction . . . . .	33

<b>3</b>	<b>The MEOQ system</b>	<b>37</b>
3.1	Instrument design and implementation . . . . .	38
3.1.1	Light source and its effects on the retina . . . . .	40
3.1.2	Binocular open-view configuration . . . . .	44
3.1.3	Multimodality . . . . .	45
3.1.4	Spherical refractive error compensation . . . . .	48
3.1.5	Astigmatic refractive error compensation . . . . .	52
3.1.6	User interfaces and data processing . . . . .	54
3.2	Instrument validation . . . . .	58
3.2.1	Selection of HS reference data . . . . .	58
3.2.2	Compensation for residual errors . . . . .	60
3.2.3	DP and HS response comparison . . . . .	61
3.3	Conclusions . . . . .	64
<b>4</b>	<b>Estimation of the scattering properties of the ocular fundus</b>	<b>65</b>
4.1	Effects of retinal scattering on DP and HS measurements . . . . .	67
4.1.1	Experimental evidence of retinal scattering . . . . .	68
4.2	Incorporation of retinal scattering in the DP expression . . . . .	70
4.2.1	The double-pass expression . . . . .	72
4.2.2	Modeling scattering as equivalent diffuser . . . . .	73
4.2.3	Modeling scattering as lateral spreading of light . . . . .	78
4.2.4	Performance of the scattering models . . . . .	81
4.3	Estimation of the scattering properties of the fundus in real eyes . . . . .	82
4.3.1	Experimental procedure . . . . .	83
4.3.2	Data processing . . . . .	84
4.3.3	Results and discussion . . . . .	86
4.4	Conclusions . . . . .	95
<b>5</b>	<b>Aberration-free index to quantify scattering in the human eye</b>	<b>97</b>
5.1	Scattering and double-pass data processing . . . . .	99

5.2	The Aberration-Free Scatter Index (AFSI) . . . . .	102
5.3	The AFSI for different refractive conditions . . . . .	104
5.4	The AFSI for ocular fundus of different characteristics . . . . .	108
5.5	Application of the AFSI in human eyes . . . . .	111
5.6	Conclusions . . . . .	114
<b>6</b>	<b>Speckle reduction in double-pass images using focus-tunable lenses</b>	<b>117</b>
6.1	Speckle and its behavior . . . . .	119
6.2	Effects of vergence variations in double-pass response . . . . .	120
6.3	Materials and methods . . . . .	122
6.3.1	Experimental platform . . . . .	122
6.3.2	Experimental procedure . . . . .	124
6.3.3	Data processing . . . . .	125
6.4	Results and discussions . . . . .	127
6.4.1	Speckle reduction in an artificial eye . . . . .	127
6.4.2	Speckle reduction in real eyes . . . . .	130
6.5	Conclusions . . . . .	134
<b>7</b>	<b>General conclusions and future work</b>	<b>135</b>
7.1	Conclusions . . . . .	135
7.2	Future Work . . . . .	138
<b>A</b>	<b>Image formation in double-pass systems</b>	<b>141</b>
<b>B</b>	<b>Zernike polynomials</b>	<b>145</b>
	<b>References</b>	<b>147</b>



# List of Figures

1.1	Conceptual representation of the MEOQ system. . . . .	9
2.1	Representation of a double-pass instrument. Lenses: $L_1, L_2, L_3, L_4$ ; Pupils: $P_1, P_2$ ; Camera: $CM_{DP}$ . . . . .	13
2.2	Representation of the local shifts $\Delta$ at a reference plane produced by wavefront slopes $\theta$ . The set of displacements are used by wavefront sensors to estimate a map of aberrations affecting a given optical system. . . . .	16
2.3	Representation of a Hartmann-Shack instrument. Lenses: $L_1, L_2, L_3$ ; Pupil: $P_1$ ; Camera: $CM_{HS}$ ; Lenslet array: $L_{HS}$ . . . . .	17
2.4	Representation of a laser ray tracing instrument. Lenses: $L_1, L_2, L_3$ ; Pupil: $P$ ; Camera: $CM_{LRT}$ ; Lenslet array: $L_{HS}$ ; Beam splitter: $BS$ . . . . .	19
2.5	Representation of an objective Tscherning instrument. Lenses: $L_1, L_2, L_3, L_4$ ; Camera: $CM_T$ ; Beam splitter: $BS$ . The Tscherning screen is indicated in the figure. . . . .	19
2.6	Formation of Talbot images. A wavefront reaches a sinusoidal grating. The set of local slopes forming the wavefront forms a distorted Talbot image on the sensor of a camera located at a certain distance $\Delta_z$ from the grating. The arrows indicate the direction of the wavefront. . . . .	20
2.7	Image formation process in a pyramid sensor. The point-to-point intensity differences among the four beams formed on the camera contain information about wave aberrations. Lenses: $L_1, L_2$ ; Camera: $CM_P$ . . . . .	21
2.8	Illustration of a curvature sensor. Two images around the pupil plane are recorded ( $I_1$ and $I_2$ ). The differences between the images in term of intensities contain information on wave aberrations. . . . .	22
2.9	Representation of two double-pass PSFs with different amounts of scattering. The curve $I_{DP1}$ presents higher scattering than $I_{DP2}$ . The regions used to compute the OSI are also illustrated in the figure. . . . .	27

3.1	Scaled representation of the MEOQ system. Light source: <i>SLD</i> ; diaphragms: $P_1, P_2, P_3$ ; polarizers: $B_1, B_2$ ; beam splitters: $BS_1, BS_2$ ; lenses: $L_1, L_2, L_3, L_C$ ; mirrors: $M_1, M_2, M_3$ ; tunable devices: $C_{1-2}, L_T$ ; dichroic mirror: $DM$ ; hot mirror: $HM$ ; cameras: $CM_P, CM_{DP}, CM_{HS}$ . Only the elements for the left-eye optical path are labeled. . . . .	38
3.2	Diagram of the MEOQ system. The optical path of light from the <i>SLD</i> to the eyes (first pass) and the one from the eyes to the double-pass and Hartmann-Shack sensors (second pass) are indicated by colors. Labels of optical devices correspond to the nomenclature used in the text. . . . .	39
3.3	Experimental measurements of SLD power spectrum for different bias currents. The curves are labeled in [mA] and normalized to the maximum measured power. . . . .	41
3.4	Temperature prediction after 20s of exposition and likelihood of retina damage in function of time for the MEOQ system. . . . .	43
3.5	Schematic of the beam generation, translation, and separation processes in the MEOQ system. . . . .	44
3.6	2-levels module (a) and control of interpupillary distance ID (b) in the MEOQ system. . . . .	45
3.7	Double-pass response for a mirror placed at the pupil plane of the MEOQ system. The solid and the dashed line correspond to the measured MTF and the one expected for a pupil of 1.8mm in diameter. The images within the graphs are $8 \times 8$ arcmin cropped versions of the recorded images. . . . .	46
3.8	Hartmann-Shack response for different induced spherical (a) and astigmatic (b) aberrations. . . . .	47
3.9	Model of the spherical refractive error corrector. $L_T$ : tunable lens, $L_C$ : compensating lens, $f_C$ : focal length of lens $L_C$ . . . . .	48
3.10	Model (left) and spot diagram at the exit pupil plane for an entrance pupil of 4mm diameter (right) for three different focal lengths in the tunable lens of the spherical refractive corrector. . . . .	50
3.11	Characterization of the spherical refractive error compensator for the left and the right eyes. The measured (dots) and expected (dashed line) refractions are presented. The results of fitting the measured values are also showed in the plot (solid line). . . . .	51
3.12	Resistance of the tunable lens for different bias currents. The measured values (dots) are presented along with their curve fitting (solid line). . . . .	52
3.13	Characterization of the astigmatic refractive error compensator for the left and the right eyes. The measured (dots), fitted curve (solid line) and expected response (dashed line) are presented. . . . .	54

3.14	Graphical user interfaces in the MEOQ system . . . . .	55
3.15	Sequence followed during images recording. Data is recorded by intercalating frames of the cameras selected until capturing n-images for each of the imaging devices. . . . .	56
3.16	Flowchart indicating DP and HS data processing. . . . .	57
3.17	The MEOQ system. . . . .	58
3.18	Second pass response of the MEOQ system for the double-pass (DP) and Hartmann-Shack (HS) sensor. In the latter case, wavefront slopes are computed with respect to centroid positions of a reference image (left) and the intersections of an ideal grid used as theoretical reference (right). . . . .	60
3.19	Second pass response of the MEOQ system for both eyes. The double-pass (solid line), Hartmann-Shack (dashed line) and the diffraction limited response (dotted line) are plotted. $4 \times 4$ arcmin versions of the second-pass PSF for the DP and HS technique are also included. . . . .	61
3.20	Second pass response of the MEOQ system for the double-pass (solid line) and Hartmann-Shack (dashed line) sensor for different aberrations. The labels following the form (Sphere,Astigmatism) indicates the values of the induced aberrations. . . . .	62
3.21	Double-pass response of the MEOQ system for the DP (solid line) and HS (dashed line) sensors for an artificial eye. The double-pass diffraction limited curve is plotted in the figure (dotted line), although it is almost overlapped by HS data. The DP image and the one reconstructed from HS data are also presented. . . . .	63
4.1	(a): DP (solid line) and HS (dashed line) response for an artificial eye using retinas $R_1$ and $R_2$ . The HS data for both retinas appears in the figure, but they are overlapped. (b): Ratio of the double-pass to the Hartmann-Shack MTF for both pupils. . . . .	69
4.2	Horizontal cut of the 3D profile for retinas $R_1$ (a) and $R_2$ (b). . . . .	70
4.3	Comparison of three models for the diffuse component of the scattered field. $\bar{\Gamma}$ denotes data for the model proposed in this work, while $\bar{\Gamma}_B$ and $\bar{\Gamma}_M$ refer to curves using Beckmann's formulation and Marcos' model for retinal reflection, respectively. . . . .	77
4.4	PSF of the ocular fundus obtained for different wavelengths. (a): Model for lateral spreading proposed in this work for $r_0 = 5\mu\text{m}$ . (b): Model used by Hodgkinson (image taken from [1]). . . . .	80

4.5	(a): Estimations of MTFs affected by scattering using the models for equivalent diffuser with $r_0 = 10\mu\text{m}$ and $\sigma = 0.2\mu\text{m}$ ( $MTF_I$ , solid line), and lateral spreading of light with $r_0 = 2\mu\text{m}$ ( $MTF_{II}$ , dashed line). (b): Ratio between the curves computed with models I (solid line) and II (dashed line) and the diffraction limited response ( $MTF_{DL}$ , dotted-dashed line). . . . .	82
4.6	Flow diagram of the data processing that was followed to compute the HS (left) and DP (right) MTF for each series of 20 images. . . . .	85
4.7	$64 \times 64$ pixels cropped versions of the point spread functions obtained from DP (top) and HS (bottom) data for 4 of the 14 subjects that were measured using the MEOQ system. . . . .	87
4.8	Average DP (solid line, left) and HS (dashed line, right) for the 14 measurements on performed on real eyes using the MEOQ system. The individual estimations are also plotted in the figures (gray solid line). . . . .	88
4.9	Average DP (solid line) and HS (dashed line) response. The average of the differences $MTF_{Df} = MTF_{HS} - MTF_{DP}$ (a) and the ratios $MTF_{Rt} = MTF_{DP}/MTF_{HS}$ (b) between HS and DP data are plotted in the figure (black dashed-dotted line), as well as their individual estimations (gray solid line). . . . .	89
4.10	(a): Standard deviation of the height fluctuations $\sigma_I$ in function of the correlation length $r_I$ using the model for the equivalent diffuser. (b): Relationship between the correlation length $r_{II}$ for the lateral spreading of light and $r_I$ . The equations of the tendency lines fitting the data and the coefficients of determination are included in the figures. . . . .	90
4.11	(a): Comparison between $MTF_{Rt}$ and the curves $MTF_I$ (Model I, solid line) and $MTF_{II}$ (Model II, dashed line). (b): Comparison between $MTF_{DP}$ (dashed-dotted line) and the curves obtained by multiplying the Hartmann-Shack response with $MTF_I$ and $MTF_{II}$ . . . . .	91
4.12	Lateral spreading of light $r_{II}$ in function of the mean intensity at the edge of double-pass images $I_e$ (a) and ratio between the DP and HS Strehl ratios $SR_{Rt}$ (b). The equations of the tendency lines fitting the data and the coefficients of determination are included in the figures. . . . .	93
4.13	Lateral spreading of light $r_{II}$ in function of age. The equation of the tendency lines fitting the data and the coefficient of determination are included in the figure. . . . .	94
4.14	$64 \times 64$ pixels cropped versions of the point spread functions obtained from DP and HS data for the left and right eyes of subject MK. . . . .	95
4.15	Relationship between lateral spreading of light for the left ( $r_{ILL}$ ) and right ( $r_{IR}$ ) of the 3 subjects assessed binocularly. The tendency line fitting the data, its equation, and the coefficient of determination are included in the figure. . . . .	95

5.1	Illustrative representation of the radial profile of two double-pass images with different amounts of scattering. It is assumed that the profile $I_1$ contains stronger scattering than $I_0$ . . . . .	100
5.2	Cumulative intensity profile of the PSF. Measurements on a subject for different intraocular scattering (a; without scattering, red circles; with induced scattering, green squares) and for different wavelengths (b; 550nm, green circles; 650nm, red circles). The variations in function of the wavelength are attributed to different amount of scattering from the fundus. Images taken from [2] and [3]. . . . .	100
5.3	Conventional data processing performed over double-pass images until obtain the modulation transfer function (MTF) of the eye. . . . .	101
5.4	Illustration of the modulation transfer function before ( $MTF_r$ ) and after ( $MTF_e$ ) peak correction before normalization (a). The typical shape of the curve obtained as $MTF_r/MTF_e$ is shown in (b). $MTF_e$ represents the normalized version of $MTF_e$ . The shaded area indicates the data used during the computation of the AFSI. . . . .	103
5.5	Proposed method to compute the AFSI from DP images. . . . .	104
5.6	Raw (a) and corrected (b) MTF for diffusers $S_0$ (solid line), $S_1$ (dashed line), and $S_2$ (dotted-dashed line) and refractive errors $L_0$ (blue line), $L_1$ (green line), and $L_2$ (red line). The rectangles on the images indicate data in a zoomed area. . . . .	106
5.7	Bar plots indicating the average value of the raw (a, top) and corrected (a, bottom) MTF and the amount of scattering quantified through the OSI (b, top) and the AFSI (b, bottom). The data is presented for different amount of scattering and aberrations induced with diffusers $S_0$ (left bars), $S_1$ (middle bars), and $S_2$ (right bars) and lenses $L_0$ (blue bar), $L_1$ (green bar), and $L_2$ (red bar), respectively. . . . .	107
5.8	Raw (a) and corrected (b) MTF for diffusers $S_0$ (solid line), $S_1$ (dashed line), and $S_2$ (dotted-dashed line) and ocular fundus $R_1$ (blue line) and $R_2$ (green line). The rectangles on the images indicate a zoom over the illustrated area. . . . .	109
5.9	Bar plots indicating the average value of the raw (a, top) and corrected (a, bottom) MTF and the amount of scattering quantified through the OSI (b, top) and the AFSI (b, bottom). The data is presented for different amount of scattering induced with diffusers $S_0$ (left bars), $S_1$ (middle bars), and $S_2$ (right bars) and with ocular fundus $R_1$ (blue bar) and $R_2$ (red bar), respectively. . . . .	110
5.10	AFSI in function of the OSI for the 19 measured eyes. The tendency line fitting the data, its equation, and the coefficient of determination are included in the figure. . . . .	112

5.11	OSI (a) and AFSI (b) in function of the normalized RMS value of the Zernike coefficients $Z/\lambda$ for the 19 measured eyes. The tendency lines fitting the data, its equations, and the coefficients of determination are included in the plots. . . . .	113
6.1	Speckle contrast as function of defocusing $\varsigma$ for different illumination conditions $\beta$ and object roughness $\sigma_\phi$ . Image taken from [4]. . . . .	120
6.2	Zemax model used to simulate the effects of vergence variations in DP response.	121
6.3	Double-pass PSF (a) and MTF (b) for vergence variations of different amplitudes. The horizontal axis of the MTF is normalized to the cutoff frequency for a pupil diameter of 2mm. . . . .	122
6.4	Scheme of the double-pass system used during the experiments. Pupils: $P_1$ , $P_2$ ; beam splitter: $BS$ ; focus-tunable lens: $L_T$ ; lenses: $L_C$ , $L_1$ ; dichroic mirror: $DM$ ; mirror: $M_1$ ; cameras: $CM_{DP}$ , $CM_P$ . . . . .	123
6.5	Flow diagram of the process to determine $SC$ , $MTF$ , $\nu_c$ , and $SR$ from double-pass images. . . . .	125
6.6	First recorded ( $I_S$ , $I_R$ , and $I_0$ ; top) and average ( $\bar{I}_S$ , $\bar{I}_R$ , $\bar{I}_0$ ; bottom) double-pass images for the artificial eye. $c$ refers to the peak amplitude of the induced vergence variations during image recording. <i>On</i> and <i>Off</i> indicate states of the scanning mirror. . . . .	127
6.7	MTF of the benchmark image $\bar{I}_0$ (continued narrow line, left axis) and relative errors in the MTF for $I_0$ ( $e_{M0}(\nu)$ ) $I_S$ ( $e_{MS}(\nu)$ ), and $I_R$ ( $e_{MR}(\nu)$ ) (right axis). In the latter case, the curves are presented for three different amplitudes $c$ of the induced vergence variations. . . . .	129
6.8	First recorded ( $I_S$ , $I_R$ , and $I_0$ ; top) and average ( $\bar{I}_S$ , $\bar{I}_R$ , $\bar{I}_0$ ; bottom) double-pass images for CE (a) and MK (b). <i>On</i> and <i>Off</i> indicate states of the scanning mirror. . . . .	131
6.9	MTF of the benchmark image $\bar{I}_0$ (continued narrow line, left axis) and mean relative errors in the MTF for $I_0$ ( $e_{M0}(\nu)$ ) $I_S$ ( $e_{MS}(\nu)$ ), and $I_R$ ( $e_{MR}(\nu)$ ) (right axis) for subjects CE (a) and MK (b). . . . .	132
A.1	Image formation in the double-pass process. . . . .	141

# List of Tables

3.1	Variations in the second principal point $\Delta H_{2T}$ of the tunable lens, its image distance from the compensating lens $s'_C$ , and in the magnification of the corrector $M_C$ for different focal lengths $f_T$ of the tunable lens. . . . .	49
4.1	Mean intensity at the edge of double-pass images ( $I_e$ ), Strehl ratio ( $SR_{Re}$ ), correlation length ( $r_I$ ) and standard deviation of the height fluctuations ( $\sigma_I$ ) for Model I, and lateral spreading of light ( $r_{II}$ ) for Model II for the left eye of the 14 subjects. . . . .	90
5.1	Values of OSI and AFSI computed for the different combinations of diffusers ( $S_0$ , $S_1$ , and $S_2$ ) and lenses ( $L_0$ , $L_1$ , and $L_2$ ). The mean value and standard deviation of the OSI and AFSI per diffuser is also presented in the table. . . .	108
5.2	Values of OSI and AFSI computed for the different combinations of diffusers ( $S_0$ , $S_1$ , and $S_2$ ) and ocular fundus ( $R_0$ and $R_1$ ). The mean value and standard deviation of the OSI and AFSI per diffuser is also presented in the table. . . .	111
5.3	Normalized RMS value of Zernike coefficients $Z/\lambda$ , OSI, and AFSI for the left eye of the 19 subjects. . . . .	114
6.1	Strehl ratio (SC) for vergence variations of different amplitudes. . . . .	122
6.2	Absolute relative errors of the speckle contrast ( $e_C$ ), MTF ( $e_M$ ), cut-off frequency ( $e_\nu$ ), and Strehl ratio ( $e_S$ ) for the full speckle ( $I_S$ and $\bar{I}_S$ ), reduced speckle ( $I_R$ and $\bar{I}_R$ ), and reference images ( $I_0$ and $\bar{I}_0$ ). . . . .	130
6.3	Absolute relative errors of the speckle contrast ( $e_C$ ), MTF ( $e_M$ ), cut-off frequency ( $e_\nu$ ), and Strehl ratio ( $e_S$ ) for the full speckle ( $I_S$ and $\bar{I}_S$ ), reduced speckle ( $I_R$ and $\bar{I}_R$ ), and reference images ( $I_0$ and $\bar{I}_0$ ). . . . .	133
B.1	First 15 <sup>th</sup> terms of the Zernike polynomials. . . . .	146



# List of abbreviations

**AFSI** Aberration-free Scatter Index

**DP** Double-Pass

**FWHM** Full Width Half Maximum

**GUI** Graphical User Interface

**HS** Hartmann-Shack

**LSF** Line Spread Function

**MEOQ** Multimodal Eye's Optical Quality

**MTF** Modulation Transfer Function

**OSI** Objective Scattering Index

**OTF** Optical Transfer Function

**PSF** Point Spread Function

**PTF** Phase Transfer Function

**RMS** Root Mean Square

**SLD** Super Luminescent Diode

**SR** Strehl Ratio



# Chapter 1

## Introduction

The ability of the human visual system to process information from our surroundings gives it a key role in daily activities [5]. Thanks to vision we distinguish objects and obtain information on their shapes and locations. By this sense, we find friends in crowded places without changing our position and enjoy variety of landscapes offered by nature. Using this, we have configured complex systems and discovered stars and galaxies. Unfortunately, these capacities may be limited by imperfections in any of the structures involved in the visual process, including those that are present in the optics of the eye [6].

Within the visual system, the optics of the eye has the function of forming the image of external objects on the retina for its posterior photo-reception and neural interpretation. During the image formation process, the optical characteristics of the eye define the manner in which we receive information from those external stimuli. For instance, people with any uncorrected ametropia perceive distorted versions of the scenes that are being observed. According to the severity of the degradation and the conditions of the scene, the information may become unrecognizable. This situation may affect the development of daily activities that in normal or corrected conditions represent easy tasks, such as reading or driving [5]. From this point of view, the relevance of the optical part of the visual system relies on the fact that it represents a gateway for much of the external information that we receive from our surroundings.

The determination of the optical factors affecting vision is crucial to understand the manner in which images of external objects are formed on the retina [6, 7]. Moreover, the quantification of the different optical phenomena affecting the eye represents a necessary step before applying any correction procedure. For instance, the determination of the refractive state of the eye gives nowadays the opportunity to prescribe corrections through spectacles or con-

---

tact lenses with the proper spherical or astigmatic refractive optical power. In this sense, the quantification of not only refraction, but also other optical factors represents a way to increase our understanding on the processes occurring in the eye.

### **Factors degrading the optical quality of the eye**

Diffraction, aberrations, and scattering form the conjunct of optical factors leading the formation of external scenes on the retina [8, 9, 10]. Diffraction is an effect that arises from the wave propagation properties of light [11] and imposes a limit to the performance of any optical system<sup>1</sup> [12]. The eye is always affected by diffraction, which may become the dominant optical phenomenon in vision, especially when the response of the eye is measured for pupils of small diameters [13]. On the other hand, the refractive state of the eye allows the formation of image on the retina, but in some cases it may also induce deviations with respect to the behavior predicted by paraxial optics [12]. These aberrations limit the response of the eye to a greater or lesser extent depending on the severity of the deviations. In the case of scattering, inhomogeneities in structures of the eye with which light interacts provoke deviations in the trajectory of the light [11]. When an optical system is affected by scattering, the effect of this phenomenon is perceived as a veiling glare luminance surrounding bright objects [14].

As seen above, diffraction, aberrations, and scattering affect the response of the eye in different manners. One approach to measure the impact of these factors is through the determination of the optical quality of the eye [15]. The point spread function (PSF), modulation transfer function (MTF) [16], Strehl ratio, and root mean square (RMS) value of wave aberrations [12] are examples of parameters that can be used to provide estimations of the optical quality and to quantify the effects of diffraction, aberrations, and scattering in the image formation process taken place in the eye. For instance, the veiling glare observed in the PSF of the eye and the decrements in the MTF could be used to estimate the amount of scattering in the eye [10] and the presence of aberrations in the eye [17], respectively; the Strehl ratio or the RMS value of wave aberrations may be employed to quantify in a single number the overall effects of the different optical phenomena that is present in the eye [12, 18].

---

<sup>1</sup>Following the Huygen's principle of light propagation, a point in a wavefront can be considered as a source of spherical wavelets. When the wavefront is disturbed by any aperture, the interference between the individual spherical wavelets generates an intensity pattern consisting in a series of light and dark bands. This phenomenon is known as diffraction and its properties depend on the dimensions of the apertures limiting light and the working wavelength.

The determination of the optical quality is important in the sense that it provides information about the optical part of the visual system, which can be used to increase our understanding of different phenomena arising from the interaction between light and eye. Therefore, it is crucial to have (or develop) techniques and instruments capable of providing accurate information on all those factors affecting the eye.

### **The determination of the properties of the eye through history**

Vision has been a field of great interest through history. The impact of vision in our life and the possibility of correcting the effects of imperfections of the eye explain to a certain extent the interest in the field and the long way that has taken to obtain the knowledge that we have nowadays on the visual system. The development of objective methods to determine the optical quality of the eye has been an important consequence of this historical process, which is constantly updated partly by improvements in optical instrumentation able to provide every time a more detailed description of the eye.

More than 5000 years have passed since the earliest forms of assessing visual acuity by distinguishing double stars<sup>2</sup>. Although the factors producing presbyopia were not understood, problems to distinguish near objects with age were already described by Aristotle (384-322 B.C.) and Roger Bacon (1220-1292), being the later who realized the importance of having a theoretical basis to understand phenomena affecting vision as well as an explanation for correcting those problems. Going further than contemporary empiricism for making lenses to correct some refractive errors, Johannes Kepler (1571-1630) divided the optical from the physiological process in vision and made the first description of the optics of the eye in 1604. After the knowledge of the Snell laws in 1621, the principles behind refraction were understood and they were used by René Descartes (1596-1650) to provide a more precise analysis on the image formation process on the retina.

There were important advances in the development of visual tests and instruments that contributed to understand the optical performance of the eye. For instance, we find the demonstration of the limits of visual resolution using square wave grating and the construction of the first optometer to determine the focal length of the eye by Robert Hooke (1635-1703) and William Porterfield (1696-1771), respectively. George Bidell Airy (1801-1892) established the first basis for testing and correcting astigmatism and also provided the description of the best focused spot in 1835.

---

<sup>2</sup>The historical data in this section has been taken from [7].

---

Among other contributions, Hermann Helmholtz (1821-1894) invented the ophthalmometer and the ophthalmoscope to determine the dimensions of structures in the eye and to inspect visually the retina. This last instrument and the slit lamp introduced by Allvar Gullstrand (1862-1930) were the first instruments used to evaluate cataracts. Herman Snellen (1834-1908) provided a way to compute visual acuity from devising shapes of different sizes and orientation of particular configurations.

### **Objective determination of the optical quality**

The development of instruments and techniques to measure the eye continued throughout the 20th century. Within this time, different researchers focused their efforts on measuring the optical quality of the eye objectively. These conjunct of methods were based on the analysis of light coming from bright images projected onto the ocular fundus [15]. Using this principle, Flamant was able to measure the line spread function (LSF) of the eye in 1955 [19].

Throughout this period, technological advances were incorporated into the field of visual optics. This situation lead to the development of instruments and techniques nowadays available to determine the optical quality of the eye. One such example is the use of digital cameras [20] instead of photographic plates [19] to record aerial retinal images. This fact and the availability of increasing computing resources have permitted the analysis of the images by digital procedures. Alongside technological advances, the adaptation of procedures originally developed in other fields of research have contributed to the determination of the optical quality of the eye. For instance, Hartmann-Shack sensors were developed to measure turbulences of the atmosphere [21], but it is now a common instrument in visual optics used to determine the optical characteristics of the eye [22, 23].

Although subjective methods have historically been used to measure the impact of different factors in vision, objective methods permit evaluations of the physical processes behind the formation of images on the retina. Since it provides representative data on the optics of the eye, the objective determination of the optical quality represents a strong tool not only for the diagnosis and monitoring of optical imperfections affecting the eye [10, 24, 25], but also for the evaluation of treatment outcomes [26, 27]. Furthermore, the possibility of offering to patients proper diagnosis is increased if the information on the optical quality is accurate and detailed. Therefore, there is a necessity of systems able not only to provide overall estimations of the optical quality, but also to quantify the contributions of the different optical phenomena occurring in the eye.

Double-pass [20] and Hartmann-Shack [22] systems have arisen as excellent options to determine objectively the optical quality of the eye and are even used in clinical practice [23, 28]. The former technique provides overall estimations on the optical quality while the latter describes well the aberrations of the eye. However, the information they provide is limited by the own techniques under conventional data processing: the individual contribution of the different optical conditions affecting the retinal image cannot be determined from double-pass data, and the intraocular scattering is well represented in Hartmann-Shack information [29]. In this respect, we consider that systems based on multiple techniques (multimodal systems), are an alternative to take advantage of the strengths of both double-pass and Hartmann-Shack sensors and to perform a detailed optical characterization with information about various phenomena occurring in the eye.

### **Some figures around the optical quality**

Looking at the fact that there are more than 1400 million people with myopia in the world [30], it is not disproportionate the USD 26000 million at which Transparent Market Research [31] valued the Ophthalmology device market in 2012, which presents a situation highly fragmented with the presence of both well established and emerging companies. This figure includes diagnostic systems, surgery devices and vision care products and is estimated to reach USD 40000 million by 2019. The growth of this market is not only attributed to the increasing prevalence of visual disorders but also to the constant improvement in products. This indicates that Ophthalmology is an open market where new systems have a place if they are capable of providing detailed information on the optical quality of the eye.

Visual impairments<sup>3</sup> affect the quality of life of people by limiting to a greater or lesser extend different aspects of daily life [5], such as work, education, mobility, and recreation. For instance, a person with uncorrected refraction errors may not be able to distinguish letters in a book due to blurred vision. According to the World Health Organization [33], 43% of the cases correspond to people with uncorrected refractive errors and 33% to unoperated cataracts. It means that around two thirds of visual impairments can be avoided or cured if

---

<sup>3</sup>The International Classification of Diseases [32] considers that a person is visual impaired if he/she has a visual acuity lower than 3/10 and a visual field lower than  $10^\circ$  in radius around the central fixation. For characterizing visual impairments, visual acuity is measured with prescribed correction. However, the World Health Organization [33] recognizes as visual impaired also those people that fulfil these criteria and have no access to correction, such as spectacles and surgeries to correct myopia, hyperopia or astigmatism and eliminate cataracts, for instance.

they are previously detected and quantified.

In this context, the knowledge of the optical quality of the eye takes relevance because it provides to clinicians a strong tool for the diagnosis and monitoring of visual impairments and treatments. Thus, it results important to have available systems able to provide overall estimations of the optical quality and to quantify separately all those optical conditions affecting vision, i.e. aberrations and intraocular scattering.

## 1.1 Objectives of the project

There is a series of points that may summarize the information presented above. First of all, the importance of the visual system in our life should be mentioned ; the possibility of having more information from our surroundings through the formation of images on the ocular fundus and its posterior interpretation results crucial for most of our daily activities. Second, the optical performance of the visual system may be degraded by different factors affecting the eye. Third, the quantification of all those phenomena contributes to the understanding of processes occurring in the eye; moreover, this information may give clinicians strong diagnostic tools. Thus, the introduction of new systems to determine the contribution of factors affecting the eye or the improvement of current systems may result important for people suffering ocular diseases in the sense that they can benefit in the future to a greater or lesser extend from these ameliorations.

Within the scope of the Erasmus Mundus Joint Doctorate EuroPhotonics, this document summarizes the work forming the project *Multimodal Eye's Optical Quality (MEOQ)*, which has as main objective the *development of a new system permitting a complete evaluation in real time of the optical quality of the eye by the integration of multiple techniques*. This project was proposed by the Centre of Sensors, Instrument and System Development – CD6 (Universitat Politècnica de Catalunya – UPC, Spain) and the Institute for Information Processing Technologies – ITIV (Karlsruher Institut für Technologie – KIT, Germany), two experienced laboratories with great expertise in research and development projects in biomedical sensors, optical design, and optical instrumentation applied to the ophthalmologic field.

The objective marked for this project was reached after accomplishing the following tasks:

- **Development of a new instrument to evaluate the optical quality of the eye**

*Objective:* Design and development of a new system that integrates multiple techniques (multimodal system) able to perform a complete characterization of selected optical phenomena occurring in the eye. The system included the following features:

- Integration of a double-pass instrument and a Hartmann-Shack wavefront sensor.
- Binocular measurements in normal viewing conditions through an open field configuration.
- Correction of low order aberrations (spherical and astigmatic refractive error compensation).
- Use of single elements when possible.

*Milestones:* 1) Improvement of current experimental setups by adapting recent advances in the field. 2) Design and integration of a system based on both the double-pass and the Hartmann-Shack technique. 3) Validation of the new system with measurements of artificial eyes and a small group of subjects.

*Methodology:* From the previous background on double-pass systems and Hartmann-Shack wavefront aberrometers, we developed a new system combining both techniques (multimodal system). It was expected to define new parameters from information about both techniques to improve the description of the optical factors affecting the eye. In particular, this configuration allowed the quantification of scattering. The system is binocular and allows patients to fixate an external stimulus in open field. Moreover, several technological improvements were implemented, such as the inclusion of a subsystem for correcting astigmatism based on a set of cylindrical lenses of configurable orientation and the inclusion of a defocus error corrector based on lenses of tunable optical power. In this manner, the optical quality can be determined without the influence of defocus and astigmatism and the dynamic range may be used to determine the effects of higher order aberrations and scattering. The experimental setup was validated by means of artificial eyes and with a small group of subjects.

*Deliverables:* 1) Experimental setup for the complete characterization of the eye's optical quality. 2) Control software and user interfaces of the experimental setup.

- **Applications for the developed system**

*Objective:* Conducting a series of studies with the developed prototype to find possible applications and to determine its advantages over other state of the art devices and methods of quantification of different optical factors present in the eye.

*Milestones:* 1) Conducting experimental studies in young healthy subjects. 2) Quantification and identification of the sources of scattering in the eye. 3) Comparison with current methods for scattering quantification.

*Methodology:* Parameters with information on the optical quality of the eye were determined for a group of young subjects. The differences in response between double-pass and Hartmann-Shack technique are attributed mainly to the presence of ocular scattering. Since data corresponded to young healthy eyes, the amount of scattering was considered as arising in the ocular fundus. The inter-subject differences were determined and a method to characterize them was proposed. Moreover, the impact of intraocular scattering on the parameters with information on the optical quality was determined based on measurements using an artificial eye with the idea of identifying in the curves the origin of the scattering. Taking advantage of the configurable optical power in the spherical refractive error corrector, a new method was explored for speckle reduction in systems based on reflections of light on the ocular fundus.

*Deliverables:* 1) Experimental studies on healthy young subjects. 2) Quantification of the contribution of scattering in the measurements. 3) Proposal of methods for scattering quantification. 4) Exploration of a new method for speckle reduction.

The MEOQ system could be summarized in the conceptual chart presented in figure 1.1. In this, the implemented instrument is divided into three main parts: optical processing, data processing, and data analysis. The first part involves the binocular instrument itself and is formed by a double-pass (DP) and a Hartmann-Shack (HS) configuration able to perform simultaneous measurements of both eyes. The second part corresponds to conventional double-pass and Hartmann-Shack data processing. Therefore, the system provides independent estimations of parameters with information on the optical quality, such the PSF, MTF, and the Strehl ratio for both of the techniques. In addition, it is possible to offer estimations on wavefront aberrations and refraction based on data measured with the aberrometer. This information is complemented through a combined data analysis in a third stage within the system. At the end of this analysis, it is possible to provide estimates of scattering based on differences between techniques. The instrument implementation, calibration, and its applica-

tion for quantifying scattering and reducing speckle is presented in the following chapters of this document.

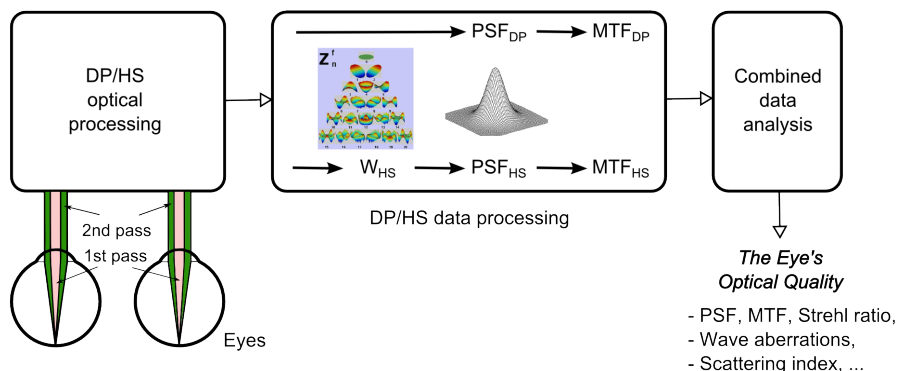


**Figure 1.1:** Conceptual representation of the MEOQ system.

## 1.2 Organization of this document

This dissertation is structured as follows. First of all, chapter 2 presents a review of current techniques available for the objective determination of the optical properties of the eye. This section covers not only double-pass instruments and Hartmann-Shack sensors, but also other techniques that have arisen for such purposes. The chapter includes a description of different methods that have been used in visual optics to quantify scattering. This review is done because one of the main applications of the MEOQ system is related with the quantification of this phenomenon. A small description of different methods that have been explored in this field of research for speckle reduction is presented.

Chapter 3 introduces the MEOQ system and the design of the instrument. Thus, the configuration that was implemented to obtain a binocular system working in open field configuration is explained. The details about both the astigmatic and spherical error correctors are also included. In addition, the software routines and interfaces developed for the MEOQ system are shown. The chapter covers also the validation of the instrument, which was based on having comparable double-pass and Hartmann-Shack estimations.

The scattering quantification based on the combined analysis of data from the multiple techniques is presented in chapter 4. The differences between the double-pass and Hartmann Shack MTF curves are used for this purpose. The deviations between responses are fitted to a model with parameters in function of the properties of the scattered light. The measurement conditions allow relating the differences to scattering arising in the ocular fundus. The details

of the models and the discussion of their applicability.

Chapter 5 introduces a novel index for the quantification of scattering based on double-pass measurements. The proposed index uses the information that is lost through the extrapolation of the zero frequency during the peak correction procedure usually performed over double-pass data. Unlike other methods for the quantification of scattering using double-pass data, the index presented here gives an estimation of intraocular scattering in the eye regardless of the presence of aberrations. The details for the computation of the index and the results based on measurements on an artificial eye are presented.

Chapter 6 explores a new method for speckle reduction in systems based on the light reflections in the ocular fundus, such as double-pass instruments and Hartmann-Shack wavefront sensors. The method takes advantage on the reconfigurability of the spherical refractive error corrector used in the MEOQ system to focus on the fundus a light beam with small fluctuations in optical power. The changes are produced during the recording of double-pass image to produce uncorrelated speckle patterns and reach in this manner a speckle reduction. The details of the method are explained.

Finally, chapter 7 presents the general conclusions of this work. The main results obtained are summarized in that chapter. The advantages and possible drawbacks of the system are discussed. In addition, the main points on the scattering quantification and speckle reduction are presented. The chapter ends with a series of proposals on future work. These include improvements and studies that could be performed using the MEOQ system.

## Chapter 2

# State of the art

The determination of the different phenomena that occur in the eye has long been an area of interest [7, 34]. Different techniques, some of them initially developed in other fields of research, and advances in technology have with time incorporated into a variety of instruments that allowing the objective assessment of the optical characteristics of the eye. For instance, the reconstruction of wave aberrations in the eye using Hartmann-Shack sensors [22] was possible after adapting a technology that had originally been designed to measure turbulences caused by the atmosphere [21]. Additional examples are the incorporation of laser sources and charge-coupled devices (CCD) into the instruments, which allowed to study the eye in monochromatic conditions and to analyze the measured data using digital processing.

This chapter presents a review of techniques that have arisen in visual optics for the objective assessment of the optical characteristics of the eye. In this manner, the intention is to give the context on which this project was developed. As stated in chapter 1, the goal of the project was to develop an instrument based on multiple techniques (multimodal system) for the objective evaluation of aberrations and scattering in the eye. The final system incorporates a double-pass instrument [20] and a Hartmann-Shack wavefront sensor [22]. In addition to the techniques used in the implemented system, we present here alternative methods that have been used in visual optics to estimate the optical quality of the eye.

Besides presenting the main characteristics of the assessment techniques, a review on methods for the quantification of ocular scattering is presented in this chapter. This review covers procedures that quantify this phenomenon by analyzing data either from single or from multiple assessment modes. In a similar manner, some methods that have arisen to reduce speckle noise in systems based on light reflections in the ocular fundus are introduced. All the topics

covered here are related to applications that will be introduced in the following chapters.

## 2.1 Objective determination of the optical quality

Different techniques have been developed over the years for objective determination of the optical properties of the eye. They range from analysis of aerial images in the double-pass technique [20] to the reconstruction of wave aberrations using a number of methods available for this aim [35]. These instruments have allowed the assessment of the optical quality of the eye in an objective manner not only under laboratory conditions but also in clinical environments using commercially available versions of the devices [23, 28, 36].

This section presents some of the techniques that have been available for the objective assessment of the eye. They are classified according to the feature used during the estimation of the optical quality. The techniques are explained and their main characteristics are introduced. The double-pass and the Hartmann-Shack techniques receive special attention because they were implemented in the MEOQ system. In addition, a review of binocular and multimodal systems is presented at the end of the section.

### 2.1.1 Technique based on the analysis of retinal images

#### Double-pass technique

The double-pass technique as it is known nowadays was introduced by Santamaría *et al.* in 1987 [20]. Instruments based on this assessment mode permit objective evaluations of the optical quality of the human eye by analyzing the aerial (double-pass) image of a point projected onto the retina. Before that work, optical properties of the eye had been evaluated with similar methods for unidimensional cases [15]. When presented, the novelty of the technique consisted in the fact that it allowed for the determination of the optical quality of the eye, but in a bidimensional manner while recording the images with digital devices.

A simplified version of a double-pass setup is illustrated in figure 2.1. In this setup, light from a point source is collimated before reaching the entrance pupil  $P_1$ . Then, light arrives at the eye after being directed by beam splitter  $BS$  and passing through the telescopic system formed by lenses  $L_2$  and  $L_3$ , which maintains the entrance and exit pupils  $P_1$  and  $P_2$  in planes that are conjugate to the pupil of the eye. In addition, the distance between lenses  $L_2$  and  $L_3$  may be varied to modify the vergence of the beam to correct spherical refractive errors of

the eye. After passing through the optics of the eye, the light is focused on the ocular fundus. Part of the incident light is reflected back towards the pupil, marking in this manner the beginning of the second pass in the double-pass process. Following an optical path identical to that of the first pass until beam splitter  $BS$ , light reaches the exit pupil  $P_2$  before being focused by lens  $L_4$  on the imaging device  $CM_{DP}$ , which records the double-pass images.

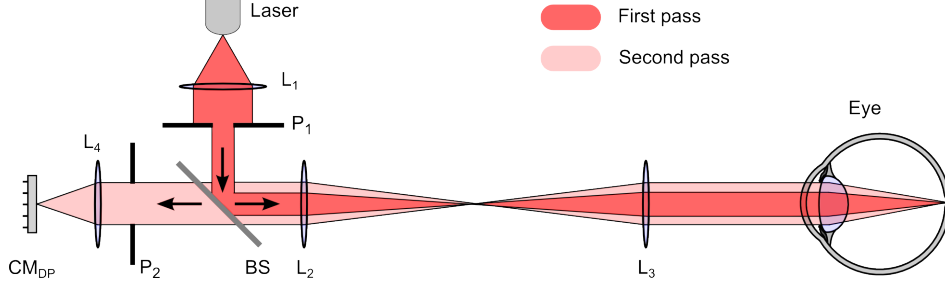


**Figure 2.1:** Representation of a double-pass instrument. Lenses:  $L_1, L_2, L_3, L_4$ ; Pupils:  $P_1, P_2$ ; Camera:  $CM_{DP}$ .

The images obtained with the double-pass technique contain information about optical factors affecting the eye, such as aberrations and ocular scattering [29]. The image formation process is presented in detail in appendix A. The incoherent intensity distribution obtained with double-pass systems ( $I_{DP}$ ) may be represented mathematically as the correlation of the intensity point-spread function of the eye for the first ( $PSF_1$ ) and second pass ( $PSF_2$ ) pupil diameters [13], which is expressed as

$$I_{DP} = PSF_2(mx'', my'') \otimes PSF_1(-mx'', -my'') \quad (2.1)$$

where  $m$  is the modulus of the first pass magnification,  $(x'', y'')$  corresponds to the coordinates at the second pass image plane, and  $\otimes$  denotes convolution. The Fourier transform can be used to obtain the response of the eye in the frequency domain [16]. When applied to double-pass images, we obtain a spectral representation that depends on the eye optical transfer function for the first ( $OTF_1$ ) and second pass ( $OTF_2$ ) pupil diameters [13], respectively. This situation is written as

$$\mathcal{F}\{I_{DP}\} = OTF_2(u, v)OTF_1^*(u, v) \quad (2.2)$$

where  $(u, v)$  are the coordinates in the frequency domain and  $*$  refers to the complex conjugate. The modulation transfer function (MTF) and the phase transfer function (PTF) are given by

the modulus and the phase of the OTF, respectively [16]. For systems with first and second pass pupils of identical diameters (symmetric systems), the MTF of the eye can be obtained as the square root of the Fourier transformed double-pass image [13],

$$MTF_e = \sqrt{\mathcal{F}\{I_{DP}\}} \quad (2.3)$$

The complex conjugate operation observed in equation 2.2 indicates that the phase in the Fourier transformed image is lost in symmetric double-pass systems. Therefore, it is not possible to recover information contained in this parameter using double-pass systems with this configuration [13]. For instance, a symmetric system does not allow recovering information on odd aberrations, such as coma. Since only the phase is lost, the MTF is not affected and it can be obtained by applying equation 2.3.

In order to keep the information related to the phase, a small first-pass pupil (diffraction limited) and a large second-pass pupil can be used to obtain double-pass images preserving the phase up to the limit imposed by diffraction [37]. In configurations with unequal pupils, the effects of placing a well-chosen small first-pass pupil can make the effects of aberrations negligible in the first-pass response of the eye. Since the theoretical effects of diffractions are known (an Airy disc with phase equal to zero) [16], it is possible to compute the OTF of the eye as

$$\begin{aligned} OTF_e &= \frac{OTF_2(u, v)OTF_1^*(u, v)}{OTF_d(u, v)} \\ &\approx OTF_2(u, v) \end{aligned} \quad (2.4)$$

where  $OTF_d$  corresponds to the diffraction limited optical transfer function for the first-pass pupil diameter.

There have been small changes since double-pass systems were introduced by Santamaría *et al.*. The majority of the modifications have been done to introduce technological improvements, but always following the same concept. For instance, the introduction of scanning mirrors [9] and rotating diffusers [38] allowed reducing the number of images and the integration time necessary to eliminate speckle in double-pass data [20]. Another example of these improvements is the substitution of Badal systems by spherical refractive error correctors based on lenses of configurable optical power [39].

The validity of the double-pass technique to determine parameters describing the optical quality of the eye has been widely studied under a variety of conditions. In this sense, the double-pass technique has been used to classify cataract patients [10, 40], to measure the optical quality before and after clinical procedures [26, 27, 41], to determine the effects of off-axis aberrations [42, 43], to detect dry eye [44], to perform studies on accommodation [45, 46], among others. Therefore, the double-pass technique represents a very useful tool that provides optical quality indicators that describe the properties of the eye under assessment. The double-pass technique is used in the OQAS (Visiometrics), a commercially available instrument used to assess the monocular optical quality of the eye in clinical environments [28].

Although double-pass images contain information on all the optical factors degrading the retinal image quality, the main drawback of this technique is maybe the impossibility of determining the individual contributions of such factors from the overall estimation. However, there is evidence that systems based on multiple techniques could be used for this purpose [29].

### 2.1.2 Techniques based on the estimation of wavefront slopes

Wavefront sensors are instruments that permit estimations of aberrations which in the case of the eye are produced either by the crystalline lens or by the corneal [47]. This type of sensors evaluates deviations in the wavefront with respect to the behavior predicted by paraxial optics [12, 48]. The majority of the wavefront sensors used in visual optics perform indirect measurements of local wavefront slopes to reconstruct a map of the aberrations affecting the eye [47]. In general, the slopes are estimated from displacements in the position at which light is focused on a reference plane. As observed in figure 2.2, the lateral shifts are proportional to the local slopes of the incident wavefront.

Once the wavefront slopes have been determined, Zernike polynomials [48, 49] can be used to reconstruct the wavefront of the eye [22]. A description of these polynomials is presented in appendix B. Using this orthogonal set of polynomials, the wavefront can be reconstructed by adding the weighted contribution of the different Zernike modes at a given position [50],

$$W(x, y) = \sum_j C_j Z_j(x, y) \quad (2.5)$$

where  $C_j$  is the coefficient of the Zernike mode  $Z_j$ . The spot displacements, the wavefront

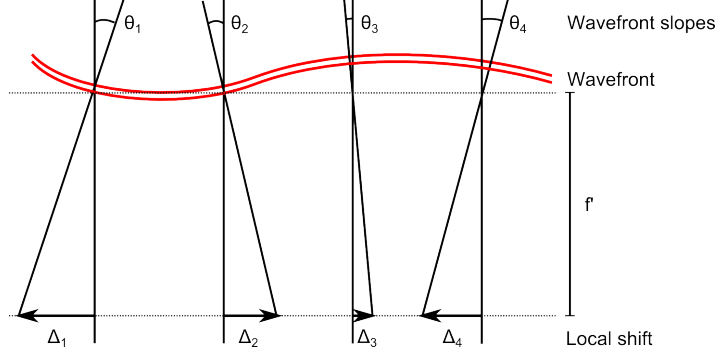


**Figure 2.2:** Representation of the local shifts  $\Delta$  at a reference plane produced by wavefront slopes  $\theta$ . The set of displacements are used by wavefront sensors to estimate a map of aberrations affecting a given optical system.

slopes, and the Zernike terms are related through the following expressions,

$$\frac{\Delta x(x, y)}{\partial x} = \frac{\partial W(x, y)}{\partial x} = \sum_j C_j \frac{\partial Z_j(\rho, \theta)}{\partial x} \quad (2.6)$$

$$\frac{\Delta y(x, y)}{\partial y} = \frac{\partial W(x, y)}{\partial y} = \sum_j C_j \frac{\partial Z_j(\rho, \theta)}{\partial y} \quad (2.7)$$

In matrix notation, equations 2.6 and 2.7 can be written as

$$\Delta = BC \quad (2.8)$$

where  $\Delta$  and  $C$  are column vectors representing the spot displacements in  $x$  and  $y$  and the unknown Zernike coefficients [49, 50], respectively. The  $B$  matrix accounts for the partial derivatives of the Zernike modes. With this representation, the set of coefficients can be obtained using a least-square estimation method:

$$C = (\Delta^T \Delta)^{-1} \Delta^T C \quad (2.9)$$

In the following paragraphs, we present a series of sensors based on the computation of local slopes to reconstruct the wavefront of the eye.

### Hartmann-Shack

Ophthalmic instruments based on Hartmann-Shack sensors are devices that use a lenslet array to sample the wave aberrations affecting the eye [22, 50]. Figure 2.3 depicts a Hartmann-Shack

configuration. In this schematic, the collimated light that reaches the eye is first focused on the ocular fundus. Up to this point, Hartmann-Shack and double-pass systems may present similar optical configurations. The light reflected by the fundus is used in Hartmann-Shack sensors as a point light source. The wavefront of the light emerging from this virtual source is distorted by wave aberrations during the second-pass of light through the optics of the eye [50, 47]. This aberrations are sampled at a plane conjugated to the pupil of the eye using the lenslet array  $L_{HS}$ . A camera  $CM_{HS}$  positioned at the focal plane of the array is used to record the spot array pattern, which contains the information that is needed to reconstruct the wave aberrations affecting the eye.

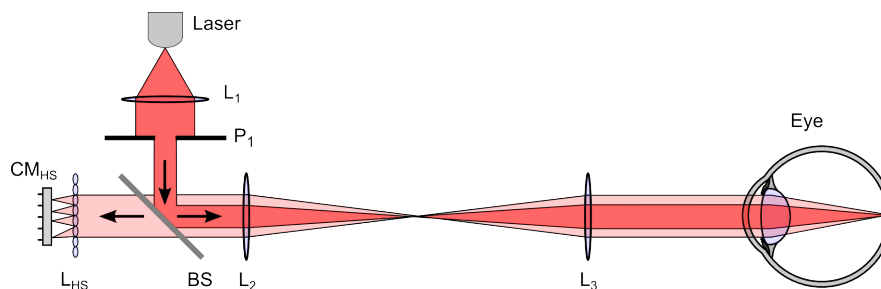


**Figure 2.3:** Representation of a Hartmann-Shack instrument. Lenses:  $L_1$ ,  $L_2$ ,  $L_3$ ; Pupil:  $P_1$ ; Camera:  $CM_{HS}$ ; Lenslet array:  $L_{HS}$ .

The lenslet consists of a series of microlenses with small aperture and short focal length that are regularly distributed over a common plane [47]. In aberration-free systems, a plane wave impinging on the lenslet array produces a series of spots at its focal plane at positions coinciding with the optical axis of each microlens. Any spot deviation from such theoretical positions is attributed to the presence of aberrations in the wavefront reaching the array [22, 47]. Once the deviations are determined, the magnitude of the displacements is used to map the wave aberrations of the eye under assessment using a set of Zernike polynomials [50].

Hartmann-Shack sensors have been used in a variety of applications that goes from the analysis of refractive conditions [9, 51] to the reconstruction of wave aberrations that are then employed in surgical procedures [52]. Moreover, they are the basis for instruments working with adaptive optics [53, 54, 55]. Hartmann-Shack sensors are probably the technology behind the majority of clinical systems used for estimating the optical quality of the eye [47].

There are different commercially available instruments working with Hartmann-Shack sensors. The aberrometers Zywave (Bausch & Lomb) and Wasca (Carl Zeiss Meditec) are examples of clinical systems based on this technique [23]. One of the main advantages of this kind of systems is that the information about aberrations is obtained simultaneously for the entire

pupil, which reduces the measurement time [56]. In the presence of scattering, the recorded spot array pattern may affect the local point spread function of the elements in the array resulting in veiling glare [57]. However, the centroids of the spot array pattern results unaffected, making it possible to determine the wave aberrations even if the recordings are affected by scattering [58].

The characteristics of the lenslet array impose a series of limitations to Hartmann-Shack sensors. For instance, an array with shorter separations between elements would permit sampling wave aberrations with finer resolution. Nevertheless, the dynamic range of Hartmann-Shack sensors is strongly affected by this parameter [47]. In addition, there is a relationship between number of lenslet elements used to sample the wavefront and the number of Zernike terms that can be used to reconstruct the wavefront. In this manner, higher order aberrations may be not sensed by this kind of sensors [18, 47]. Despite of these drawbacks, Hartmann-Shack instruments represent a strong tool in visual optics for determining the optical properties of the eye.

### **Laser ray tracing**

Laser ray tracing is a method that reconstructs wave aberrations by estimating spot displacements in a series of aerial retinal images of light pencils delivered sequentially at different positions along the pupil of the eye [59]. Referring to the laser ray tracing device illustrated in figure 2.4, a collimated beam of small diameter (light pencil) reaches the pupil at different positions in a sequential manner thanks to scanning mirror  $M_s$ . For each position a small focused spot on the retina is produced at a position that depends on both the scanned region at the pupil plane and the local wave aberration. The reflected light is then recorded at a conjugate plane with camera  $CM_{LRT}$ . At the end of the scanning process, a series of sequentially recorded images containing the spot positions of all the scanned regions is available. The local wavefront slopes are then computed by comparing the spot locations with respect to those obtained for an aberration-free system. In this manner, the joint spot deviations are used to reconstruct the wave aberrations with Zernike polynomials [56].

Since each point is recorded sequentially, the spots do not interfere among them in laser ray tracing devices. In this manner, laser ray tracing systems present a higher dynamic range with respect to Hartmann-Shack sensors [60]. The commercially available system iTrace VFA (Tracey Technologies) is an example of the use of laser ray tracing devices in the clinical practice [23].

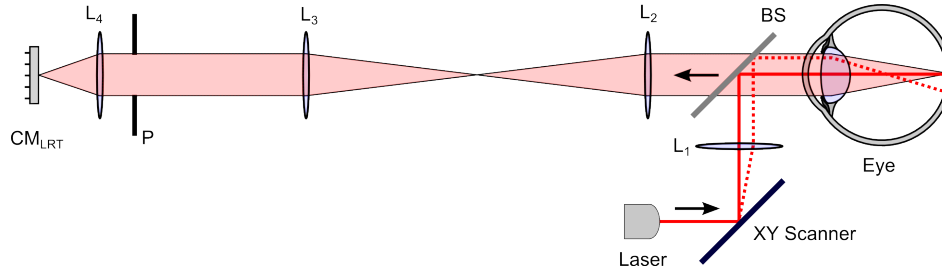


**Figure 2.4:** Representation of a laser ray tracing instrument. Lenses:  $L_1$ ,  $L_2$ ,  $L_3$ ; Pupil:  $P$ ; Camera:  $CM_{LRT}$ ; Lenslet array:  $L_{HS}$ ; Beam splitter:  $BS$ .

One of the disadvantages of the laser ray tracing systems is the longer time needed to complete the measurements over the entire pupil as a result of the sequential manner of obtaining the data [60]. Variations in the refractive conditions of the eye during measurements could provoke inaccuracies in the estimated wave aberrations. Moreover, changes in the structure of the ocular fundus could induce spot deviations that would be interpreted as aberrations [35].

### Objective Tscherning technique

The objective Tscherning is a technique that permits reconstructions of wave aberrations using the same measurement principle as the laser ray tracing, but from a set of light spots simultaneously projected on the pupil of the eye [23, 61, 62]. As illustrated in the setup depicted in figure 2.5, collimated light passes through a screen with a series of holes to generate a group of laser beams that reaches the eye at different positions along the pupil of the eye. The beams form a spot pattern on the retina resembling that observed in Hartmann-Shack images. The aerial image of the pattern is then used to estimate the wave aberrations affecting the eye from the distortions with respect to an aberration-free system using Zernike polynomials.

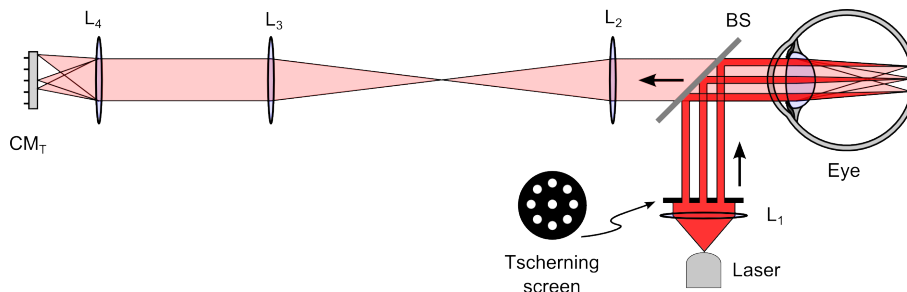


**Figure 2.5:** Representation of an objective Tscherning instrument. Lenses:  $L_1$ ,  $L_2$ ,  $L_3$ ,  $L_4$ ; Camera:  $CM_T$ ; Beam splitter:  $BS$ . The Tscherning screen is indicated in the figure

There are clinical commercial devices using this objective technique, such as the Allegretto

Wave Analyzer (Wavelight) [23]. Compared with laser ray tracing devices, the time that is necessary to record the spot positions is reduced because in the objective Tscherning technique the spot pattern is generated simultaneously for all the assessed areas. Therefore, variations in the refractive conditions of the eye have a lower impact during the computation of the wave aberrations. However, the dynamic range is reduced and the variations in the structure of the fundus may provoke undesired deviations in the spot pattern [23, 35].

### Talbot sensors

Talbot sensors use the changes in the self-image [16] of a two-dimensional grating to reconstruct the wavefront of the eye [63, 64]. When a sinusoidal grating is illuminated by a plane wave, the effects of diffraction form an intensity pattern at certain distances behind the element that can be interpreted as a perfect image of the pattern [16]. These images are known as Talbot, or self-images, and are formed without the presence of lenses. Under the influence of aberrations, Talbot images are distorted due to the local slopes of the wavefront [64]. Using a two-dimensional grating, the Talbot image consists in a series of spots whose positions depend on the wave aberration of the eye. In this sense, Talbot sensors can be seen as a simple version of a Hartmann-Shack sensor [35]. When measuring the eye, the grating is placed at the pupil plane and the image is recorded with a camera whose sensor is separated from the grating a certain distance that permits the formation of Talbot images [64], as observed in figure 2.6.

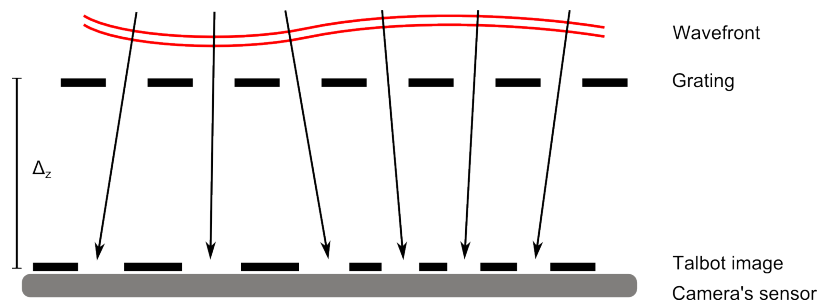


**Figure 2.6:** Formation of Talbot images. A wavefront reaches a sinusoidal grating. The set of local slopes forming the wavefront forms a distorted Talbot image on the sensor of a camera located at a certain distance  $\Delta_z$  from the grating. The arrows indicate the direction of the wavefront.

Due to the similarity between the Talbot and Hartmann-Shack sensors, they may show similar performances, including the limitations in dynamic range. The shifts produced in the spots by aberrations can be analyzed to that of Hartmann-Shack sensors or by determining the phase shift introduced by the wavefront slope in the frequency domain [64]. Then, this information

may be used in combination with Zernike polynomials to reconstruct the wavefront of the eye. The use of analysis in the Fourier domain may result in a reconstruction with higher resolutions [64] with respect to Hartmann-Shack sensors. Nevertheless, this type of data processing requires higher computational resources.

### 2.1.3 Techniques based on phase diversity

#### Pyramid sensor

Pyramid sensors are devices able to provide information on the first derivative of wave aberrations of the eye based on differences in intensities in images formed by mean of a pyramidal refractive element [65, 66, 67]. As illustrated in figure 2.7, a four faceted glass pyramid is placed in the Fourier plane of a lens positioned at a plane conjugated to the pupil of the eye. After being refracted by the pyramid element, the resultant four beams (one per face of the refractive element) are recorded by a camera located at a plane conjugated to the pupil of the eye by lens  $L_2$ . In an aberration-free system, the camera would record four beams with identical intensities. Under the presence of aberrations, the intensities are modified and the point-to-point differences provide information on the local slope of the wave aberration affecting the eye. On its extended source version [65], an incoherent light source is used to project probe beams of configurable size on the retina. This configuration enables the formation of energy-balanced equally aberrated fields on the four faces of the pyramid, which allows carrying on the point-to-point analysis of intensities.

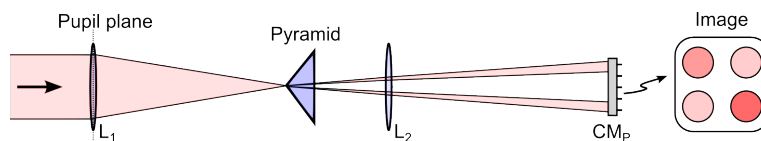


**Figure 2.7:** Image formation process in a pyramid sensor. The point-to-point intensity differences among the four beams formed on the camera contain information about wave aberrations. Lenses:  $L_1$ ,  $L_2$ ; Camera:  $CM_P$

One of the advantages of this kind of sensors is its configurable resolution and dynamic range. While the former of these two parameters may be improved by increasing the magnification of the image formed on the sensor of the recording device, the dynamic range can be easily modified by changing the size of the probe beam impinging on the retina. On the other hand, measurements may be affected by corneal reflections [65]. Based on the analysis of intensities, changes in reflectivity caused by variations in the structure of the ocular fundus

may be quantified erroneously as aberrations. Therefore, this kind of sensors may no be a robust option for clinical environments.

### Curvature sensor

Curvature sensors rely on the comparison of intensities at two close planes around the pupil plane to estimate wave aberrations. Referring to the system proposed in [68], a modified version of a double-pass setup may be used to record the images. In this schematic, the light returning from the ocular fundus is used to generate two parallel beams with an optical path difference between them. This configuration allows using of a single camera to record simultaneously an in-plane and an out-of-plane version of the intensity at a plane conjugate to the pupil. Then, phase retrieval algorithms are used to estimate the wave aberrations after analyzing the point-to-point differences in intensities.

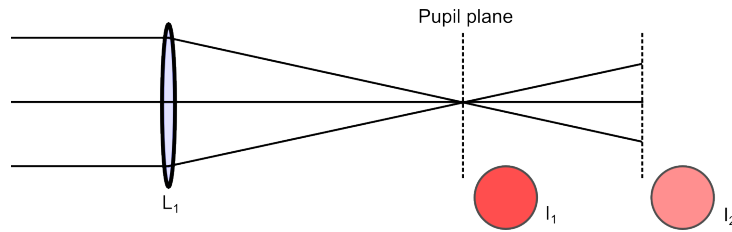


**Figure 2.8:** Illustration of a curvature sensor. Two images around the pupil plane are recorded ( $I_1$  and  $I_2$ ). The differences between the images in term of intensities contain information on wave aberrations.

Compared with Hartmann-Shack instruments, systems based on curvature sensors provide a higher resolution. The dynamic range depends on the system configuration. Hence, this parameter should be considered during the instrument design. The main drawbacks of the sensor are possibly the higher time and computational cost resulting from the use of phase retrieval algorithms [35, 68]. As in pyramid sensors, fluctuations in the structure of the ocular fundus may produce changes in the measured intensity, which would induce inaccuracies during the estimation of the wave aberration.

#### 2.1.4 Technique based on measurements of longitudinal aberrations

##### Objective retinoscopy

In this technique, an infrared fast moving slit is projected sequentially along a given meridian of the pupil of the eye. The light reflected by the fundus is then captured by an array of photo-detectors in a conjugate plane. The reflected light moves along the meridian with a

specific speed and direction that depends upon the longitudinal aberrations of the eye. This information is registered by the array of photo-detectors and then processed to reconstruct a map of the wave aberrations affecting the eye. This process is repeated along several meridians until a 360 degree area is covered [23, 35, 69]. Contrary to sensors based on the computation of wavefront slopes (transversal aberrations), this technique is sensitive to radial deflections (longitudinal aberrations) [69].

Although the technique is used in a commercial device (OPD Scan III), it may not provide repeatable measurements in clinical environments [23, 70]. Recently, some authors have presented algorithms to improve the accuracy of this kind of sensor [69, 71].

### 2.1.5 Eye assessment using binocular systems

The objective determination of the optical quality has been studied mainly for monocular conditions using instruments based on the techniques described above. However, the visual system is itself binocular and the performance of vision may present differences between monocular and binocular conditions. For instance, some authors have suggested that micro-fluctuations in accommodation could be smaller under binocularity [72]. The optical behavior of both eyes may be studied sequentially using monocular instruments [17, 73, 74]. However, the optical system of the human eye has a time-variant behavior [9] and changes in the optical conditions between the sequential measurements of the eyes may provoke inaccuracies during data comparison. In this sense, binocular instruments are the natural option to study the optics of the eye under binocular conditions.

In the following paragraphs different binocular instruments that have been introduced to determine the optical characteristics of the eye are presented. The systems are classified according to the manner in which the fixation test is presented to the subject: open or closed field. The main advantage of the former configuration with respect to the latter one relies on the fact that measurements are performed in normal viewing conditions because accommodation is reached by the eye without being influenced by the optics of the measurement system.

#### Systems working in open field

The interest in determining the optical characteristics involved in vision using open field configurations is not new. In 1989, Heron *et al.* [75] and some years later Okuyama *et al.*

[76] presented different versions of optometers that permitted studies on accommodation in normal viewing conditions. These systems worked in infrared light. Besides accommodation, the system presented in [76] allowed studies on pupil diameters and eye movements. Although these systems were able to determine the refractive state of the eyes, other parameters with relevant information of the optical quality such as the point spread function were not available. In addition, these instruments were based on element duplication, which increases both the size and cost of the final system.

Binocular systems have benefited by the incorporation of Hartmann-Shack sensors. Hampson, Chin, and Mallen [38, 77] presented a binocular system that allowed studying the behavior of ocular aberrations in real time (microfluctuation of accommodation at 20.5Hz) using a fixed target. The systems introduced by Kobayashi *et al.* [78] and more recently by Chirre *et al.* [79] are examples of other Hartmann-Shack systems that have been designed in an open field configuration. These systems were conceived to study accommodation, convergence, pupil size, and aberrations in normal viewing conditions. Unlike the configuration used in [78], which is based on element duplication, the systems in [38, 79] were implemented using single laser sources and recording devices to measure both eyes. The simultaneity of the measurements is assured under this configuration and permits accurate comparison of data from both eyes.

### Systems working in closed field

Talbot sensors have been used in binocular systems. Warden *et al.* [80] introduced a system based on the self-image effect that permitted an evaluation of both eyes. The system corresponded to the instrument Z-View that was commercialized by Ophthoniex. The company was closed in 2012 and the details of its configuration are not available.

Fernandez *et al.* [54] presented a Hartmann-Shack system to analyze the performance of the eye under a variety of conditions. The instrument was able to configure a complex pupil function with different shapes and sizes using a spatial light modulator [81]. Among other studies, the analyzer has been used to determine stereopsis in the presence of aberrations [82]. The optical paths for the left and the right eyes share the majority of the elements in the system.

Sabesan *et al.* [83] introduced also an instrument based in Hartmann-Shack sensors. In this case, binocularity was reached by element duplication, except for the laser source. A deformable mirror permits corrections of higher order aberrations in real time. The application

of the system is related to studies on the performance of the visual systems and binocular summation when higher order aberrations are corrected during measurements.

### 2.1.6 Eye assessment using multimodal systems

Systems based on multiple techniques (multimodal systems) have been used in visual optics for different purposes. The advantage of this kind of systems relies on the fact that data from multiple techniques can be compared and used to provide complementary information on the optical processes occurring in the eye. Moreover, multimodal systems have allowed the validation of measurements and quantification methods of a given phenomenon using the techniques implemented in the system. Limiting the research to systems based on double-pass instruments or Hartmann-Shack sensors, this section presents some multimodal systems that have been realized by different groups to measure the optical properties of the eye.

One of the first systems that combined double-pass and Hartmann-Shack instruments was implemented by Prieto *et al.* [50]. The work was presented some years after the adaptation of Hartmann-Shack sensors to visual optics [22] and its main objective was to study the sources leading to differences between techniques. After analyzing different parameters, the deviations between double-pass and Hartmann-Shack data were attributed at that moment to the effects of the integration time during image recording. However, different authors have suggested that the main source of the differences is related to ocular scattering [29, 84].

Multimodal systems have also been used to study the scattering occurring within the eye. Cox *et al.* [58] used a system based on multiple techniques to study the effect of intraocular scattering in double-pass instruments and Hartmann-Shack sensors. Although the techniques shared most of the optical path, the selection of the technique used during measurements depended on the presence of a removable mirror, therefore the system was not able to provide simultaneous estimations. The authors found that data from wavefront sensors were not affected by induced intraocular scattering whereas double-pass measurements contained information on this phenomenon. This behavior was considered by Shahidi and Yang [85], and Rodriguez and Navarro [86] to provide estimations of ocular scattering. In the former case, the authors used the line spread function obtained with a modified version of a double-pass configuration and a Hartmann-Shack sensor to obtain information on scattering. In the case of Rodriguez and Navarro, this information was derived from differences in the modulation transfer function computed from double-pass and laser ray tracing data.

Bueno *et al.* [87] introduced a system that permitted the assessment of double-pass and Hartmann-Shack information using different polarization states between the light reaching the eye and that reflected from the fundus. The system was used to compute double-pass data for different combinations between the first and second pass polarization states. The differences between measurements were then considered to provide an index of scattering. Despite the presence of the Hartmann-Shack sensor in the system, wavefront data was used to corroborate the refractive state of the artificial eye that the authors employed during the experimentation, but not to provide complementary information.

Besides quantifying scattering, multimodal systems have been used for other purposes. Aldaba *et al.* [45] and Vinas *et al.* [88] implemented systems based on double-pass instruments and Hartmann-Shack sensors to validate the use of the double-pass techniques in studies of accommodation and to study the influence of longitudinal chromatic aberrations in the eye, respectively. To do this, the work presented in [45] compared data between techniques for different accommodative states. In the case of [88], an adaptive optics system was used to obtain data from both techniques at different wavelengths under natural and corrected aberrations.

## 2.2 Quantification of scattering in the human eye

The use of multimodal systems may be useful to quantify phenomena complementary between techniques. For instance, the fact that scattering affects double-pass instruments but not Hartmann-Shack sensors [29, 58] suggests that the combined analysis of data from these two techniques may be used to quantify scattering. Since the system that will be introduced later in this work combines these techniques, this would be a natural application for it. For this reason, we present here a review of some objective methods that have been used for similar purposes, including not only those based on double-pass and Hartmann-Shack systems, but also other options based on different techniques.

### 2.2.1 Methods based on the double-pass technique

#### OSI

The ocular scatterer index, OSI, is an objective manner of quantifying scattering based on the analysis of double-pass images [10]. The index is defined as the ratio between the integrated

intensity at an eccentric region of the image ( $I_R$ ) and that surrounding its central part ( $I_0$ ). This relationship between intensities is given by the following expression,

$$OSI = a \frac{I_R}{I_0} \quad (2.10)$$

where  $a$  is a scale factor that is used to provide an index between a given range of values. The authors in [10] used a factor of  $a = 0.1$  to limit the values of OSI from 0 to 25 and the intensities contained in a ring between 4 and 12 arcmin of the double-pass image to compute  $I_R$ . In the case of the central region, all those intensities contained in a circle of radius 1 arcmin were considered to obtain  $I_0$ . These regions are illustrated in figure 2.9 for two curves emulating different amounts of scattering.

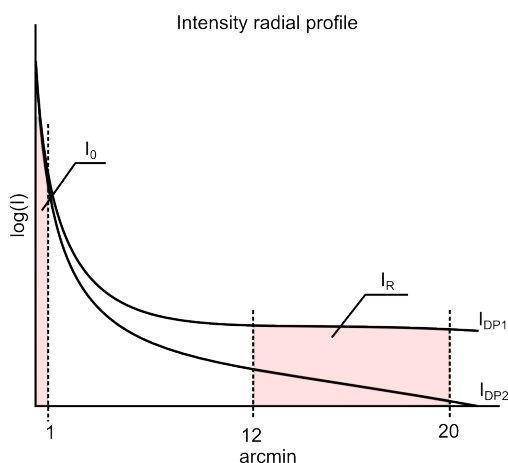


**Figure 2.9:** Representation of two double-pass PSFs with different amounts of scattering. The curve  $I_{DP1}$  presents higher scattering than  $I_{DP2}$ . The regions used to compute the OSI are also illustrated in the figure.

As observed in figure 2.9, the OSI uses the increment in intensities produced at the base of the double-pass PSF of the eye. The limits of the eccentric regions were defined by the authors to minimize the effects of aberrations during the computation of the index. However, eyes with aberrations beyond a certain limit may influence the results. One of the main applications of the OSI is the classification of cataract patients. In this sense, changes in the veiling glare from scattered light are considered to have their origin in the lens of the eye. Yet, at certain wavelengths scattering arising from the ocular fundus may produce a shift in the index. Nevertheless, the OSI represents nowadays a robust method to quantify scattering by objective means.

### Degree of polarization

Some authors have used the degree of polarization as an indicator of the amount of scattering in the human eye [87]. This method is based on the depolarization process occurring during the interaction of light with surfaces producing scattering. The method uses intensities in double-pass images under different controlled polarization conditions between the first and second pass of light through the system. The measured intensity is proportional to the polarization state, which in turn depends upon the amount of scattering contained in the optical system under assessment. The changes in intensity are then used to obtain a Stokes vector with coefficients depending on the amount of scattering in the double-pass images.

In the method proposed in [87], the polarization states were determined at four different orientations. The four Stokes terms resulting from this measurements are used to compute the degree of polarization as the ratio of the polarized-component terms ( $S_1, S_2, S_3$ ) to the term standing for the integrated intensity ( $S_0$ ),

$$DOP = \frac{(S_1^2 + S_2^2 + S_3^2)^{1/2}}{S_0} \quad (2.11)$$

One disadvantage of the method is the necessity of obtaining four images under different polarization conditions, which may increase the measurement time. During the integration, the authors used a rotating a  $\lambda/4$  plate to generate the polarization combinations. As a result, the precision of the orientation may influence the accuracy of the quantification.

#### 2.2.2 Methods based on the Hartmann-Shack technique

##### Analysis of the spot array pattern

Although the estimation of wave aberrations with Hartmann-Shack sensors is not affected by scattering [58], the spot array pattern has been used to provide scatter estimations [57]. In this method, each lenslet of the Hartmann-Shack array is considered as a small imaging system affected by the local properties of the lens at the sampled position. Therefore, if the eye is locally affected by scattering, the corresponding spot may present a veiling glare arising from this phenomenon. The individual analysis of the spots in the array pattern may be used to provide spatially resolved estimations of scattering.

In the methodology proposed in [57], the radial variance for spot blur is used as an estimator of scattering. Following the derivation of the method proposed by the authors, the radial variance containing the effects of the PSF for the eye and lenslet  $V(h)$  results of adding the radial variance due to the presence of aberrations  $V(h_0)$  to that produced by scattering  $V(h_s)$ ,

$$V(h) = V(h_0) + V(h_s) \quad (2.12)$$

Therefore, the methodology consists of determining the effects of scattering along the entire pupil. Contrary to the OSI, the computation of the radial vergences gives spatial information on scattering, but not on its overall effects on the point spread function of the eye. On the other hand, the quantification of scattering for all the lenslet positions requires more time and demands higher computational resources.

### 2.2.3 Methods based on multiple techniques

#### Differences between DP and HS measurement

Measurements from double-pass and Hartmann-Shack systems have been used to estimate the amount of scattering in the eye. For instance, the line spread function obtained with a modified version of a double-pass setup and a wavefront sensor have been used to estimate ocular scattering [85]. The authors defined an index based on the difference between the areas under the curves measured with both of the techniques,

$$LSI = \text{area}(LSF_{DP}) - \text{area}(LSF_{HS}) \quad (2.13)$$

Since double-pass data contain the overall effects of optical factors affecting the eye, it was considered that the curve  $LSF_{DP}$  enclosed the effects of aberrations and scattering whereas the curve  $LSF_{HS}$  was assumed to be affected by aberrations only. In this manner, the difference between areas may be related to the amount of scattering in the eye.

It should be mentioned that the computation of the LSI may be affected by residual light reflections in the double-pass image. This spurious light could come from light reflected at the surface of the eye lenses or in optical devices within measuring system. In this situation, the index may suffer a shift during the quantification of scattering. Moreover, higher order

aberrations undetected by Hartmann-Shack sensors may be another source of deviations of the index.

Differences in the modulation transfer functions between techniques have also been used to quantify scattering. Díaz-Doutón *et al.* [29] used two independent instruments to estimate the MTF with a double-pass instrument and a Hartmann-Shack sensor. The results obtained were used to provide an index of scattering based on the values of Strehl ratios computed for both measurement techniques. With a Strehl (SR) ratio defined as the area under the MTF, the information on scattering was obtained in the following manner:

$$SR_{HS-DP} = \frac{SR_{HS} - SR_{DP}}{SR_{HS}} \quad (2.14)$$

where the sub-indexes *DP* and *HS* correspond to data for the double-pass and the Hartmann-Shack technique, respectively. The authors were able to find differences between the techniques that were attributed to intraocular scattering. However, part of the deviations may be provoked by differences between double-pass and Hartmann-Shack data related to scattering arising in the ocular fundus [84] at certain wavelengths. The authors applied a peak correction [89] to double-pass data before the computation of the index. Therefore, that information on scattering contained at zero frequency is not considered during the quantification.

### Computation of an equivalent diffuser

The effects of scattering have been used to quantify parameters of an equivalent diffuser that would produce the same effects as those observed during measurements. This method was used in [86] using data from a double-pass instrument and a laser ray tracing wavefront sensor. The modulation transfer function was the parameter used for this purpose. As in Hartmann-Shack sensors, it is supposed that estimations from laser ray tracing devices remain unaffected by scattering. In this manner, the differences between the MTF from double-pass and laser ray tracing estimations are assumed to be mainly related to scattering. The authors developed a model based on the Beckmann-Kirchhoff scattering theory [90] to provide an expression for the double-pass curve ( $MTF_{DP}$ ) in function of that obtained from the wavefront sensor ( $MTF_{LRT}$ ) and the parameters defining statistically the equivalent diffuser. In mathematical terms, the relationship is given by the following expression

$$\begin{aligned}
 MTF_{DP}(u, v) &= MTF_{LRT}(u, v) \exp(-k^2\sigma^2) \times \\
 &\times \left\{ 1 + k^2\sigma^2 \exp \left[ -\frac{\lambda f'}{r_0} (u^2 + v^2)^{1/2} \right] \right\}
 \end{aligned} \tag{2.15}$$

where  $k = 2\pi/\lambda$  is the wavenumber,  $f'$  represents the focal length, and  $(u, v)$  are the frequency coordinates. In the case of  $\sigma$  and  $r_0$ , they represent the standard deviation of the height fluctuations (roughness) and the correlation length (space between scattering element in the surface) defining the equivalent diffuser, respectively. Once the curves from both of the techniques were computed, a fitting procedure was carried out to obtain the values of  $\sigma$  and  $r_0$  defining the equivalent scattering surface for the measured eye.

The model developed in [86] was thought for intraocular scattering. Therefore, the parameters obtained with this procedure accounts for an equivalent diffuser that would be present at the pupil plane of the eye producing an overall scattering with equivalent characteristics as the measured one. Thus, the parameters of the equivalent diffuser computed with this method may not represent an accurate estimator of a specific surface in cases in which the scattering results from the contribution of many surfaces with different diffusing characteristics in the eye.

## 2.2.4 Other methods

### Method based on reflectometric measurements

Purkinje images has been used to obtain the characteristics of lens surfaces, and in the case of cataract patients, an associated scatter halo [91]. Here, the third Purkinje image corresponds to light reflected by the anterior lens surface. In the case of rotational symmetry in the recorded image, the intensity distribution can be fitted to a function of the form

$$\langle I(\rho) \rangle = A^2 \frac{2\pi r_o^2}{Sk^2\sigma_\psi} \left( 1 + \frac{r_0^2\rho^2}{\sigma_\psi^2 f'^2} \right)^{-3/2} \tag{2.16}$$

where  $A$  is a constant,  $S$  is the pupil area,  $f'$  represent the focal length,  $k$  accounts for the wave number,  $\rho$  is the spatial radial coordinate,  $r_0$  is the correlation length, and  $\sigma_\psi$  is proportional to the roughness of the surface. The authors used these measurements in combination with computations for the speckle contrast to obtain values of roughness with information on the properties of the surface producing scattering.

### Method based on double-pass optical integration

Recently, Ginis *et al.* have proposed a method to measure intraocular forward scattering [92] using the concept of double-pass optical integration [2]. In this method, an extended light source formed by two concentric zones is projected on the ocular fundus. The zones of the light source correspond to a disk of 3 visual degrees in radius and an annulus which varies from 3 to 8 degrees in visual angles temporally modulated at different frequencies. The system is completed with a series of optical elements that allow the projection of the light onto the retina using two spatially-separated regions of the pupil for the illumination and measurement optical path. This configuration is used to avoid the influence of backscattered light during the quantification of scattering. The intensity at the center of the extended source is measured at a plane conjugated to the fundus. The differences in modulation frequency enable the extraction of information about the intensity for the disk ( $I_d$ ) and the annulus ( $I_a$ ) after a spectral analysis of the measured signal. The PSF at the middle of the angular range between the disk ( $\theta_1$ ) and the outer angular zone of the annulus ( $\theta_2$ ) is then computed as

$$PSF_{DP} = \frac{1}{2\pi\theta_s} \frac{1}{\theta_2 - \theta_1} \frac{I_a}{I_a + I_d} \quad (2.17)$$

where  $\theta_s = (\theta_2 - \theta_1)/2$ . Then, the parameter with information on intraocular scattering is obtained as

$$S = \frac{\theta_s^2 PSF_{DP}}{2} \quad (2.18)$$

The main advantage of this method relies on the fact that it uses zones of the PSF that are usually not available in the conventional double-pass technique, but that contain relevant information on scattering. Moreover, the small diameters of the beams interacting with the optics of the eye permit minimizing the impact of aberrations during the computation. Nevertheless, it should be mentioned that this technique provides information on the intraocular scattering affecting the small zones of the eye lens with which light interacts during the measurements. Therefore, spatial variations in the scattering properties of the eye may not be considered during the quantification.

## 2.3 Speckle reduction

Speckle is a phenomenon that affects measurement techniques based on light reflections in the ocular fundus, such as double-pass instruments and Hartmann-Shack wavefront sensors [20, 93]. In general, speckle appears when coherent light is reflected by rough surfaces [94]. In double-pass systems, the parameters for the optical quality of the eye are derived from the incoherent version of the image (without speckle) [13]. In the case of Hartmann-Shack sensors, the presence of speckle noise may induce variations in the centroids within the spot array pattern used to estimate the wavefront slopes. Therefore, speckle reduction is an important issue in the field of visual optics. Speckle reduction has been accomplished by different authors using a limited number of techniques. In the following paragraphs, we present a review of the techniques that have been implemented for this purpose in double-pass and Hartmann-Shack systems.

### Time diversity

The first methods for speckle reduction in systems based on retinal reflection were based on time diversity [20]. In this methodology, a number of coherent speckle patterns are averaged to obtain a noise reduction. The averaging process is done by adding short-exposure frames or by extending the integration time during image recording. In visual optics, this methodology is possible because the eye is a time-varying system producing incoherent speckle patterns over time.

Time diversity may be the easiest manner to obtain images without the effects of speckle because it does not require additional lenses or devices to enable the noise reduction. As a result, longer times are needed to record enough image frames with uncorrelated speckle patterns; otherwise, the reduction would not be fully. In this sense, movements of the subject or microfluctuations of accommodation during image recording may lead to inaccuracies in the computed estimators.

### Scanning mirrors

The time (or number of images) needed to obtain enough uncorrelated patterns to reach speckle reduction may be reduced with scanning mirrors [9]. To do this, a mirror is placed in a plane conjugate with the pupil of the eye within the optical path of light. When the

light travels towards the eye, the scanning mirror produces changes in the orientation of the light. As a consequence, the laser spot scans a region in the ocular fundus at the oscillation frequency of the mirror. After this, the mirror descans the light reflected by the fundus. In this manner, there is no apparent movement of the light after being descanned by the mirror. If the changes in orientation printed into the light by the scanning procedure are enough to scan uncorrelated positions in the fundus, the speckle may be reduced. Thus, it is possible to obtain double-pass or Hartmann-Shack images with reduced speckle.

The scanning mirrors method for speckle reduction is based on mechanical movements. Therefore, the main disadvantage of the method is the possible induction of mechanical vibrations in other devices or in the whole system. If the vibrations are strong enough, they may be perceived by patients. Moreover, the vibrations may induce misalignments of other optical elements.

### **Rotating diffusers**

When speckle is reduced by rotating diffusers, light is focused onto a diffusing material mounted on a rotating motor [38]. After passing through the diffuser, the beam is collimated again before it reaches the eye. As a consequence of the rotating diffuser, the light focused on the ocular fundus consists of a series of random patterns producing a partially incoherent beam. When the diffuser produces changes in the light reaching the retina at sufficiently high frequency and amplitude, the recorded double-pass or Hartmann-Shack images contain reduced amounts of speckle.

The implementation of this method for speckle reduction requires a special stage for collimation in the setup. In this sense, instruments with this configuration may increase in size. In laboratory conditions it should not represent any drawback. However, in commercial instruments the final size of the instrument may be a point to be considered.

### **Wavelength diversity**

According to Goodman [94], speckle can be reduced with changes in optical paths produced by light sources with multiple wavelength components. When the bandwidth of the laser source is large enough, the light reflected by the rough surface will be formed by dependent speckle patterns, which in turn results in speckle reduction.

In visual optical, wavelength diversity has been implemented by using light source with ex-

tended bandwidths, such as that delivered super-luminescent diodes (SLD). For instance, the setup introduced in [9] used an SLD at 780nm and 20nm in bandwidth. The results presented by the authors suggest that light sources with these characteristics are not enough to break completely the coherence of light in systems based of reflections in the ocular fundus. Although different authors have implemented instruments using light sources with extended bandwidth [53, 78, 95], it is not clear whether the speckle is suppressed from their use. In this sense, SLDs with larger bandwidths could be used to reach the speckle reduction. However, the price of SLDs is higher than that of conventional laser sources.

### **Acoustic modulators**

The use of acoustic modulators has permitted the reduction of speckle in visual optics using Hartmann-Shack sensors [96]. Under this concept, an acoustic cell is placed within the optical path in front of the laser source. When light traverses the acoustic cell, it interacts with standing sound waves. As a result of this process, the increment in the spot size, angular spreading, and temporal modulation is used to record an averaged spot array pattern with reduced speckle.

The acoustic modulator used in this method for speckle reduction is formed by a water filled box. A set of piezoelectric transducers are glued to the box and then biased with a sine wave generator to create a standing acoustic wave within the cell [97]. Using this setup, it is possible to generate the changes in the incoming light that are necessary to reduce speckle. The results presented by the authors suggest that this method can be applied in wavefront sensors for the human eye. Nevertheless, it is still necessary to study its behavior in instruments based on other techniques.



## Chapter 3

# The MEOQ system

Optical characterization of the eye is of great interest because it offers a tool to describe and analyze the formation of images on the retina. Moreover, the impact of this knowledge is increased when it is used for diagnosis and treatments of visual diseases. In this sense, the implementation of measuring systems able to provide complementary and comparable information in an accurate manner about the different phenomena involved in vision could increase our understanding on the optical properties of the eye and, in this way, brings us closer to its full optical description. The use of systems integrating multiple techniques (multimodal systems) arises as a natural option for this purpose<sup>1</sup>. In this kind of apparatus, a combined analysis of data from the multiple implemented configurations may be used to complement information about the optical characteristics of the eye.

With the idea of performing a comprehensive evaluation of the optical quality of the human eye, the Multimodal Eye's Optical Quality (MEOQ) system has been designed, implemented, and validated. It implements a double-pass instrument and a Hartmann-Shack sensor, so that it provides not only overall estimations on the optical quality but also information about aberrations. Moreover, combined analysis of data derived from these multiple modes allows a detailed quantification of the effects of scattering. As shown in figure 3.1, the MEOQ system is binocular and works in open field. Thus, the determination of the eye's optical quality is performed in normal viewing conditions. Additionally, the instrument is able to compensate for spherical and astigmatic refractive errors by changing the optical power of tunable devices.

This chapter introduces the MEOQ system and presents an extended version of the results

---

<sup>1</sup>Different authors have presented instruments that integrate multiple assessment modes. A review of those works can be found in the State of the art (chapter 2).



prism mirror  $M_1$ , and light going to the left and right eye is processed separately by two branches of identical optical elements. For the sake of clarity, only one of the branches is described.

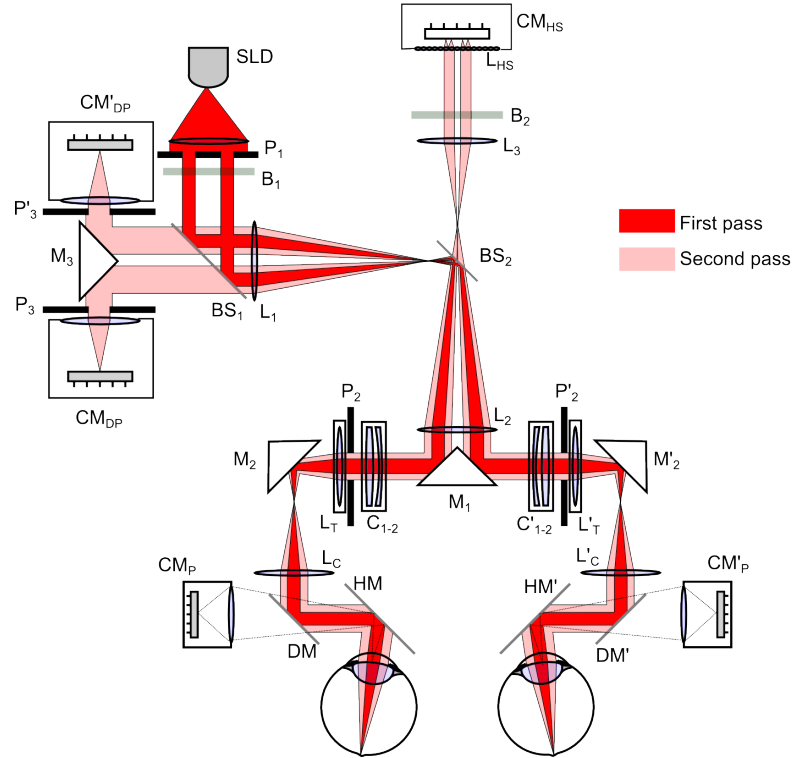


**Figure 3.2:** Diagram of the MEOQ system. The optical path of light from the *SLD* to the eyes (first pass) and the one from the eyes to the double-pass and Hartmann-Shack sensors (second pass) are indicated by colors. Labels of optical devices correspond to the nomenclature used in the text.

Continuing with the description, astigmatism is compensated by controlling the angle between two ophthalmic astigmatic lenses of identical prescription<sup>2</sup>  $(+2, -1, \theta^\circ)$  composing the lens set  $C_{1-2}$  [99]. The corrector is just before the focus tunable lens  $L_T$ , located in a plane conjugated to the entrance pupil of the system. The combination of  $L_T$  with the lens of fixed optical power  $L_C$  forms the spherical refractive error corrector [39]. The focal distance of  $L_T$  varies from around 45 to 120mm, while the one of  $L_C$  is 75mm. The distance between lenses  $L_T$  and  $L_C$ , and between  $L_C$  and the pupil plane of the eye is 150mm, twice the focal distance of lens  $L_C$ , so that  $L_T$  is also in a plane conjugated to the pupil of the eye. Mirrors  $M_2$ ,  $DM$ , and  $HM$  are used to direct light to the eye. In addition, the dichroic mirror  $DM$  allows camera  $CM_P$  to monitor the pupil position while the eye is illuminated by a series of light-emitting diodes at 980nm. On the other hand, transverse displacements and angular rotations of hot mirror  $HM$  are used to control the interpupillary distance and the angle of incidence of light,

<sup>2</sup>Lens prescription is given as  $(S, C, \theta)$ , where  $S$  and  $C$  are, respectively, the spherical and astigmatic refractive powers in units of diopters and  $\theta$  represents the orientation of the astigmatic axis in degrees.

respectively.

After entering the eye, the light is focused on the retina. There, the different structures produce scattering back towards the pupil [100], marking in this way the beginning of the second pass. Following an optical path identical to that of the first pass, light arrives to the circular aperture  $P_2$  of 6mm in diameter located just after lens  $L_T$ . When the natural pupil of the eye is larger, this aperture avoids overlapping of the light from the two eyes after light is redirected by  $M_1$  towards the telescopic systems  $L_2 - L_1$  and  $L_2 - L_3$ . In the former case, light reflected by  $BS_2$ , transmitted by  $BS_1$ , and redirected by prism mirror  $M_3$  reaches circular apertures  $P_3$  and  $P'_3$  of 4mm in diameter. These apertures act as exit pupils and are located in front of cameras  $CM_{DP}$  and  $CM'_{DP}$ , which record, respectively, double-pass retinal images of the left and right eye both using objectives of 100mm. In the case of the Hartmann-Shack configuration, light transmitted by  $BS_2$  is collimated by lens  $L_3$  of 100mm in focal length and filtered by linear polarizer  $B_2$ , which in combination with the crossed polarizer  $B_1$  allows for the elimination of corneal reflection in Hartmann-Shack images. Due to the magnification of the telescope system and the extent of  $P_2$ , the resulting beams are 4mm in separation and 3mm in maximum diameter. This configuration permits the use of the single micro-lens Hartmann-Shack array  $L_{HS}$  followed by camera  $CM_{HS}$  to sample the pupils of both eyes simultaneously.

### 3.1.1 Light source and its effects on the retina

The MEOQ system uses the commercially available super-luminescent diode Superlum SLD-37-HP2-DIL-SM-PD as light source. Originally, the reason of its selection was the broader spectral bandwidth that it presents compared with the one offered by conventional laser diodes. It is known that light sources of broad spectrum can be used to reduce speckle noise [94]. In the case of systems based on retina reflections, the required bandwidth to produce uncorrelated speckle patterns is a function of  $\sigma_z$ , the standard deviation of the equivalent surface height fluctuations produced by the retina. Following the formulation presented by Goodman [94] and Yamaguchi et al. [101], the bandwidth that is required to produce uncorrelated speckle patterns is given by

$$\Delta\lambda \approx \frac{\lambda^2}{2\sigma_z} \quad (3.1)$$

Considering fluctuations of  $\sigma_z = 1.88\mu\text{m}$ , the application of equation 3.1 for a central wavelength

of  $\lambda = 801\text{nm}$  indicates that a bandwidth of  $\Delta\lambda = 170\text{nm}$  would be necessary to reduce speckle in systems based on reflections of light from the retina<sup>3</sup>. However, the maximum bandwidth offered by the light source is  $37\text{nm}$ , which is much smaller than the required one<sup>4</sup>. Despite this fact, the SLD is still suitable for our purposes since its power is enough to compensate for the optical losses impinged by beam splitters and retinal reflections. On the other hand, the parameters with information on the optical quality may vary for different wavelengths [103]. Thus, we expect that the small bandwidth does not have a major impact on the computations.

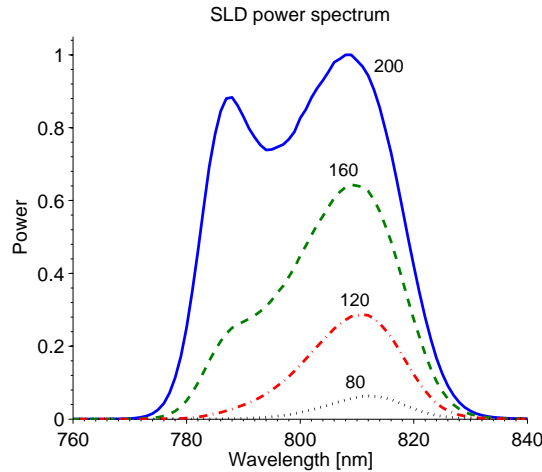


**Figure 3.3:** Experimental measurements of SLD power spectrum for different bias currents. The curves are labeled in [mA] and normalized to the maximum measured power.

Measurements of the SLD spectrum show that both the spectral center and bandwidth change with bias current, as observed in figure 3.3. For instance, the Full Width Half Maximum (FWHM) goes from 16 to  $37\text{nm}$  for SLD currents between 80 and  $200\text{mA}$ , while the central wavelength varies from  $812$  to  $801\text{nm}$ . This variation represents a spectral shift of around 1% only. When using the MEOQ system for assessing the optical quality of real eyes, the SLD is biased with currents ranging from 80 to  $140\text{mA}$ . Despite of the small changes within this range, a wavelength of  $\lambda = 801\text{nm}$  is used during computations.

<sup>3</sup>The required bandwidth was computed assuming a tentative value of height fluctuations taken from simulations of scattering produced by photoreceptors [102]. On the other hand, light sources of broad spectrum can be combined with the time-variant behavior of the eye to reduce the bandwidth that is necessary to obtain images unaffected by speckle for a given integration time in the recording device.

<sup>4</sup>The central wavelength of  $801\text{nm}$  and the spectral bandwidth of  $37\text{nm}$  used here were measured at  $200\text{mA}$ . Such values were obtained experimentally and fit those provided by the manufacturer through the Acceptance Test Report of the device.

### Prediction of temperature and likelihood of damage

Double-pass and Hartmann-Shack systems are based on reflection of focused light on the retina. This intentional exposure of the eye to laser light causes changes in the temperature of the irradiated area and may provoke damages when its power and the exposure time exceeds certain thresholds. Moreover, the effects differ from one wavelength to another due to the different absorption values within the retinal pigment epithelium (RPE) region of the retina [104]. From this, any system based on retinal reflections must operate under conditions that do not cause damage to the eyes.

In the MEOQ system, collimated laser beams of around  $w = 2\text{mm}$  in diameter enter the eye. Experimental measurements of the incident power at the pupil planes indicate that the left and right eyes are exposed to  $0.760$  and  $0.782\mu\text{W}$ , respectively<sup>5</sup>. Considering the width of the central lobe of the Airy pattern given by equation 3.2 [16] for  $\lambda = 800\text{nm}$  and  $f = 16.7\text{mm}$ , the incident powers are focused on the retina in spots of around  $16\mu\text{m}$  in diameter. When measuring the optical quality, the eye is typically exposed to laser light for times between 5 and 20s distributed as follows: 4 to 19s to align the subject with the instrument and around 1s to record double-pass and Hartmann-Shack images. However, the measured power corresponds to an energy density at the pupil plane of around  $0.24\text{Wm}^{-2}$  for both eyes, which is a value much lower than  $15.92\text{Wm}^{-2}$ , the Maximum Permissible Exposure (MPE) defined by the standard ANSI Z136.1 [105].

$$d = 1.22 \frac{\lambda f}{w} \tag{3.2}$$

The temperature increment and the likelihood of damage caused by the MEOQ system were computed using a three-dimensional thermo-dynamic model of the human eye. The model has been developed at Karlsruhe Institute of Technology (KIT-ITIV) and its use is the result of the collaboration between this institute and the Polytechnic University of Catalonia (UPC-CD6) within the framework of the program Europhotonics. The model takes into account the geometry of the eye and considers blood flow in the choroid, which can influence the results in the case of long irradiations times. To predict the temperature, the model computes the energy absorbed at different regions of the retina for a given wavelength over time. From these data, the tissue damage is estimated using the Arrhenius integral given by equation 3.3, where  $\tau$  is the exposure time,  $E_a$  the activation energy,  $R$  the universal gas constant,  $T$

---

<sup>5</sup>Data measured for a SLD current of 100mA

the temperature during exposure, and  $A$  a scaling factor. The integral presents a unity value when there are retina damages. Further details on the model are out of the scope of this work, but can be consulted in the work of Heussner et al. in [104].

$$\Omega = A \int_0^{\tau} \exp \left[ -\frac{E_a}{RT(t)} \right] \quad (3.3)$$

Using the parameters for the MEOQ system, the temperature increment and the evolution of the Arrhenius integral were computed for times between 0 and 20s. For the simulations, an incident power on the retina of  $1\mu\text{W}$  in a spot of  $16\mu\text{m}$  of diameter was considered. To complete the model, absorption within a  $5\mu\text{m}$  RPE of 15% and blood perfusion of  $0.005\text{ms}^{-1}$  in the choroid was considered. Figure 3.4a shows the radial profile of the calculated temperature increment after 20s. As expected, the maximum temperature is observed at the center of the exposure and the values vanish as a function of the radius. More important than the temperature increment, the Arrhenius integral presents values much lower than unity, as observed in figure 3.4b. The results of the simulations indicate a small likelihood of damage, even for the long exposure times used in the analysis. These figures suggest that the MEOQ system can be used for measuring the optical quality of the eye while keeping its effects on the retina negligible.

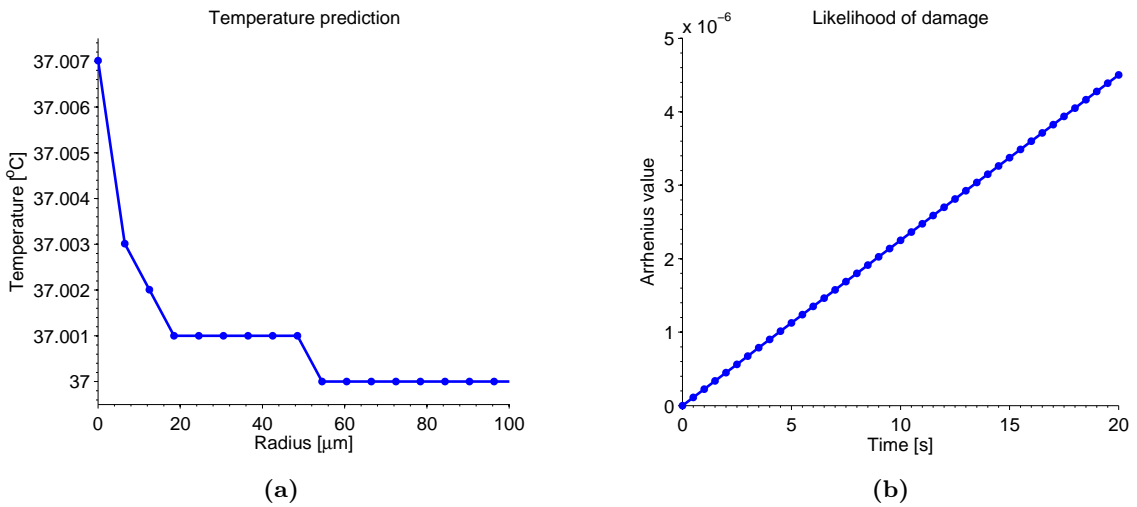


**Figure 3.4:** Temperature prediction after 20s of exposition and likelihood of retina damage in function of time for the MEOQ system.

### 3.1.2 Binocular open-view configuration

The MEOQ system is able to analyze both eyes simultaneously thanks to its binocular configuration. Furthermore, the open field of view design permits the system to perform an optical characterization of the eyes in normal visual conditions. In the case of binocularity, it is achieved through the generation of two collimated beams, one for each eye, that reach the pupil of the eyes after being translated by a single telescopic system and compensated independently for low order aberrations.

The two-beam generation is reached by passing collimated light through a diaphragm at the entrance pupil plane of the system composed of two-horizontally aligned circular apertures of 1.8mm in diameter and 8mm in center-to-center separation. Considering the ratio between areas of the output to the input beam, only 0.1% of the incident energy reaches the eye. However, the laser source allows compensating for these losses. On the other hand, prism mirrors are used to separate (join) the optical path of beams when necessary: before (after) compensating for low order aberrations within the first (second) pass and before reaching the cameras that record the double-pass images. One advantage of using beams with small center-to-center separation is that single optical devices with proper diameters can be used to process simultaneously light going to or coming from both eyes. This characteristic is used in the telescopic systems. They are formed by optical elements of clear apertures of 25.4mm diameter. The beam generation, translation, and separation processes are illustrated in figure 3.5. In the case of the Hartmann-Shack sensor, a telescopic system with a magnification of  $|M| = 0.5$  allows to use a single lenslet array of 25.4mm in diameter followed by a CMOS sensor of  $6.78 \times 5.25$ mm. The sensor size, the center-to-center beam separation, and the system magnification permits the assessments of pupils up to 5.56mm in diameter.

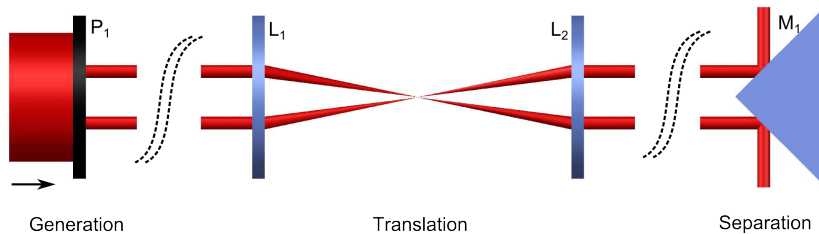


**Figure 3.5:** Schematic of the beam generation, translation, and separation processes in the MEOQ system.

Once the beam is separated, light is processed by two identical optical paths formed by an astigmatism and a defocus corrector, and the necessary mirrors to direct light to the eye. These elements are mounted in a two-level module that allows the system to work in open field and to compensate for low order aberrations independently. Referring to figure 3.6, the subject

is asked for looking at a target through hot mirrors  $HM$  and  $HM'$  during measurements. These mirrors are mounted in a kinematic mount that permits the variation of the angle  $\theta_i$  to fit the angle of incidence of light with the visual axis. The system allows simultaneous transversal translations of the mirrors with respect to the pupil plane. In this way, when  $HM$  and  $HM'$  are moved forward or backwards, the interpupillary distance is increased or decreased, respectively. The system is configured in such a way that permits measurements for interpupillary distances between 50 and 70mm.

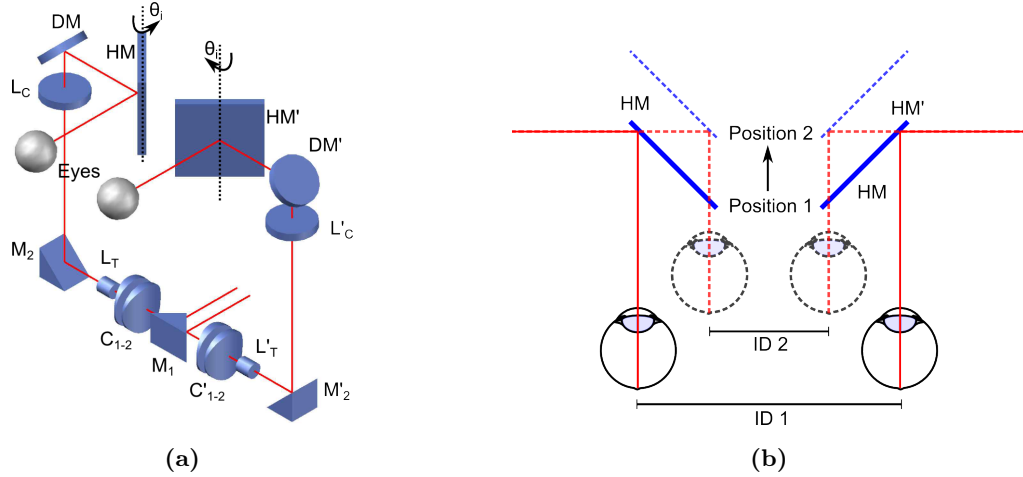


**Figure 3.6:** 2-levels module (a) and control of interpupillary distance ID (b) in the MEOQ system.

The manner in which binocularity is reached in the implemented configuration presents a series of advantages with respect to other configurations. An easiest way to obtain a binocular system is through element duplication. However, the fact of sharing elements for measuring both eyes reduces considerably the cost of the system. Besides sharing the majority of the optical elements, a single light source and Hartmann-Shack camera is used to obtain data for the left and right eye simultaneously. However, the magnification of  $|M| = 0.5$  reduces the capabilities of the wavefront sensor. The element duplication was not avoided in the case of double-pass cameras and in the refractive error correctors. Nevertheless, we consider that the implemented system is robust and will permit diverse type of studies on binocularity.

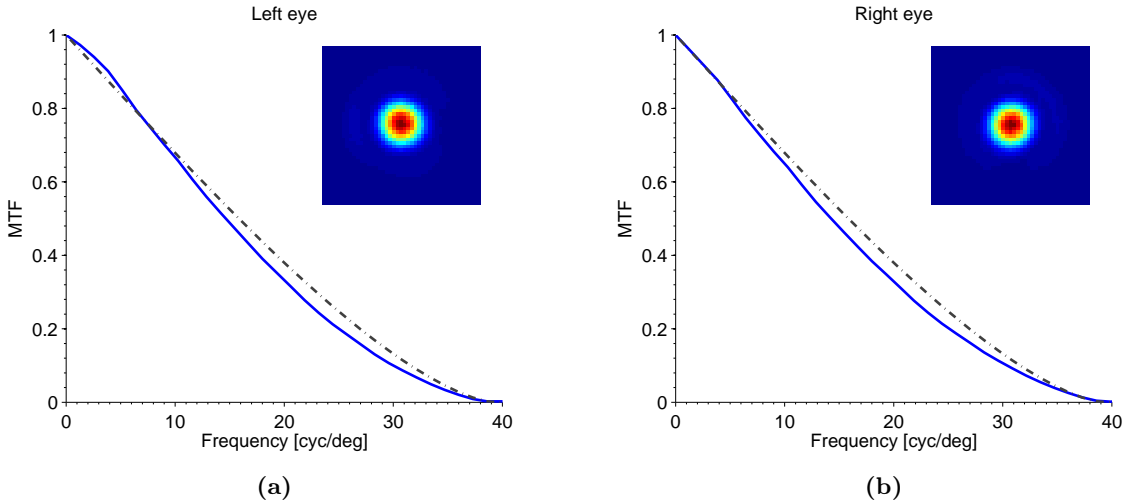
### 3.1.3 Multimodality

Within the context of this work, multimodality is understood as the ability of the MEOQ system to deliver information from two different modes: the double-pass and the Hartmann-Shack technique. To implement the former mode, a configuration with unequal entrance and exit pupils is used [13]. The double-pass spread function is measured independently for the left and the right eye with two CMOS cameras. In the case of the aberrometer, a magnification

of  $|M| = 0.5$  allows to record images with information on the wavefront aberration of both eyes with a single CMOS sensor.

### Double-pass characterization

During image recording, the double-pass sensors use commercially available CMOS cameras UI-1240ML-NIR. The spatial resolution of the double-pass images is limited by the spacing between pixels ( $5.3\mu\text{m}$ ) or, considering the camera objective,  $0.182\text{arcmin}$ . During the data processing, images of  $256 \times 256$  pixels are processed, so that the system examines data of  $46.592\text{arcmin}$  in extension. For the diffracted limited case, more than 80% of the energy is contained within the main lobe of the PSF [12], whose extension is around  $3.397\text{arcmin}$  for a pupil diameter of 2mm. Therefore, we consider that the processed image contains relevant information to determine the eye's optical quality. In the Fourier plane, the extension of the image results in a resolution of  $0.737\text{cyc/mm}$  or, equivalently,  $1.281\text{cyc/deg}$ .



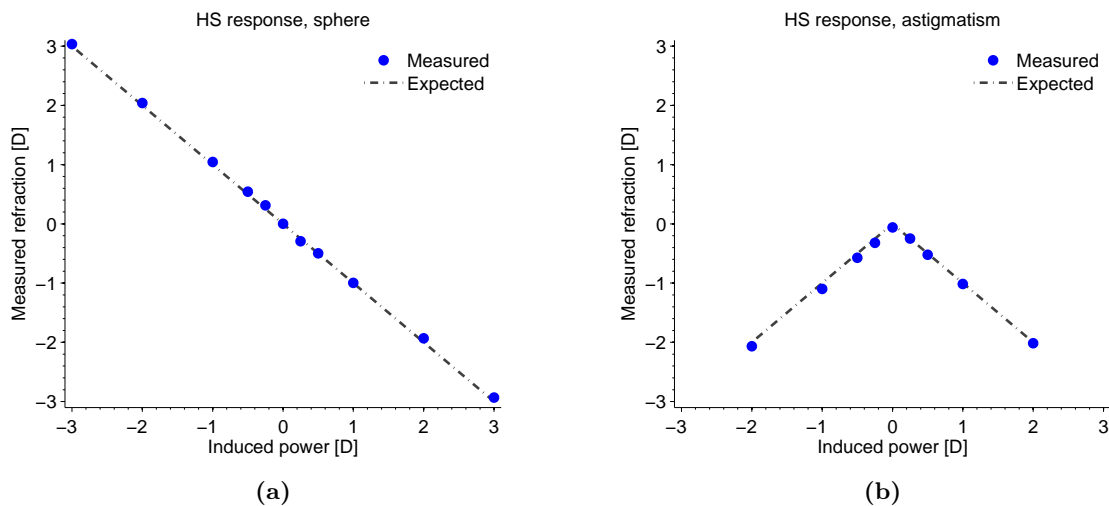
**Figure 3.7:** Double-pass response for a mirror placed at the pupil plane of the MEOQ system. The solid and the dashed line correspond to the measured MTF and the one expected for a pupil of 1.8mm in diameter. The images within the graphs are  $8 \times 8\text{arcmin}$  cropped versions of the recorded images.

Figure 3.7 shows the response of the system for a mirror placed at the output pupil plane for the best optical quality (narrowest spot). The recorded images represent the point-spread function after the light passes twice through the system for the entrance pupil diameter. The MTF was computed by Fourier transforming the images and applying a peak correction [43] by extrapolating the zero frequency from curve fitting using two exponential functions [106]. The computed Strehl ratios of 0.954 and 0.940 for the left and right branches of the system, respectively, reveal that the it is diffraction limited according to the Marechal criterion for

image quality<sup>6</sup> [12].

### Hartmann-Shack characterization

The Hartmann-Shack sensor consists of lenslet array 0200-6.3-S-C (Adaptive Optics Associates) followed by the CMOS camera UI-1241LE-NIR-GL (IDS). The microlenses of 6.3mm in nominal focal length are arranged in a rectangular grid with a lens pitch of  $200\mu\text{m}$ . Taking into account the magnification of the system, a 4mm pupil is sampled with around 78 lenslets. The number of Zernike coefficients that can be adequately calculated is approximately the same as the number of lenslets [47]. Since the majority of the higher order aberrations can be described with eight order (42) Zernike coefficients [17], we found the sampling resolution enough for our purposes. Regarding the wavefront slope, the focal length of the lenslets and their pitch permit measurements of wavefront slopes  $\theta$  in the range of 0.048 to 0.910deg.



**Figure 3.8:** Hartmann-Shack response for different induced spherical (a) and astigmatic (b) aberrations.

The response of the Hartmann-Shack sensor was experimentally measured. To do this, the output of the MEOQ system was illuminated with a collimated laser beam to measure its second pass response. After alignment of the laser, trial lenses with spherical and cylindrical power were placed in front of the laser to induce known aberrations. Thus, 11 (9) cases between  $-3$  and  $3\text{D}$  ( $-2$  and  $2\text{D}$ ) were measured with the HS sensor for the induced spherical (cylindrical) power. Figure 3.8 shows the average of ten measurements. The standard deviation among measurements is not shown in the figure, but it remained smaller than  $0.015\text{D}$  ( $0.034\text{D}$ ). Since the Hartmann-Shack sensor provides the value that is needed to compensate

<sup>6</sup>An Strehl ration of 0.8 correspond to the Marechal criterion for diffraction limited image quality.

for the current refraction, a negative slope is observed for the spherical refraction. In the case of the astigmatism, the positive values of computed refraction are converted into negative equivalent lenses. Based on these results, it can be assured that the HS sensor of the MEOQ system provides representative estimates for refraction.

### 3.1.4 Spherical refractive error compensation

Spherical refractive errors are compensated with correctors based on lenses of variable focal lengths, as proposed by Sanabria et al. [39]. The corrector is shown in figure 3.9 and is composed by a lens  $L_T$  of tunable focal length followed by a compensating lens  $L_C$  at twice its focal distance  $f_C$  from the tunable device and the pupil of the eye. In this manner, collimated light passing through lens  $L_T$  is translated by lens  $L_C$  to the pupil plane, where the beam presents a constant diameter, but with vergences in function of the focal length of the tunable lens.

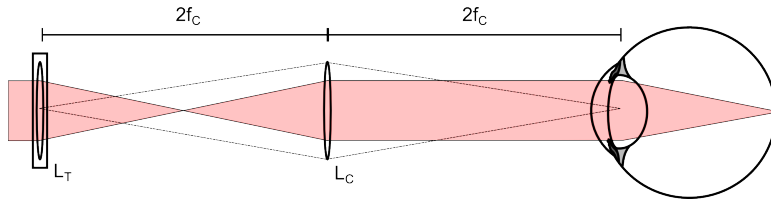


**Figure 3.9:** Model of the spherical refractive error corrector.  $L_T$ : tunable lens,  $L_C$ : compensating lens,  $f_C$ : focal length of lens  $L_C$ .

The MEOQ system uses the commercial electro-optical liquid lens EL-10-30-NIR-LD (Optotune) as tunable device. This lens allows users to set back focal distances between 45 and 120mm by varying the current flowing through an electromagnetic actuator that modifies the pressure of the optical fluid in the lens [107]. Besides making it possible to have the tunable lens and the pupil in conjugate planes, the compensating lens shifts the range of correction for the device. By applying the Gaussian lens formula modeled by equation 3.4 sequentially over the lenses until finding the equivalent optical power of the corrector at the exit pupil plane<sup>7</sup>, it is found that the lens  $L_C$  of  $f_C = 75\text{mm}$  used in the MEOQ system would permit compensations for spherical refractive errors between +8.52 and  $-5.00\text{D}$ .

<sup>7</sup>In the formula,  $f$  is the focal length and  $s$  and  $s'$  are respectively, the object and image distances from the principal planes [11]. Regarding the sign convention,  $s$  and  $s'$  are positive when they are, respectively, on the left and right side of the lens for light entering from the left.

$$\frac{1}{f} = \frac{1}{s} + \frac{1}{s'} \quad (3.4)$$

Tunable lens based correctors and traditional Badal optometers can be used in double-pass configurations to determine the optical quality of the eye [39]. We use the former instead of the latter method because it makes possible to have a more compact binocular system to perform faster corrections and posterior measurement of the eye. However, its use introduces small deviations from ideal values as consequence of the physical changes induced in the lens to vary the focal length.

An electro-optical liquid lens is a tunable device that changes the curvature of one of its faces as consequence of the change in pressure in the optical fluid contained behind an elastic membrane. These shape variations provoke longitudinal shifts in the position of its principal planes, which in turn affects the position of the pupil plane and the magnification of the corrector. The magnitude of such displacements was estimated using the Zemax model of the tunable lens provided by the manufacturer. Table 3.1 presents the displacement of the second principal point<sup>8</sup>  $\Delta H_{2T}$  as well as its image distance from the compensating lens  $s'_C$  and the resulting magnification  $M_C$ . The image distance and the magnification were computed, respectively, with equation 3.4 and 3.5 for  $s = f - \Delta H_{2T}$ ,  $s' = s'_C$ , and  $f = 75\text{mm}$ .

$$M = -\frac{s'}{s} \quad (3.5)$$

**Table 3.1:** Variations in the second principal point  $\Delta H_{2T}$  of the tunable lens, its image distance from the compensating lens  $s'_C$ , and in the magnification of the corrector  $M_C$  for different focal lengths  $f_T$  of the tunable lens.

	$f_T = 45\text{mm}$	$f_T = 75\text{mm}$	$f_T = 120\text{mm}$
$\Delta H_{2T}$ [mm]	0.218	0	-0.293
$s'_C$ [mm]	150.219	150	149.708
$M_C$	-1.003	-1	-0.996

The effects in the beam and the variations in the spot size produced by the tunable lens can be visualized in the models and spot diagrams in figure 3.10. The small magnitude of the variations in the parameters of table 3.1 are in agreement with those presented by Sanabria et al. in [39] and confirm that spherical refractive error correctors based on tunable lenses can

---

<sup>8</sup>The rays are considered to be approaching the corrector from the left.

be used in our system. Since they depend on the pupil diameter, the changes in width of the central lobe in the Fourier plane and the cut-off frequency of the corrector are proportional to the computed magnification  $M_C$ , which presents a maximum absolute deviation of 0.4% with respect to the value for the central focal length of the tunable lens.

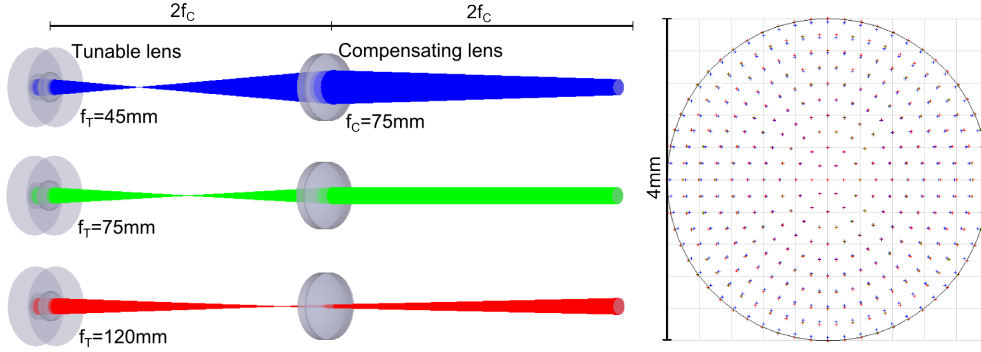


**Figure 3.10:** Model (left) and spot diagram at the exit pupil plane for an entrance pupil of 4mm diameter (right) for three different focal lengths in the tunable lens of the spherical refractive corrector.

In addition to the variable position of its principal planes, the tunable lens presents unwanted aberrations as consequence of the variable curvature of its face, the effects of gravity on the optical fluid, and other sources of random errors [107]. The data sheet of the tunable lens shows that it presents typical RMS wavefront errors of up to  $0.2\lambda$ , which could be shifted up  $0.4\lambda$  by the gravity induced Y-coma term<sup>9</sup> when the tunable lens is placed vertically. However, the Strehl ratios measured in reference [39] remained around 0.8 for all focal lengths. Furthermore, we consider that characterization curves of the spherical refractive error corrector can be used to countering somehow such undesired performance during the analysis of double-pass and Hartmann-Shack images.

### Experimental characterization

The response of the spherical refractive error corrector was experimentally measured during the calibration process of the MEOQ system. To do this, a collimated laser was used to illuminate the system from the eye pupil plane. Then, the equivalent sphere was measured with the Hartmann-Shack sensor for pupil diameters of 4mm. This process was done for currents between 0 and 300mA in steps of 30mA to obtain the performance of the corrector over the full range of optical powers of the tunable device. For each case, the sphere was

<sup>9</sup>Data obtained at 525nm and 8mm of clear aperture

measured every 30s until 10 values of refraction were obtained. Due to limitations in the dynamic range of the HS sensor, it was necessary for the extreme values of currents to place trial lenses of  $\pm 5D$  in front of the collimated beam to compensate for the sphere induced by the own corrector. However, this was considered and the values were corrected during data processing.

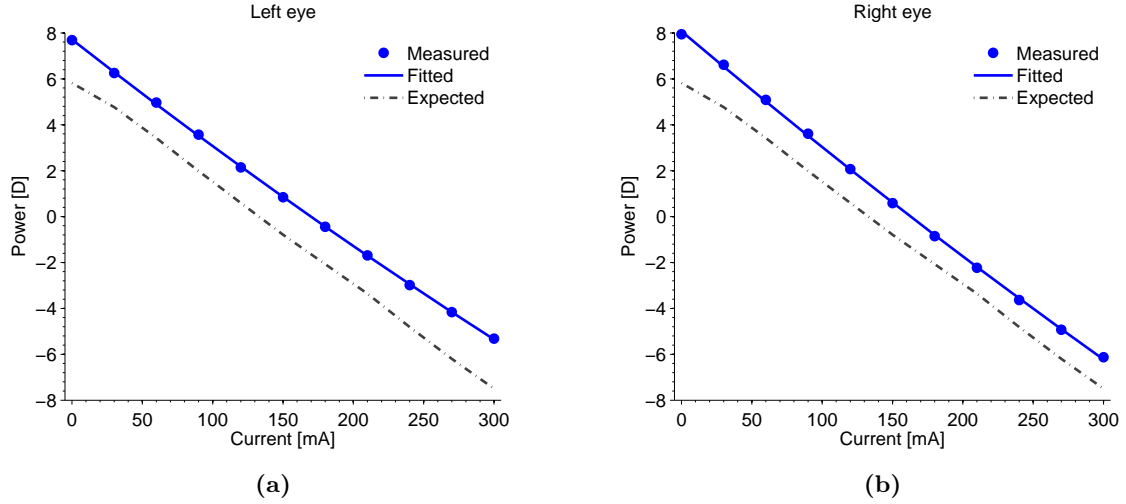


**Figure 3.11:** Characterization of the spherical refractive error compensator for the left and the right eyes. The measured (dots) and expected (dashed line) refractions are presented. The results of fitting the measured values are also showed in the plot (solid line).

Figure 3.11 depicts the expected and measured spherical equivalent refraction for both eyes. The former values were computed from data provided by the manufacturer though the characterization sheet of the tunable devices. As observed, the measured values represent a shifted version of the expected ones. However, it should be pointed out that the manufacturer provides focal lengths measured from the rear surface of the lens, whose position is not within the principal plane. In fact, simulations of the tunable device in Zemax indicate a separation of 3.68mm between principal plane and the rear surface. The experimental data suggest that MEOQ systems is able to correct spherical refractive errors from  $+7.68$  to  $-5.32D$  and from  $+7.94$  to  $-6.13D$  for the left and right eye, respectively. The experimental measurements have been fitted using a third-order polynomial model. This information is used during data analysis to provide an accurate value of refraction regardless of the current in the tunable device.

It is known that the optical power of the tunable devices present slight changes with temperature. According to the manufacturer, the optical power decreases  $\sim 0.6D$  and the resistance increases  $2\Omega$  per  $10^\circ C$  of temperature increment. Since the tunable devices are biased by

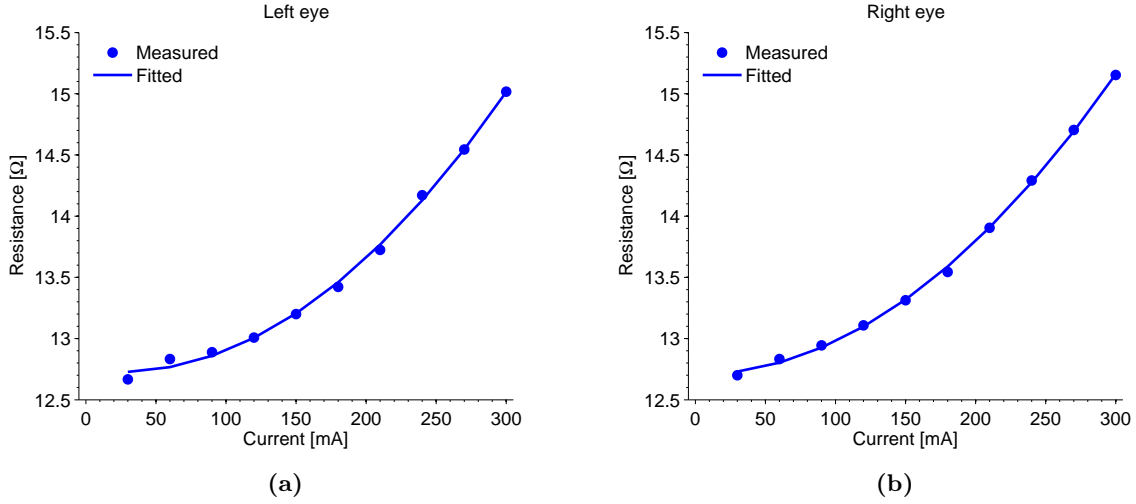


**Figure 3.12:** Resistance of the tunable lens for different bias currents. The measured values (dots) are presented along with their curve fitting (solid line).

a remote-controlled power supply, the voltage between terminals  $V$  and the current  $I$  were also sensed during this characterization. Computed as  $R = V/I$  the resistance of the tunable device is plotted in figure 3.12. These curves are used to apply a correction during the computation of wave aberrations to provide an accurate value of refraction. This is done by sensing  $R$  and  $V$  during measurements and applying a correction factor to the spherical refraction that compensates for the differences between the actual resistance and the one obtained for the characterization curves.

### 3.1.5 Astigmatic refractive error compensation

The corrector is based on two sphero-cylindrical ophthalmic lenses with identical optical power that are rotated one with respect to each other to generate the cylindrical power that compensates for the subject's astigmatism, as proposed by Arines and Acosta in Ref. [99]. Considering two lenses of prescriptions  $(S, C, \theta_1)$  and  $(S, C, \theta_2)$ , it is possible to generate effective cylindrical powers  $C_e$  between zero and  $2C$  depending on the angle between lenses  $\theta = \theta_2 - \theta_1$ . In this manner, the minimum and maximum values are reached when axes are oriented in a perpendicular or parallel manner, respectively. Since they present identical power, the axis of the resultant lens is equidistant to the axes of the original cylinders. Regarding the effective sphere  $S_e$ , it depends on the cylindrical power  $C_e$ , and its value changes when the lenses are rotated. The behavior of the effective cylinder, axis, and sphere can be modeled using equations 3.6-3.8.

$$C_e = 2C_L \cos\theta \quad (3.6)$$

$$\theta_e = (\theta_2 - \theta_1)/2 \quad (3.7)$$

$$S_e = 2S + \frac{2C - C_e}{2} \quad (3.8)$$

The astigmatism compensator was implemented by placing two sphero-cylindrical lenses of  $(+1, -2, \theta)$  in a stage that rotates them in opposite directions. Moreover, the orientation of the effective axis is controlled by rotations of the whole stage. The process for compensation is the following: first, the subject's prescription is measured with the Hartmann-Shack sensor; then, the magnitude of the effective cylinder is configured by setting the proper angle between lenses; finally, the whole stage is rotated to match the effective axis with the one that is necessary to compensate for the subject's astigmatism.

### Experimental characterization

The astigmatism compensator was experimentally characterized once mounted in the MEOQ system. The response in function of the orientation between lenses was measured with the Hartmann-Shack sensor while the system was irradiated from the eye pupil plane with a collimated laser. The refraction was measured 10 times for sweeps between  $-45$  and  $45$ deg in  $5$ deg steps. During the characterization, the orientation of the lenses was controlled by a step-to-step motor which allowed accuracy in angle positioning. The results of the characterization are presented in figure 3.13. By assuming accuracy in data provided by the HS sensor, the differences between the measured and the expected curves are attributed to the real power of the ophthalmic lenses. Since a third-order polynomial fitting of the experimental values is taken into account during compensation, these differences do not influence the astigmatism correction.

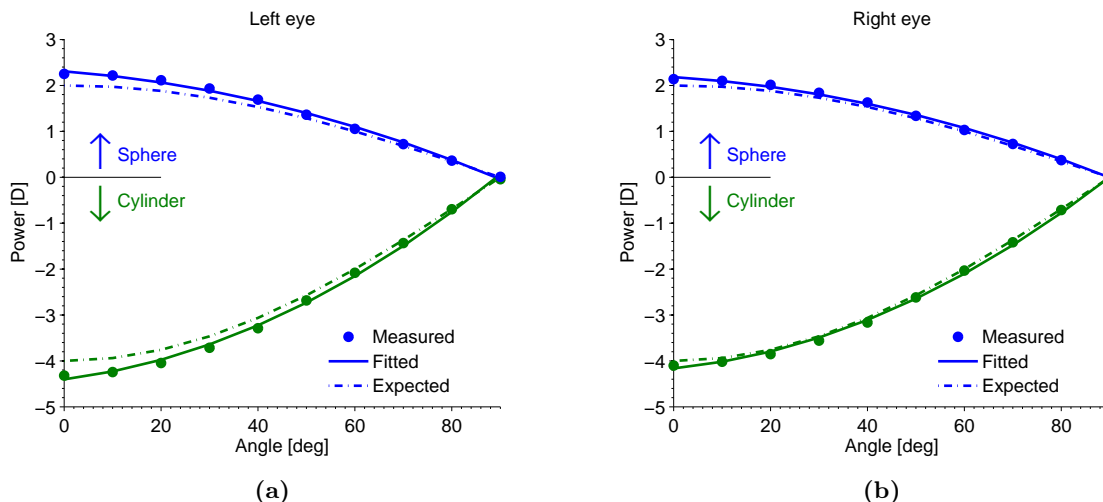


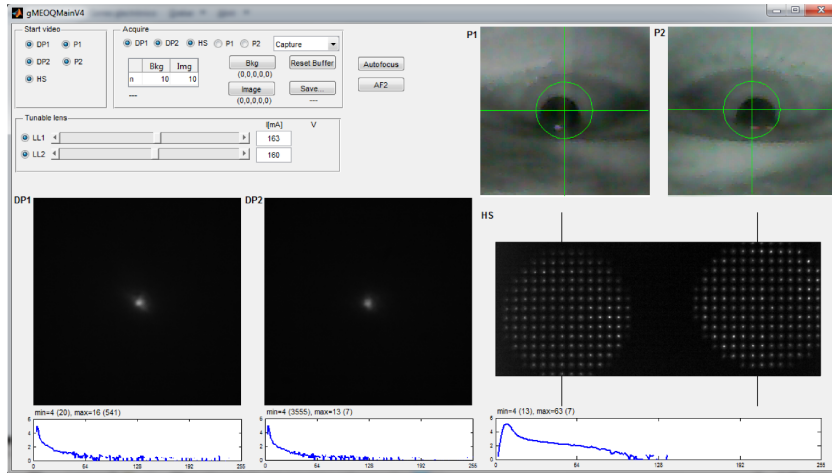
**Figure 3.13:** Characterization of the astigmatic refractive error compensator for the left and the right eyes. The measured (dots), fitted curve (solid line) and expected response (dashed line) are presented.

### 3.1.6 User interfaces and data processing

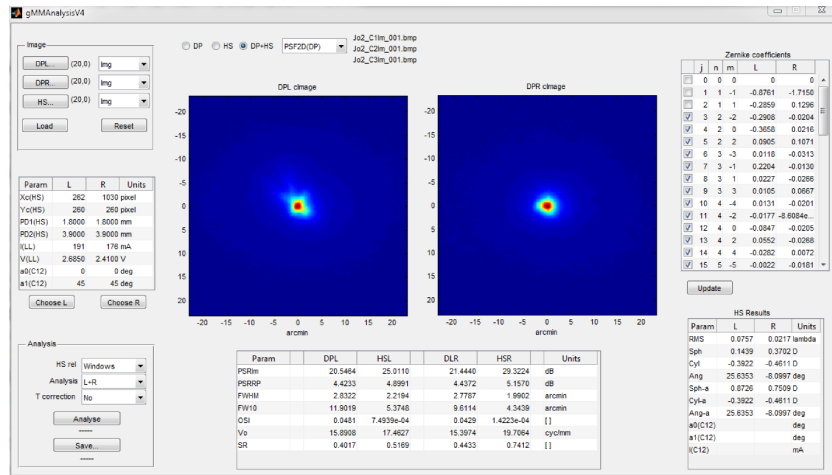
The remote controlled components, image recording, and data analysis are managed through a series of classes and graphical user interfaces specially developed in Matlab within the context of the MEOQ project. These components permit the operator a flexible configuration of the instrument by changing parameters either directly with the interfaces or in the corresponding configuration files. Once the subject under assessment is properly aligned with the measuring system, these tools make it possible to compensate for low order aberrations, to record DP and HS images, and to process multimodal data for both eyes in less than five seconds.

#### Remote control

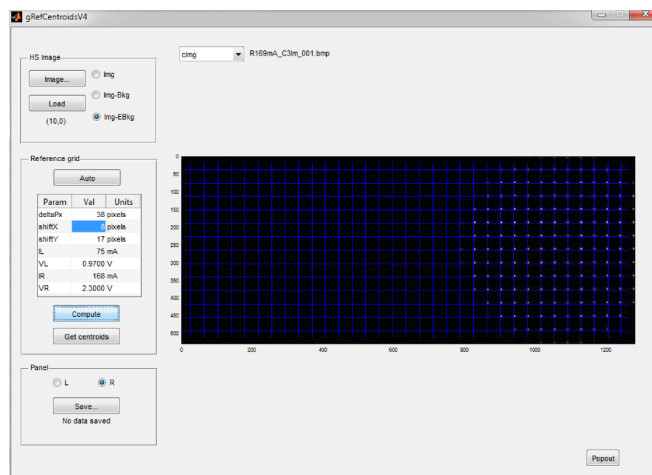
Cameras and tunable lenses are controlled through the interface gMEOQMain, shown in figure 3.14a. Once initialized, real-time video and the corresponding histogram are available for both the double-pass and the Hartmann-Shack cameras. A pop-out interface permits the configuration of, among others parameters, frame rate, integration time, background level, and gain. In the case of the pupil cameras, only real-time video is available. The current in the tunable devices is managed through the remote controlled power supply QL355TP (TTi). It is possible to change the output optical power with a series of sliders in the interface. Moreover, there is an option to find and set the current for the best optical quality by pressing the auto-focus option. When selected, the characterization curves of tunable devices presented in section 3.1.4 are considered to set the current that compensate for the refraction measured



(a) gMEOQMain



(b) gMMAAnalysis



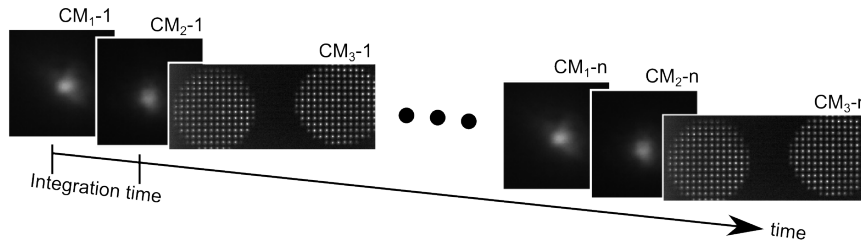
(c) gRefCentroids

Figure 3.14: Graphical user interfaces in the MEOQ system

with the HS sensor. This process is repeated 3 times or stopped if the error (difference between configured and measured power) goes below a fixed threshold (0.25D), but in general the process takes around 1s. Image recording is initialized by the operator. It is possible to modify the number of images per capture directly in the interface. Once recorded, the images are saved in a temporal file common to all the interfaces. Copies of the recordings are saved in the folder specified by the operator when requested.

### Image recording

When image acquisition is demanded, images for the selected cameras are recorded n-times following the sequence illustrated in figure 3.15. Although the images are captured strictly at different instants, the average of the n-images per camera contains information of the same period of time. Usually, the average of more than 10 recordings are processed. Thus, we consider that data derived from the averages can be compared because it includes information of the same short-period of time. The duration of the recording depends on the number of cameras selected, images per capture, and frame rate. The cameras permit a maximum frame rate of 25fps. Thus, when the three cameras are selected and 10 frames are saved, it takes  $3 \times 10 \times 0.04s = 1.2s$  to collect the images. Besides image recording, the values of current and voltage of the tunable lenses are also saved for their posterior usage during estimations of refractions.



**Figure 3.15:** Sequence followed during images recording. Data is recorded by intercalating frames of the cameras selected until capturing n-images for each of the imaging devices.

### Data analysis

Once the images have been recorded, the GUI gMMAAnalysis (figure 3.14b) is used to obtain information on the optical quality. The parameters used during the analysis can be modified through this interface. The images to be analyzed can be loaded from the temporal file

common to all the interfaces or browsed manually. When more than one file is available, the average image is considered during data processing. Zernike coefficients computed from HS images are used to obtain both the subject's refraction and the wave aberrations  $W_a$  for the first and second pass pupil diameters. The latter information is used to reconstruct the point-spread function (PSF) for pupils of 1.8 and 4mm by taking the square magnitude of Fourier transformed complex pupils of the form,

$$P(x, y) = A(x, y) \exp[ikW_a(x, y)] \quad (3.9)$$

where  $A(x, y)$  and  $k$  represent the amplitude and the wave number [16], respectively. To compare information between techniques, the double-pass point-spread function is obtained from HS data by convolving the PSFs for the first and second pass pupil diameters. After this, DP and HS information are processed in a similar fashion. First, the PSF is Fourier transformed to obtain the double-pass modulation transfer function (MTF). Then, the curves are analyzed to obtain information on the optical quality. The process followed during data analysis is described in the flowcharts of figure 3.16.

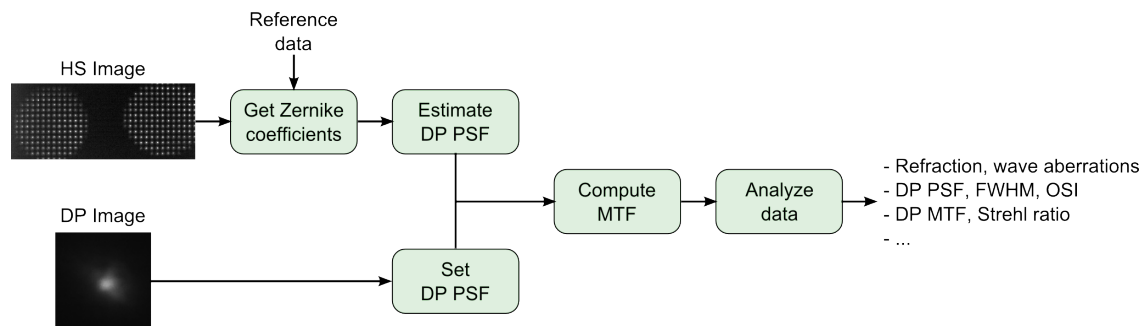


**Figure 3.16:** Flowchart indicating DP and HS data processing.

The results of the DP and HS analysis, such as PSF, MTF, and wave aberrations can be visualized directly in the interface gMMAAnalysis by selecting the proper option in a pop-up menu. Numerical results are also available in the GUI. Thus, the operator have direct access to Zernike coefficients, values of refraction, objective scattering indexes, Strehl ratios, FWHM values, among others parameters with information on the optical quality. The system is able to process monocular and/or binocular data either in a monomodal or multimodal fashion. In the case of Hartmann-Shack analysis, the associated interface gRefCentroids (figure 3.14c) is used during the determination of the searching windows and reference centroids, which are computed by finding the center of mass of the conjunct of spots in the HS image [50].

## 3.2 Instrument validation

Up to now, the MEOQ system (figure 3.17) has been presented and validated to some extent. For instance, the double-pass configuration presents a diffraction limited response for pupil diameters of 1.8mm, while the refraction measured by the Hartmann-Shack sensor match the values of trial lenses<sup>10</sup>. However, it is necessary to assure that DP and HS data can be compared with respect to each other to be able to perform analysis that combines information from both techniques. In this sense, we present here a series of additional steps performed during data processing to obtain comparable data. As follows, this section indicates the reference data used during the computation of wave aberrations, as well as the procedure carried out to compensate for residual errors of the measuring system. Finally, matched DP and HS second-pass responses for pupils of 4mm in diameter are used to validate the system.

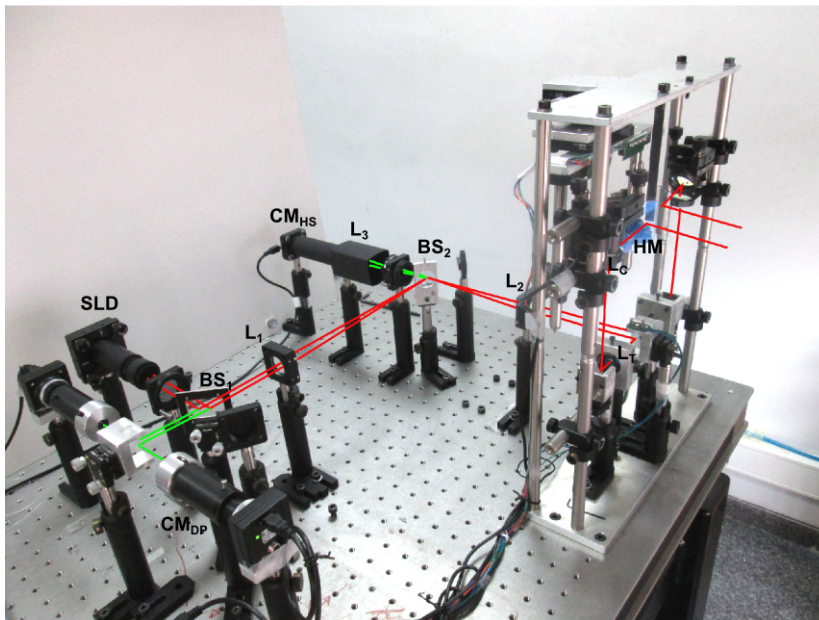


Figure 3.17: The MEOQ system.

### 3.2.1 Selection of HS reference data

There are a series of factors that may induce aberrations in the system. For instance, some optical devices have been tilted to avoid reflections within the second-pass path of light, which induces astigmatism. Moreover, it has been pointed out (see section 3.1.4) that tunable-

<sup>10</sup>See section 3.1.3 for more details on the characterization of both the double-pass and Hartmann-Shack configurations.

devices may be affected by coma-like aberrations. These effects may be more evident with increments in pupil diameters. While aberrations are always present in double-pass measurements, the effects of aberrations may be masked in Hartmann-Shack sensors depending on the data that is used as reference during the computation of wavefront slopes. Therefore, the right selection of reference data is important to reach comparable curves.

In Hartmann-Shack, wave aberrations are estimated by quantifying spot displacements from a user-defined reference. Traditionally, this reference corresponds to centroid positions of an image taken when the output is irradiated with collimated light [22, 108]. In this manner, residual errors caused by the measurement system are avoided, so the computed wave aberrations contain only the effects of the eye under assessment. In order to have HS and DP data with the same information on aberrations, including the one of the measurement instrument, the MEOQ system quantifies spot displacements from theoretical positions, a pattern of equally spaced horizontal and vertical lines whose intersections indicate the positions where the spots would be located in an aberration-free system.

The MEOQ system is able to compute HS data using either centroid or theoretical positions. To generate the reference data, a perfect grid with a spacing of 38 pixels between lines is calculated first. This value considers the lenslet pitch and the pixel size in the HS sensor. Then, the pattern is shifted until finding the best coincidences between intersections and spots centroids of a reference image, which corresponds to the second pass response for collimated light irradiating the system from the pupil plane of the eye. The shifted grid and the spot centroids are considered as the theoretical and experimental reference, respectively. Once saved, they are available for subsequent measurements and the use of one or another is easily selected during data analysis.

In order to visualize the difference between these two ways of getting data, the single-pass response of the system was measured for a defocused beam. To do this, a trial lens with spherical power of 0.25D was placed in front of the collimated beam irradiating the system from the eye's pupil plane. Figure 3.18 shows the PSF measured with the DP sensor along with the ones estimated from HS data by using the centroid and the theoretical positions during the computation of the wavefront slopes. As observed, the best coincidences in terms of shape between the Hartmann-Shack and the double-pass data are found when wave aberrations provoked by the system are included during the PSF estimation (theoretical reference).

It should be mentioned that aberrations or manufacturing errors of devices in non-common optical paths may be a source of differences between images. For instance, the effects of errors

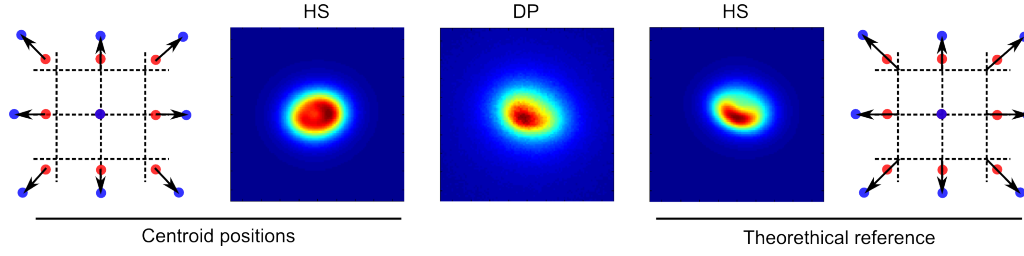


**Figure 3.18:** Second pass response of the MEOQ system for the double-pass (DP) and Hartmann-Shack (HS) sensor. In the latter case, wavefront slopes are computed with respect to centroid positions of a reference image (left) and the intersections of an ideal grid used as theoretical reference (right).

in lenslet positions are not present in double-pass images, but are interpreted as aberrations in the Hartmann-Shack data. However, based on the comparison with the double-pass data, visual inspection of images for the theoretical-reference case does not reveal that this could be a source of significant deviations. Therefore, wavefront slopes are computed hereafter with respect to the intersection of an ideal grid used as theoretical reference.

### 3.2.2 Compensation for residual errors

The second-pass response of the system for pupil diameters of  $4mm$  was measured for both eyes while the output was irradiated with collimated laser light. The DP and HS images used for this analysis correspond to recordings for the best optical quality (narrowest spot in the DP sensor). The MTFs were computed as the radial profile of the Fourier transformed image intensity. In the case of HS data, wave aberrations were obtained with respect to a theoretical reference. There are a number of possible causes producing the differences between curves observed in figure 3.19. For instance, the non-sensed higher order aberrations may be overestimating the response of the HS sensor. Moreover, we believe that light dispersion in the tunable device contributes to residual errors, as observed in the edges the DP image in figure 3.18. Whatever the cause, a method to compensate for residual errors would allow a direct comparison between DP and HS data.

Assuming that it can be expressed in terms of the diffraction limited response  $MTF_{DL}$  and the contribution of residual errors  $MTF_R$  provoked by the system through a multiplicative model, the  $MTF_B$  for the best possible optical quality is expressed as

$$MTF_B = MTF_{DL} \times MTF_R \quad (3.10)$$

Therefore, it would be possible to quantify the contribution of residual errors by deconvolving

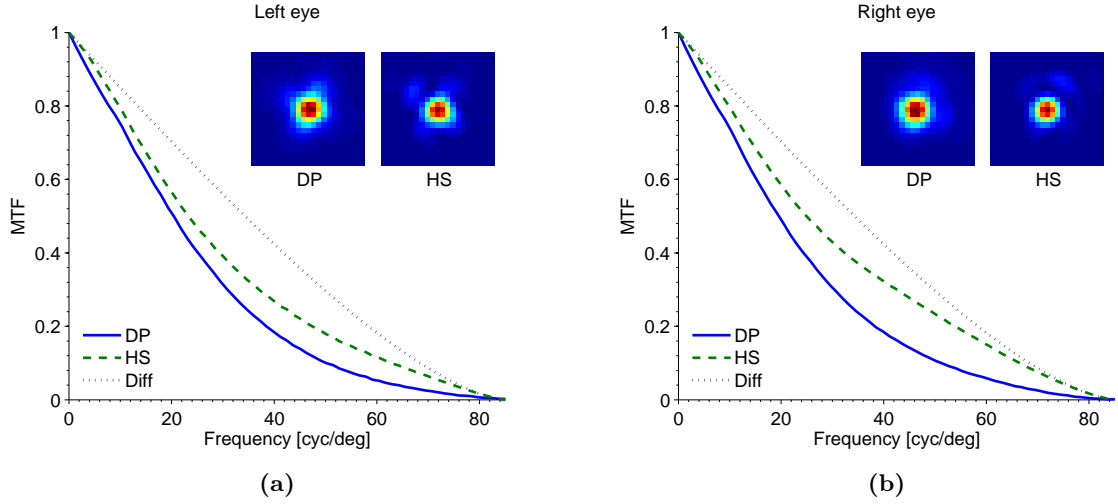


**Figure 3.19:** Second pass response of the MEOQ system for both eyes. The double-pass (solid line), Hartmann-Shack (dashed line) and the diffraction limited response (dotted line) are plotted.  $4 \times 4$  arcmin versions of the second-pass PSF for the DP and HS technique are also included.

the effects of diffraction from  $MTF_B$ . Alternatively, considering a time invariant behavior in deviations provoked by the system, an estimated  $MTF_C$  could be computed from the measured  $MTF$  after compensating for the effects of residual errors by applying the following expression

$$MTF_C = \frac{MTF}{MTF_R} \quad (3.11)$$

This method of compensation for residual errors is applied in the MEOQ system with successful results. To obtain the magnitude of  $MTF_R$ , images for the best optical quality are obtained for both the DP and the HS sensor. In fact, this configuration corresponds to that used during the computations of reference for the computation of wave aberrations. Once obtained, the effects of residual errors are compensated in a 2D fashion for any computed  $MTF$ . Due to its construction, MTFs fully matched with diffracted limited curves are obtained when the compensation is applied over images for the best optical quality. Since deviations from diffraction limited curves present a small magnitude for the first-pass response, the compensation is only applied to the second-pass response.

### 3.2.3 DP and HS response comparison

Before measurements, the MEOQ system should be calibrated. The purpose of this stage is to obtain the reference data that is used during the determination of wave aberrations,

refractions, and curves with information on the subject's optical quality. The calibration process consists in measuring the second-pass response of both the DP and HS image when the system is irradiated at its output with collimated light. In these conditions, the spherical and astigmatic refractive errors are computed from HS data using an ideal grid as reference during the computation of the wavefront slopes. These residual components are compensated in measurements to provide accurate estimations of refraction. After computing the corresponding MTF, the residual error  $MTF_R$  is obtained for both the DP and the HS sensor. This data is saved and used in subsequent measurements to be compensated for. Therefore, the real MTF is estimated from the measured MTF, which contains some amount of deviations provoked by aberrations and diffusion inherent to the measuring instrument. After calibrated, the MEOQ system is able to provide DP and HS data that can be compared with respect to each other.

### Second-pass response

The second-pass response of the MEOQ system is presented here in terms of MTFs. The curves were obtained by irradiating with collimated light the output of the system during image recording. During computations, wave aberrations were computed with respect to an ideal reference (see section 3.2.1) and applying the correction factors explained in last section. The images were recorded for the best optical quality and for two more cases: for an induced astigmatism and defocus of  $-0.25D$  each, respectively. The induced aberrations were generated by placing trial lenses in front of the collimated beam. Since the response present a similar behavior for both eyes, figure 3.20 shows only data for the right eye.

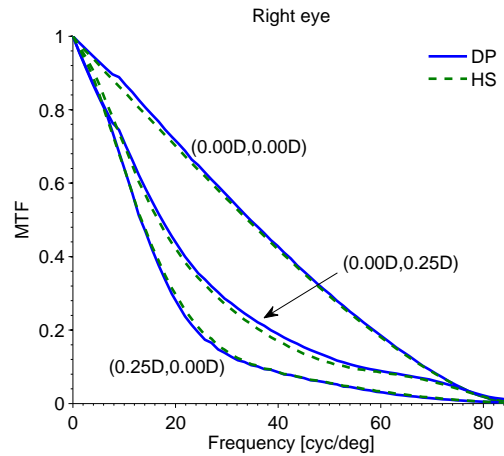


**Figure 3.20:** Second pass response of the MEOQ system for the double-pass (solid line) and Hartmann-Shack (dashed line) sensor for different aberrations. The labels following the form (Sphere,Astigmatism) indicates the values of the induced aberrations.

As observed, the compensation of residual errors permits the system to provide comparable DP and HS curves. In terms of Strehl ratios, a maximum relative deviation of 0.012 and 0.008 is found for the left and right eye for the measured cases. These differences could be decreased, for instance, using a finer sampling resolution in the HS sensor. However, the small deviations are enough for our purposes and we consider that they allow to compare DP with HS data.

### Double-pass response

The double-pass response was measured for an artificial eye consisting of a lens with  $50\text{mm}$  focal length followed by a cardboard acting as retina. This diffusing material was mounted onto a rotating motor that allowed obtaining non-speckled images. The MTF residual error correction was applied for both DP and HS curves. The analyzed data correspond to images for the best optical quality (narrowest spot in the DP sensor). In the case of HS and diffraction limited data, the double-pass response was obtained by multiplying the MTF for pupils of 2 and  $4\text{mm}$ . Both the left-eye and right-eye optical paths of the system presented similar behaviors. For this reason, figure 3.21 shows only the results for the latter optical path.

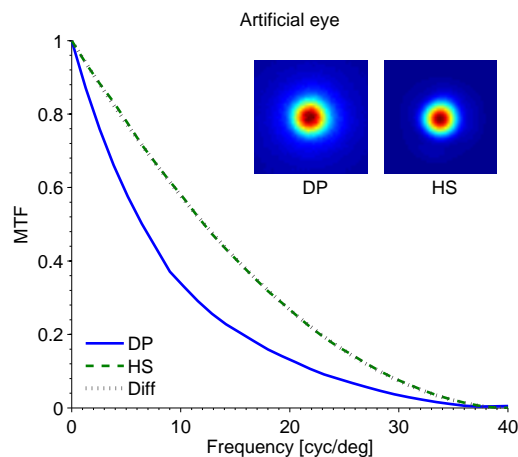


**Figure 3.21:** Double-pass response of the MEOQ system for the DP (solid line) and HS (dashed line) sensors for an artificial eye. The double-pass diffraction limited curve is plotted in the figure (dotted line), although it is almost overlapped by HS data. The DP image and the one reconstructed from HS data are also presented.

The behavior of the system for an artificial eye shows a good agreement between diffraction limited and HS curves. In terms of Strehl ratios, there is a relative deviation of 0.007 and 0.002 for the left and the right eye, respectively. On the contrary, the DP MTF is considerably lower than the expected values. Considering the matched curves for the second-pass response in figure 3.20, the differences between DP and HS are not attributed to the measuring instru-

ment, but to the characteristics of the system under assessment. Based on the similarities between HS diffraction limited data, lower order aberrations in the artificial eye present a small contribution to the response. Assuming that aberrations have a negligible impact, the characteristics of the diffuser used as retina may be the source of the differences. This will be analyzed in the next chapter.

### 3.3 Conclusions

In this chapter, the MEOQ system and its main features have been introduced. The design and implementation of a multimodal system working in a binocular open-field configuration able to correct low order aberrations was presented. The system has been validated by obtaining diffraction limited curves for small pupils and by reaching data that can be compared with respect to each other for the double-pass and the Hartmann-Shack configurations. It has been shown that comparable MTF curves can be obtained if wave aberrations are computed with respect to a theoretical reference and if the data is compensated for residual errors of the measurement instrument. The details of this procedure have been explained and demonstrated through experimental measurements. In the case of the double-pass response, measurements on an artificial eye suggest that retina diffusion may be a considerable source of differences between DP and HS data.

## Chapter 4

# Estimation of the scattering properties of the ocular fundus

Instruments based on retinal reflections are useful tools that permit an objective evaluation of the processes involved in vision during the imaging of external scenes on the retina [23, 28]. Double-pass [20] and the Hartmann-Shack [22] are examples of techniques relying on the projection of a point source on the retina to estimate the optical properties of the eye. Under conventional data analysis both techniques provide information about diffraction and aberrations [29]. Additionally, double-pass data contain the effects of scattering [10, 17, 109], which can be generated in any of the ocular structures interacting with the incident light, including the retina and deeper layers of the ocular fundus where certain wavelengths may penetrate [42, 84, 1].

When light interacts with the ocular fundus, it suffers from absorption, reflections, and scattering [1]. In the case of the retina, light is waveguided within photoreceptors and part of the incident energy is reflected by the pigment epithelium towards the pupil with a given angular distribution [42]. Since the photoreceptors present different lengths, light emerges from the retina with a variety of phases [100]. The part of the incident light that is not reflected or absorbed by the pigment epithelium may penetrate until the choroid, where the scattering produced by the presence of blood disperses light laterally [1]. It has been suggested that light emitted towards the pupil from this deeper layer is the result of forward scattering and reflections at interfaces such as vessels or sclera [1]. This situation is more evident at certain wavelengths [3, 110] in function of the absorption properties of the pigment epithelium [111]. Thus, red light produces higher amounts of scattering than green light because such

---

wavelengths penetrate not only the retina, but also deeper layers of the ocular fundus with dispersive properties.

The optical properties of the retina have been widely studied. For instance, the effects of orientation and waveguide properties of photoreceptors has been experimentally determined by measuring the light distribution of a point source reflected by the retina using reflectometric techniques [46, 112] and Hartmann-Shack sensors [95]. Moreover, different authors have described the behavior of the angular dependence of light using theoretical models [100, 113], whose predictions agree with psychophysical estimations of the Stiles-Crawford effect. On the other hand, the spatial distribution of photoreceptors has been determined by analyzing images obtained with fundus cameras [114], using modified versions of the reflectometric technique [46], and employing speckle interferometry [115].

The scattering process occurring in the ocular fundus has been considered in visual optics to explain differences between double-pass data and that obtained with instruments that are not affected by scattering, such as interferometric devices [84] and Hartmann-Shack sensors [17]. These works suggest that the differences may arise from light scattered in the choroid. On the other hand, it has been corroborated that variations in both the structure of the ocular fundus [42] and the wavelength [116] influence the response of double-pass instruments. Some authors have developed theoretical models based on approximations of experimental data that predict the response of the ocular fundus to incident light at different wavelengths [1]. However, this knowledge is usually not incorporated into double-pass models, maybe because the difficulties to separate its contribution in the double-pass response in real measurements or because it is not clear if the scattered light in the visible range contributes to the image formation process while it travels through the photoreceptors towards the pupil [84].

The objective of this chapter is to introduce a model that accounts for the effects of fundal scattering in the model describing the double-pass process presented by Artal *et al.* in [13]. To do this, we follow two different approaches for modeling the scattering: the equivalent diffuser and the lateral spreading of light. In the former case, the ocular fundus is statistically described using the Beckmann-Kirchhoff scattering theory [90] to obtain the values of roughness and correlation length of an equivalent surface that would produce the same effects as those observed in double-pass measurements. In the second approach, the modulation transfer function of the scattering process is estimated and used to obtain the lateral spreading of light produced by the ocular fundus [1] during the double-pass process. Experimentally, the models are used in measurements of young healthy eyes obtained with the MEOQ system,

which works in the infrared part of the spectrum and provides comparable double-pass and Hartmann-Shack curves. The differences between techniques are attributed to fundal scattering and fitted using the proposed models to provide parameters with information on the process occurring in the ocular fundus.

We consider the incorporation of models for scattering in the double-pass formulae important because it can be used to obtain a better understanding of the processes occurring in the ocular fundus. In turn, this knowledge can be used to improve the accuracy of the parameters with information about the optical quality of the eye, such as the modulation transfer function, Strehl ratio, scatter indexes, among others. The characterization of the scattering process may be used to relate deviations from normal values to other problems affecting vision.

This chapter is organized in the following manner. First, the effects of the fundus in the double-pass process are presented and described in section 4.1 using measurements on an artificial eye for different diffusing materials acting as retinas. Section 4.2 presents the models for the equivalent diffuser and the lateral spreading of light. The validation of the models and their performance are presented in that section also. The experimental results are included in section 4.3. The procedure followed during the experimentation and data processing is explained at the beginning of the section. Finally, the conclusions on the models and their application in real measurements are presented at the end of the chapter.

## **4.1 Effects of retinal scattering on DP and HS measurements**

When double-pass and Hartmann-Shack instruments are used to assess the same optical system, the estimations may differ with respect to each other because they contain complementary information on the phenomena occurring in the eye [29]. In particular, the directional sensitivity of photoreceptors [112] and ocular scattering [14] are known to contribute to those differences [17, 29, 84]. In addition to the scattering produced by the lens of the eye, scattering may arise during the complex reflection process occurring in the retina [117] or in deeper layers in the ocular fundus [84]. For the retina, the performance of the scattering depends on the characteristics of the surface [90, 118], such as cone spacing (in the case of the fovea) and the phase fluctuations arising from the differences in length between photoreceptors [100]. On the other hand, the scattering in the choroid produces a lateral spreading of light in function of both the wavelength and the distance traveled by light inside the dispersive material [1].

In the double-pass process, the scattering produces a veil surrounding the point-spread func-

tion (PSF) of the eye [1]. Related to the PSF through a Fourier transformation [16], the modulation transfer function (MTF) becomes narrower under the presence of scattering, which is measured as a decrease of the volume under the normalized curve. In terms of the Strehl ratio, this situation represents a decrement in the optical quality of the assessed eye [42]. The magnitude of the scattering is wavelength-dependent [1]. In this manner systems working with infrared light are able to detect higher fundal scattering because longer wavelengths penetrate deeper into the layers [110] before being directed towards the pupil.

In Hartmann-Shack sensors, the wavefront is sampled at the pupil plane using a lenslet array, which forms at its focal plane a set of spots that are used to reconstruct wave aberrations [22]. Indeed, each spot represents a local point-spread function of the eye at a given pupil position [57]. Not only the scattering, but also the directional properties of the retina affect the intensity at the pupil plane of the eye [100]. For this reason the spots may vary in intensity in function of its position with respect to the pupil [57, 95]. Although a set of veiled point-spread functions with different integrated intensities is used during computations, there is experimental evidence indicating that the spot position is not modified under the presence of scattering [29, 58]. Therefore, conventional Hartmann-Shack data processing is not a useful method to quantify this phenomenon.

#### 4.1.1 Experimental evidence of retinal scattering

The effects of scattering in the retinal plane of an artificial eye have been measured experimentally using the MEOQ system, which integrates a double-pass (DP) instrument with a Hartmann-Shack (HS) sensor. The characteristics of the multimodal system, the methodology to obtain comparable data between techniques, and its validation have been presented in chapter 3 of this work<sup>1</sup>. Regarding the artificial eye, this device consists of a lens with 50mm focal length and its response was measured for two cardboards acting as retinas. The interchangeable diffuse materials  $R_1$  and  $R_2$  were mounted in a rotating motor to break temporal coherence [60] by producing uncorrelated patterns during image recording. In this manner, the saved frames were not much affected by speckle. Using an integration time of 40ms, 5 images were recorded for both the double-pass and the Hartmann-Shack sensor. Then, the

---

<sup>1</sup>The DP and HS techniques provide comparable data with respect to each other after computing wavefront slopes from intersections of an ideal grid and compensating for residual errors provoked by optical defects of the measuring system. Although not mentioned, this methodology is followed to obtain the results presented along this chapter.

average image was used to compute the modulation transfer function (MTF) using both techniques. The MTF was obtained as the product of the autocorrelated complex pupil functions [16] for the first and second pass pupil diameters ( $MTF_{2\text{mm}} \times MTF_{4\text{mm}}$ ) in the case of HS and by Fourier transforming the recorded image and applying a peak correction [43] when working with DP data.

Figure 4.1a depicts the DP and HS MTF for both cases. As observed, the Hartmann-Shack curves are practically overlapped for both of the diffusers acting as retinas. On the contrary, double-pass data present a variability, which may be provoked by differences in the properties between  $R_1$  and  $R_2$ . The ratios between curves presented in figure 4.1b suggest that the effects of the scattering process follow an exponential behavior and that the resulting curve is valid when the MTFs have representative magnitudes; the ratio tend to infinity when the HS MTF approaches to zero. The cardboards were visually different in the sense that  $R_2$  seemed to be coated, probably with some kind of ink. Assuming that the differences in the material produced unequal scattering, the observed performance would be in agreement with the results presented in [22] and [84] suggesting that DP data is affected by fundal scattering.

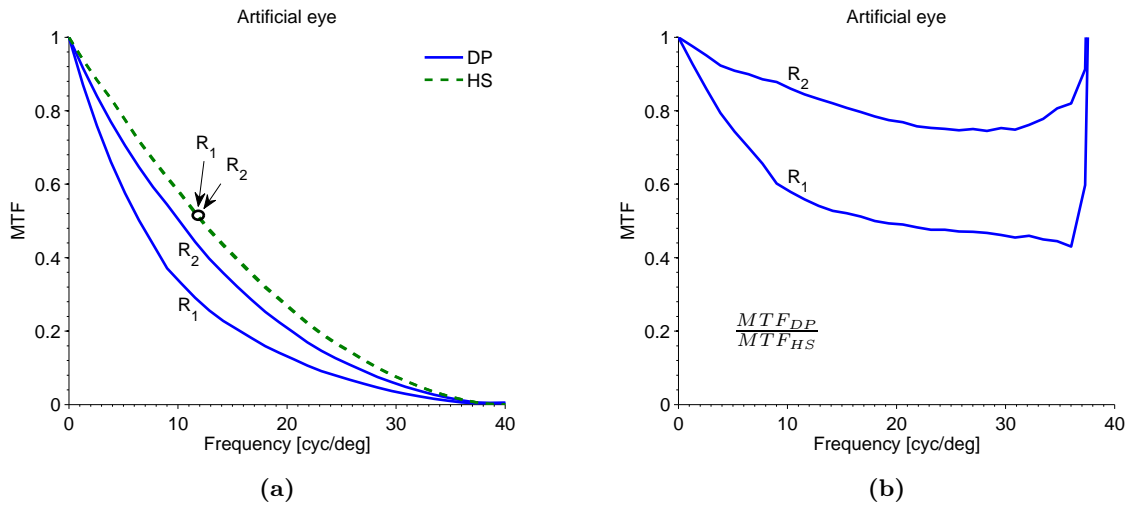


**Figure 4.1:** (a): DP (solid line) and HS (dashed line) response for an artificial eye using retinas  $R_1$  and  $R_2$ . The HS data for both retinas appears in the figure, but they are overlapped. (b): Ratio of the double-pass to the Hartmann-Shack MTF for both pupils.

The properties of the cardboards were measured with the 3D profiles PLu apex (Sensofar) [119]. Figure 4.2 presents the horizontal cuts at the center of the measured area. It was not possible to find a representative spacing between elements within the material because the cardboards are probably composed by fibers that generate random values for this parameter. On the other hand, the standard deviation of the height fluctuations of retinas  $R_1$  and  $R_2$

were  $3.984$  and  $0.900\mu\text{m}$ , respectively. Based on these differences, the higher magnitude of the deviations for retina  $R_1$  with respect to those for  $R_2$  in figure 4.1a may be related to the larger height fluctuations of that diffusing material.

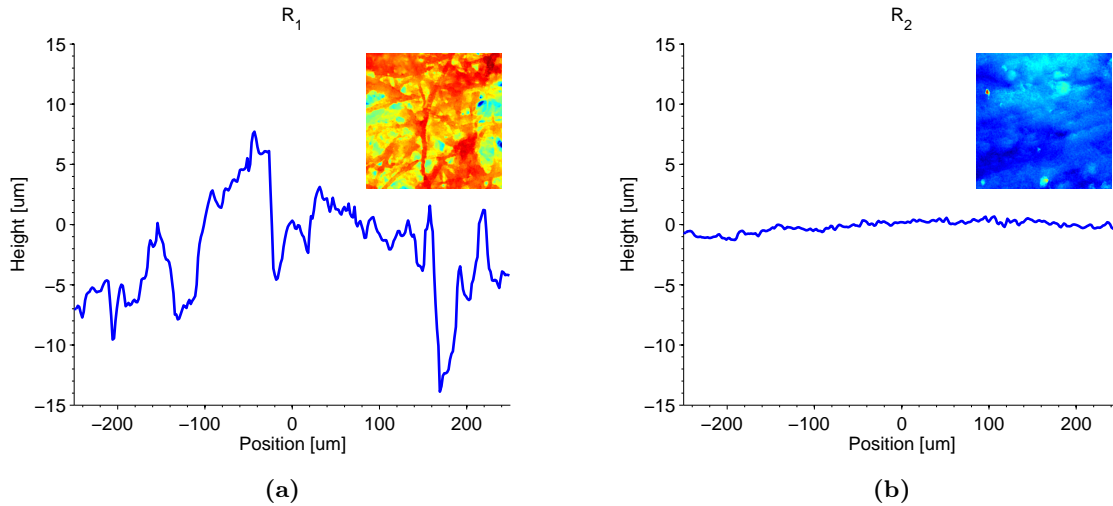


**Figure 4.2:** Horizontal cut of the 3D profile for retinas  $R_1$  (a) and  $R_2$  (b).

The results presented in this section indicate on the one hand that double-pass systems detect retinal scattering and on the other hand that multimodal systems based on DP and HS measurements can be used to quantify this phenomenon. This quantification can be based on differences between curves as done by other authors [29, 85] during the quantification of intraocular scattering. Since these variations are related to the properties of the reflecting material, a model accounting for the effects of scattering may be used to estimate the properties of the fundus.

## 4.2 Incorporation of retinal scattering in the DP expression

The double-pass technique is a useful tool to describe the optical properties of the eye under various conditions [27, 45, 120]. In this, first a point source is projected on the retina; there the light suffers a time-varying complex reflection process and then the aerial retinal image is recorded after the second-pass of light through the optics of the eye [20]. A theoretical description of this process is presented in [13]. During the development of the expressions, the reflection process that occurs in the fundus is assumed to be  $\delta$ -correlated [117]. Under this consideration, the dependence of the fundus is eliminated for the long-exposure (incoherent) intensity. However, experimental measurements based on reflectometric techniques [46] and models of the fundal response to incident light [1] suggest that the scattering process arising

from the iteration of light with the fundus is governed by correlation functions different than  $\delta$ .

The scattering process have been studied in visual optics using the Beckmann-Kirchhoff formulation [90], which is a method that permits the prediction of the energy distribution at the far-field of the surface. For this, the effects imposed by the surface are statistically described in terms of height fluctuations and correlation functions. This formulation have been used to describe the properties of eye lens surfaces by measuring the diffuse component of Purkinje images [91] and to account for the effects of intraocular scattering under the concept of equivalent diffuser [86, 121] using exponential correlation functions. In the ocular fundus, Marcos *et al.* in [100] presented a model for the diffuse component of the scattering field produced by retinal reflections (without considering the effects of the choroid). Such formulation is based on the Kirchhoff approximation and uses correlation functions following a Gaussian behavior.

Hodgkinson *et al.* in [1] introduced a model that describes the response of the ocular fundus to incident light. Basically, the results in [1] predict the point spread function of the ocular fundus at different wavelengths. In systems without scattering this response is given by a  $\delta$ -function, but the application of the model indicates that the point spread function may be fitted using *sech* functions<sup>2</sup> and that the standard deviation of the response (the lateral spreading of light) is proportional to the thickness of the layers containing blood cells, which in the case of the eye refers to the choroid.

The objective of this section is to obtain two models that account for the effects of the scattering process occurring either in the retina or in deeper layers of the ocular fundus. In this context, it is necessary to modify the shape of the correlation function in the double-pass expression developed in [13] to account for the effects of scattering from the ocular fundus in DP images. On the one hand, the statistically description used by Beckmann is introduced into the double-pass expression considering an exponential correlation function. On the other hand, the scattering process is treated in terms of its point spread function using Gaussian-like functions. The theoretical development of both approaches is presented in detail until an expression for the modulation transfer function is obtained that takes the effects of scattering into account.

---

<sup>2</sup>sech refers to a hyperbolic secant function and is defined as  $\text{sech} = 2/(e^x + e^{-x})$  [122]

### 4.2.1 The double-pass expression

Consider the image-formation process in the double-pass technique described by Artal *et al.* in [13]. From there, it is known that the instantaneous (coherent) intensity of the double-pass process computed as the square modulus of the amplitude field  $U_i''$  at the second pass image plane  $(x'', y'')$  can be expressed as

$$\begin{aligned} I_i''(x'', y'') &= |U_i''(x'', y'')|^2 \\ &= m^4 |h_2(mx'', my'') \otimes [h_1(-mx'', -my'') R_i(-mx'', -my'')]|^2 \end{aligned} \quad (4.1)$$

where  $m$  is the modulus of the first pass magnification,  $h_1$  and  $h_2$  are the first and second pass amplitude-spread functions, and  $\otimes$  denotes convolution. As originally conceived,  $R_i$  accounts for the instantaneous reflection factor of the retina. However, there are cases in which deeper layers of the ocular fundus should be considered to obtain a more realistic representation of the double-pass process, especially under the presence of scattering. Therefore, the term  $R_i$  as used here incorporates all the effects arising in any of the layers of the ocular fundus.

Let us consider hereafter the unidimensional case for the sake of clarity. The incoherent double-pass response is obtained by averaging a number of coherent estimations denoted by equation 4.1 [13]. The image resulting from this operation is known to be linear in intensity [16]. In this manner, the square magnitudes affecting the intensity can be applied independently on each side of the convolution and the results can be expressed in terms of point-spread functions (PSF). Assuming that the spread functions are deterministic and denoting the ensemble average as  $\langle \dots \rangle$ , the intensity can be written in the following form

$$\begin{aligned} \langle I_i''(x'') \rangle &= I''(x'') \\ &\propto |h_2(mx'')|^2 \otimes \left[ |h_1(-mx'')|^2 \langle R_i(-mx'') R_i^*(-mx'') \rangle \right] \\ &= PSF_2(mx'') \otimes [PSF_1(-mx'') \langle R_i(-mx'') R_i^*(-mx'') \rangle] \end{aligned} \quad (4.2)$$

The term  $\langle RR_1^* \rangle$  represents the realization of the ensemble average between the scattered fields at two point positions [90] and is computed as an autocorrelation function. Moreover, the ensemble average is substituted by a space average because the process is considered as statistically stationary [118]. The result of this operation is a function that depends on the properties of the rough surface (fundus).

### 4.2.2 Modeling scattering as equivalent diffuser

Let us consider the fundus as a randomly varying function  $\zeta(-mx'', -my'')$  assuming random heights  $z$  at each point along its area with a given spatial distribution and correlation function. Based on the results reported by Beckmann in [90] and assuming that the reflection process does not modify the intensity of the incoming light, the phase changes produced by the fundus can be described as  $R = \exp(j\nu_z\zeta)$ , where  $\nu_z \approx 2k$ , with  $k = 2\pi/\lambda$  and for incident and reflected light with directions around the normal of the reflecting surface, as in the case of the eye when assessed with the double-pass technique<sup>3</sup>. Therefore, we can express the factor  $\langle RR_1^* \rangle$  in the description of the coherent double-pass process given by equation 4.2 in terms of both the standard deviations of the fluctuations (roughness)  $\sigma_z$  and the correlation coefficient  $C(\rho)$

$$\begin{aligned} \langle RR_1^* \rangle &= \langle e^{j\nu_z(\zeta - \zeta_1)} \rangle \\ &= \exp \{ -k^2 \sigma^2 [1 - C(\rho)] \} \end{aligned} \quad (4.3)$$

where  $\rho = mx_1'' - mx''$  is the distance between two points within the scattering plane and  $\sigma = 2\sigma_z$  accounts for the phase fluctuation during the scattering process. We have to define the correlation coefficient observed in equation 4.3 to evaluate the effects of the reflection process. Different studies have shown that correlation coefficients with exponential forms fit better the scattering processes occurring in the eye [86, 121]. Assuming an exponential behavior, the correlation coefficient can be expressed as  $C(\rho) = \exp(-|\rho|/r_0)$  [90], where  $r_0$  is the correlation length, which in other words represents the distance between valleys and hills in the rough surface [100]. If expanded using a Taylor series, equation 4.3 takes the following form

$$\langle RR_1^* \rangle = \exp(-k^2 \sigma^2) \left[ 1 + \sum_{n=1}^{\infty} \frac{k^{2n} \sigma^{2n} C^n(\rho)}{n!} \right] \quad (4.4)$$

After substituting last result in equation 4.2, the intensity can be separated into terms  $\gamma_s^2$  and  $\gamma_d^2$ , which account respectively for the specular and diffuse component of the scattering process.

---

<sup>3</sup>The expression given by Beckmann depends on the angle between the normal of the surface and the incident ( $\theta_1$ ) and reflected ( $\theta_2$ ) light and is expressed as  $\nu_z = k(\cos\theta_1 + \cos\theta_2)$ . In the double-pass process and for a pupil diameter of 4mm, the angles remain lower than 7°. Thus, the cosines take always values fluctuating around 1.

$$I''(x'') = \exp(-k^2\sigma^2) [\gamma_s^2(x'') + \gamma_d^2(x'')] \quad (4.5)$$

$$\gamma_s^2(x'') = PSF_2(mx'') \otimes PSF_1(-mx'') \quad (4.6)$$

$$\gamma_d^2(x'', \rho) = PSF_2(mx'') \otimes \left[ PSF_1(-mx'') \sum_{n=1}^{\infty} \frac{k^{2n}\sigma^{2n}}{n!} \exp\left(-\frac{|\rho|}{r_0/n}\right) \right] \quad (4.7)$$

Equation 4.6 indicates that the specular component is the response that would be obtained for a scattering-free system and is expressed by the convolution of the first and second pass point-spread functions. On the other hand, the properties of the fundus influence the result of the diffuse component. Equation 4.7 expresses this situation. However, it depends not only on the coordinates, but also on the distance  $\rho = mx_1'' - mx''$ . To eliminate such dependence we have to add for each coordinate ( $mx_1''$ ) the contribution of all the other scatters, whose impact is a function of both the amplitude of the field at ( $mx_1''$ ) and the distance  $\rho$ . By integrating over  $mx_1''$  the part of the expression affected by  $\rho$ , the diffuse component takes the form of a convolution integral

$$\begin{aligned} \gamma_d^2(x'') &= PSF_2(mx'') \\ &\otimes \int PSF_1(-mx_1'') \sum_{n=1}^{\infty} \frac{k^{2n}\sigma^{2n}}{n!} \exp\left(-\frac{|-mx'' + mx_1''|}{r_0/n}\right) dx_1'' \\ &= PSF_2(mx'') \otimes PSF_1(-mx_1'') \otimes \sum_{n=1}^{\infty} \frac{k^{2n}\sigma^{2n}}{n!} \exp\left(-\frac{|-mx''|}{r_0/n}\right) \end{aligned} \quad (4.8)$$

It results convenient to evaluate the scattering process in the Fourier domain. There, the convolutions are evaluated as a multiplication between spectral representations [122]. When applied over the PSF, the Fourier transform leads to the optical transfer function (OTF) [16], which in the case of the eye indicates the complex distribution of energy over the pupil plane. Using the results given by equations 4.6 and 4.8, the Fourier transformation of equation 4.5 gives the following

$$\mathcal{F}\{I''(x'')\} = \exp(-k^2\sigma^2) OTF_2(u) OTF_1^*(u) [1 + \Gamma(u)] \quad (4.9)$$

$$\Gamma(u) = \frac{2}{mL_{x''}} \sum_{n=1}^{\infty} \frac{1}{n!} \frac{k^{2n} \sigma^{2n} r_0/n}{1 + 4\pi^2 r_0^2 u^2 / (m^2 n^2)} \quad (4.10)$$

There,  $u$  is the unidimensional angular coordinate in cyc/m at the pupil plane and  $mL_{x''}$  is the length of the assessed region. Last equation indicates that the modulus of the Fourier representation is affected by the scattering process and that these are influenced by the magnitude of the fluctuations ( $\sigma$ , roughness) and the spatial distribution of the scatters ( $r_0$ , grain size). On the other hand, the modulation transfer function (MTF) defined as the modulus of the OTF is a parameter usually used to derive information on the optical quality [13]. By definition, the MTF is normalized with respect to its value at the zero frequency [16]. After proper normalization the two-dimensional modulation transfer function of the double-pass process may be obtained as

$$MTF(u, v) = MTF_2(u, v) MTF_1(u, v) \frac{1 + \Gamma(u, v)}{1 + \Gamma(0, 0)} \quad (4.11)$$

$$\Gamma(u, v) = \frac{2}{mL_{x''} L_{y''}} \sum_{n=1}^{\infty} \frac{1}{n!} \frac{k^{2n} \sigma^{2n} r_0/n}{1 + 4\pi^2 r_0^2 (u^2 + v^2) / (m^2 n^2)} \quad (4.12)$$

Equations 4.11 and 4.12 stand for the effects of the scattering process in the MTF. Since this is based on multiplications instead of convolutions, it can easily be incorporated into computations. In this manner, they may be used to estimate the response of systems not affected by diffusion, such as curves obtained with Hartmann-Shack methods or in schematic eyes. However, before this, the dependence of light penetration with wavelength should be incorporated.

### Validation of the model

The expressions for the modulation transfer function obtained in last section indicate that the diffuse component is proportional to both the standard deviation of height fluctuations ( $\sigma$ ) and correlation length ( $r_0$ ), as predicted from Beckmann formulation in [90] for scattering in the far-field of the surface. In fact, the expression in equation 4.11 is comparable with that obtained by Navarro in [91] for the effects of intraocular scattering, because in the case of scattering occurring in the eye lenses the far-field is derived at the retina plane.

The expression for the diffuse component predicted by Beckmann formulation for exponential correlation functions for incident and reflected light with angles around the normal of the surface is given by

$$\Gamma_B(u, v) = \frac{2\pi}{mL_{x''}L_{y''}} \sum_{n=1}^{\infty} \frac{1}{n!} \frac{k^{2n}\sigma^{2n}r_0^2/n^2}{[1 + 4\pi^2r_0^2(u^2 + v^2)/(m^2n^2)]^{3/2}} \quad (4.13)$$

Although there is similarity of equation 4.13 with the expression obtained here, they are not completely equal. During the development of the model presented in this work, the effects of the retina are first expanded using a Taylor series and then the far field is obtained by evaluating the effects in the Fraunhofer region through a Fourier transformation [16]. In the Beckmann formulation the effects of scattering are evaluated by approximating an integral based on Bessel functions [90]. Since these methods are based on different approximations, the expressions may not be completely equal, but they must give similar results.

The validation of equation 4.11 and 4.12 was performed by comparing the normalized uni-dimensional behavior of the diffuse component,  $\bar{\Gamma} = \Gamma(u)/\Gamma(0)$ , with the model for retinal scattering developed by Marcos' *et al.* in [100] and with the expression given by equation 4.13 after proper normalization,  $\bar{\Gamma}_B = \Gamma_B(u)/\Gamma_B(0)$ . For Marcos model, the diffuse component of the intensity is obtained as  $\bar{\Gamma}_M = 10^{-2\varrho u^2}$ , where  $\varrho$  is a shape factor computed with equation 4.14. This expression differs with respect to the one given in [100] because it was originally obtained for coordinates in mm and here they are given in cyc/mm and expressed in terms of correlation lengths.

$$\varrho = \frac{\pi^2 r_0^2}{\ln(10)} \quad (4.14)$$

Figure 4.3 depicts the behavior of the three models for  $\sigma = 0.1\mu\text{m}$  and different correlation lengths  $r_0$ . The values for the lengths used during simulations correspond to those typically considered for photoreceptors in the fovea [46]. As observed, all  $\bar{\Gamma}$ ,  $\bar{\Gamma}_B$  and  $\bar{\Gamma}_M$  predict a widening of the diffuse component with decrements of  $r_0$ . This performance is expected because the retinal and the pupil planes are related through Fourier transformations [13]; thus, cones with smaller separations affects higher angular frequencies [16]. Furthermore, the values predicted by the model presented in this work are in between those obtained by  $\bar{\Gamma}_B$  and  $\bar{\Gamma}_M$  for lower spectral components.

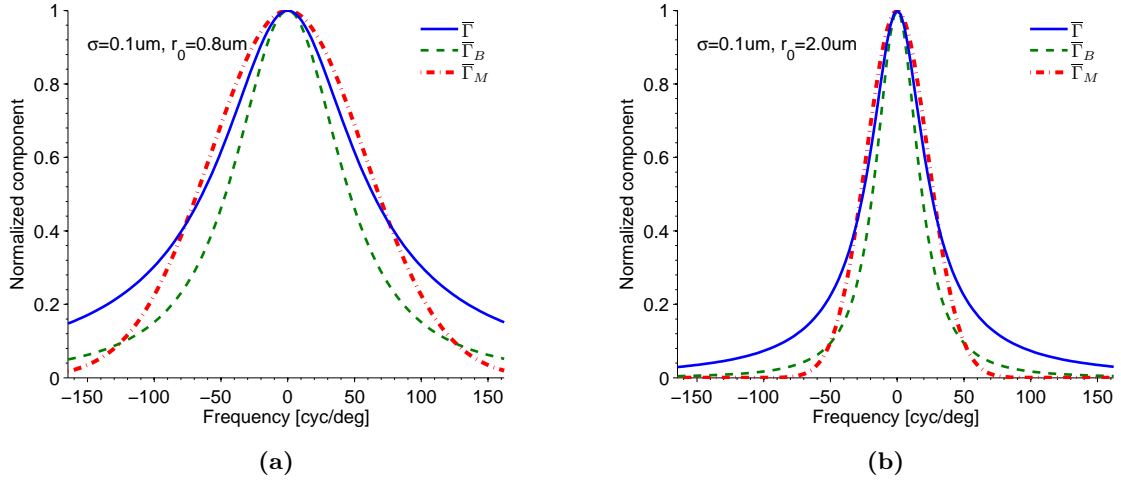


**Figure 4.3:** Comparison of three models for the diffuse component of the scattered field.  $\bar{\Gamma}$  denotes data for the model proposed in this work, while  $\bar{\Gamma}_B$  and  $\bar{\Gamma}_M$  refer to curves using Beckmann's formulation and Marcos' model for retinal reflection, respectively.

The curves depicted in figure 4.3 were obtained by considering only one term of the sum of the Taylor expansion used in equation 4.12. However, the results are still accurate because the plotted cases corresponds to height fluctuations of  $\sigma = 0.1$ . Under this condition, the impact of other terms in the sum is negligible. It is known that the specular component dominates the scattering process for smooth surfaces ( $k^2\sigma^2 \ll 1$ ). As roughness increases, the influence of the diffuse component becomes higher, until reaching a point where this may dominate the scattering process. Considering 10 terms of the Taylor expansion, we suggest that both the diffuse and specular components should be considered for height fluctuations between  $\sigma = 0.07$  and  $0.35\mu\text{m}$  for values of  $r_0$  around  $0.8\mu\text{m}$ . These limits were estimated by finding the positions at which the maximum magnitude of the diffuse components is 1 and 10 times that of the specular component, respectively.

The comparison among models suggest that the model given by equation 4.11 may be used to predict the diffuse component of scattering processes occurring in the ocular fundus, such as those arising from the random phase variations imposed by photoreceptors in the retina. Based on the Beckmann model for composite rough surfaces [90], we expect larger values for  $\sigma$  and  $r_0$  during the application of the model under the concept of equivalent diffuser in real measurements affected by scattering from multiple fundal layers.

### 4.2.3 Modeling scattering as lateral spreading of light

In the incoherent double-pass process given by equation 4.2, the light resulting from the interaction of light with the ocular fundus is expressed as a multiplication between the first pass point-spread function and the long-exposure reflection factor of the surface. Let us introduce in the model the concept of point spread function of the ocular fundus. This is denoted as  $PSF_R$  and represents the response of the fundus when this is impinged by a ray of light. Mathematically, the contribution of all the rays forming the incident light is given by the convolution [16]. If the multiplicative reflection process is substituted by a convolution between the incident light and  $PSF_R$ , the double-pass process may be expressed as

$$I''(x'') = PSF_2(mx'') \otimes [PSF_1(-mx'') \otimes PSF_R(-mx'')] \quad (4.15)$$

It results convenient to express the last expression in the Fourier domain, where the convolutions can be evaluated as multiplications between the spectral representations of the functions involved in the process [122]. The magnitude of the Fourier transformed PSF leads to the MTF after proper normalization [16]. In this manner, the spectral representation of the double-pass image can be mathematically represented in terms of modulation transfer functions accounting for the responses of not only the first and second pass, but also the fundus

$$\begin{aligned} MTF(u) &\propto |\mathcal{F}\{I''(x'')\}| \\ &= MTF_2(u) [MTF_1(u) MTF_R(u)] \end{aligned} \quad (4.16)$$

$MTF_R$  should be specified to continue with the development of the model. Hodgkinson in [1] found that the PSF of an idealized ocular fundus may be fitted using *sech* functions. However, there is evidence indicating that some scattering processes occurring in the eye follow an exponential behavior [86, 91]. The measurements presented in section 4.1 on an artificial eye corroborate this behavior for the part of the modulation transfer function attributed to scattering from the fundus <sup>4</sup>. Based on this information, we propose to use an exponential

---

<sup>4</sup>Referring to figure 4.1b, the ratio between the double-pass and Hartmann shack MTF is attributed to scattering from the ocular fundus. Under the multiplicative model proposed in this section, the curve resulting from the ratio could be considered as the MTF of the scattering process.

function to depict this response in the Fourier domain. In particular, we use a function of the form

$$MTF_R(u) = \exp\left(-2\pi\frac{|u|}{r_u}\right) \quad (4.17)$$

where  $r_u$  may be interpreted as the correlation length of the scattering process in the frequency domain. To keep the same format in the model for the equivalent diffuser, we introduce the equality  $r_u = 1/(r_0)$  to have an expression depending on correlation lengths given in object space coordinates. Introducing equation 4.17 in the expression for the modulation transfer function of equation 4.16, we obtain the following

$$MTF(u) = MTF_2(u) MTF_1(u) \exp(-2\pi r_0 |u|) \quad (4.18)$$

The last expression may be used to account for the effects of scattering in the double-pass process. The term  $r_0$  that we call correlation length can be interpreted as an indirect estimation of the lateral spreading of light after the complex reflection process in the fundus. Following the work of Hodgkinson *et al.* in [1], the process in the choroid is dominated by forward scattering and the light returning towards the pupil comes from reflections in the boundaries of this layer. If it is true, variations of this parameter for a fixed wavelength may be related with the thickness of the choroid.

The expression given in equation 4.18 can be used to predict the performance of double-pass systems in the wavelength range going from 600 to 800nm. From [1], we expect a linear increment for  $r_0$  within this range<sup>5</sup>. Hence, the correlation length (lateral spreading) can be computed as

$$r(\lambda) = r|_{800} [1 - s(800 - \lambda)] \quad (4.19)$$

where  $r|_{800} = r_0$  represents the correlation length evaluated at 800nm,  $s$  is a scale factor, and  $\lambda$  indicates the wavelength to be evaluated in nm. Suppose an increment for  $r_0$  of 2.25

---

<sup>5</sup>We expect a similar performance between  $r_0$  used here and the standard deviation of the PSF used in [1]. The authors in that work predict a linear behavior for the standard deviation between 600 and 750nm. Thus, we are assuming that this trend is kept until 800nm.

times between 600 and 800nm, the scalar factor takes a value of  $s = 0.0028$ . It would be necessary to characterize of the scattering at different wavelengths using the model to provide better estimates for  $s$ .

### Validation of the model

The model for the lateral spreading of light given by equations 4.18 and 4.19 can be used to estimate the modulation transfer function of the scattering process in the ocular fundus. Since they both are derived under the concept of point spread function, the results obtained here should coincide with those predicted by Hodgkinson in [1]. In the object plane (ocular fundus), the expression for the response of the surface to incident light is given by

$$PSF_R(mx'') \propto \frac{1}{r_0^2 + (mx'')^2} \quad (4.20)$$

Last mathematical expression corresponds to the Fourier transform pair of equation 4.18 [122] and is not completely equal to the one proposed in [1] because we use here an exponential function to approximate the MTF of the scattering.

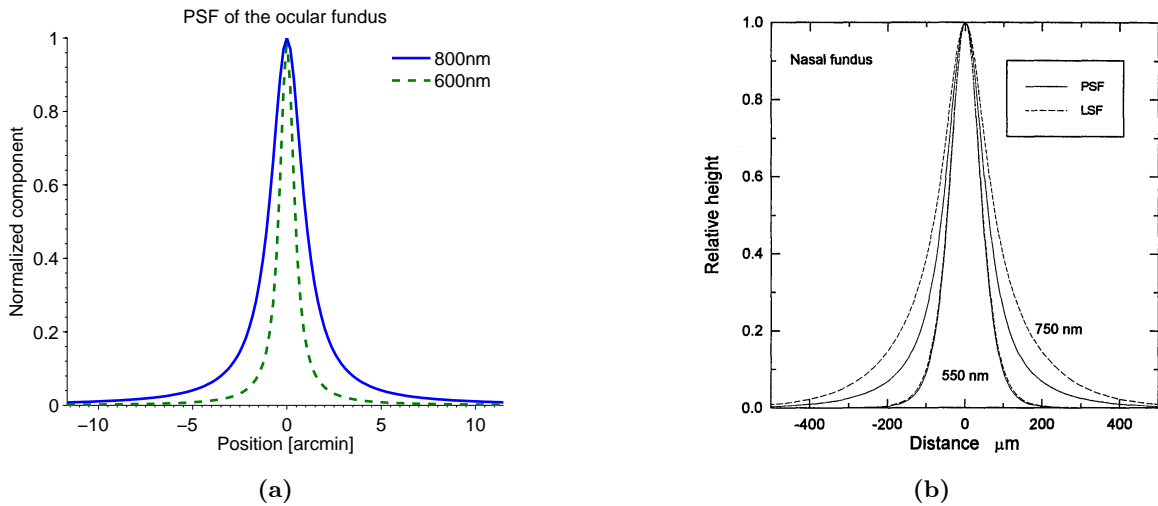


**Figure 4.4:** PSF of the ocular fundus obtained for different wavelengths. (a): Model for lateral spreading proposed in this work for  $r_0 = 5\mu\text{m}$ . (b): Model used by Hodgkinson (image taken from [1]).

Figure 4.4 shows the point spread function of the ocular fundus for different wavelengths using the model given by equations 4.19 and 4.20 and the one proposed in [1]. It is difficult to make a direct comparison between models because of the different approximations, the differences between the parameters used by each model, among other factors. However, it is

important to point out that both cases predict a widening in the PSF for longer wavelengths. This is an expected behavior in real situations based on the penetration properties of the fundus for different spectral components [3]. The scale factor  $s$  used in equation 4.19 was estimated based on results presented in [1]. As stated before, this factor may be modified for a better match to real situations after performing a proper characterization of the model with experimental measurements. Therefore, we believe that this model can be used to predict the scattering process occurring in the ocular fundus of the eye.

#### 4.2.4 Performance of the scattering models

Until now, the behavior of the models has been presented, but only for validation purposes without evaluating its impact in the double-pass modulation transfer function. In this sense, the objective of this section is to introduce into ideal MTF curves the effects of the scattering process predicted by the model for both the equivalent diffuser (model I) and the lateral spreading of light (model II). To do this, the curves for model I and II were computed using equations 4.11 and 4.20, respectively. To estimate the terms  $MTF_1$  and  $MTF_2$  appearing in the expressions, the theoretical predictions [16] for diffraction limited responses for pupils of 2mm and 4mm in diameter were considered. These values correspond to the first and second pass pupils in the MEOQ system.

Figure 4.5a depicts the expected modulation transfer functions for diffraction limited systems affected by scattering using Model I ( $MTF_I$ ) and II ( $MTF_{II}$ ). The diffracted limited response of the double-pass process was computed as  $MTF_{DL} = MTF_{2mm} \times MTF_{4mm}$ . The parameters of the models used during the computation were chosen in such a way that the responses presented similar behaviors. This situation was found for  $r_0 = 10$  and  $\sigma = 0.2\mu\text{m}$  for the equivalent diffuser and for  $r_0 = 2\mu\text{m}$  for the lateral spreading of light. As observed, the application of the models suggests a reduction in the area under the MTF for systems under the presence of fundal scattering. Moreover,  $MTF_I$  and  $MTF_{II}$  show similar behavior as that measured in the artificial eye in figure 4.1a, which indicates a reduction in the MTF in function of the characteristics of the diffuse material used as retina. Therefore, this similarity with measured data represents an additional test of the applicability of the models in real situations.

The ratios between MTF curves obtained for model I and II and that for the diffraction limited response is depicted in figure 4.5b. Although  $MTF_I$  and  $MTF_{II}$  follows similar behaviors, the ratios differs with respect to each other in the second half of the spectrum. At such

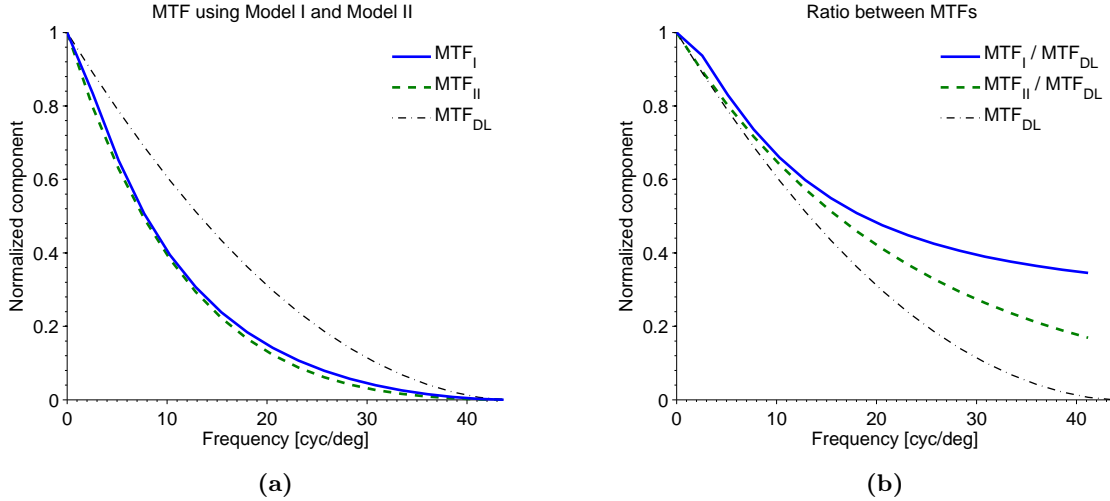


**Figure 4.5:** (a): Estimations of MTFs affected by scattering using the models for equivalent diffuser with  $r_0 = 10\mu\text{m}$  and  $\sigma = 0.2\mu\text{m}$  ( $MTF_I$ , solid line), and lateral spreading of light with  $r_0 = 2\mu\text{m}$  ( $MTF_{II}$ , dashed line). (b): Ratio between the curves computed with models I (solid line) and II (dashed line) and the diffraction limited response ( $MTF_{DL}$ , dotted-dashed line).

frequencies, the magnitude of the modulation transfer functions tends to zero and the ratios become undetermined beyond the cutoff frequency of the system. Assuming a multiplicative model for the effects of scattering in Fourier domain, the ratios may be considered as an estimation of the MTF accounting for the scattering process. However, the depicted curves indicate that such estimations can suffer inaccuracies in zones in which the magnitude of the responses involved in the process approaches to zero. Hence, if any of the models presented here are used to fit real data, the estimations at lower frequencies should have higher weight in the computations. It can be easily implemented by limiting the number of points used during the fitting process to those regions where the transfer functions present magnitudes above a user defined threshold.

### 4.3 Estimation of the scattering properties of the fundus in real eyes

The scattering properties of the ocular fundus were measured experimentally in real eyes using a calibrated version of the MEOQ system. The characteristics of this multimodal system, as well as its calibration and validation have been presented in chapter 3 of this work. However, some of the features used during the measurements reported in this section are summarized below.

The MEOQ system is a binocular device working in open field that integrates a double-pass (DP) instrument with a Hartmann-Shack (HS) sensor. It provides comparable DP and HS data after computing wavefront slopes from intersections of an ideal grid and compensating for residual errors provoked by optical defects of the measuring system. In addition, the instrument works at 801nm and compensates for spherical and astigmatic refractive errors of the eye during measurements. To do this, it incorporates a remote controlled defocus corrector based on focus-tunable lenses. In turn, astigmatism is corrected by controlling the orientation between two cylindrical lenses.

The measuring system includes a series of graphical user interfaces that help the experimenter during measurements. Among them, the interface gMEOQmain incorporates video in real time from the DP, HS, and pupil cameras. The latter ones allow the user to monitor the position of the eye and are used for alignment purposes to match the optical axis of the instrument with the one of the assessed eye. On the other hand, the experimenter can request the auto-focus option, which is a closed-loop task that sets up automatically the current in the tunable device that compensates for the actual spherical refractive error. Moreover, real time histograms are available to avoid recordings of saturated frames.

The effects of scattering were determined from deviations between DP and HS modulation transfer functions (MTF). The sections below explain the experimental procedure that was followed during measurements and the posterior data processing. Then, the DP and HS responses of real eyes are presented. The differences between curves are fitted using both of the models discussed before: the equivalent diffuser and the lateral spreading of light. Finally, the results and the applicability of the proposed models in real measurements are discussed at the end of the section.

### 4.3.1 Experimental procedure

The DP and HS modulation transfer functions (MTF) were obtained for 14 healthy subjects using the MEOQ system. The task of the person under assessment was to fixate in normal visual conditions on an external target located at a distance of six meters. A frequent task of the experimenter was to align the optical axis of the system with the one of the eyes under assessment by matching the pupil centers with the cross marks available in the real-time video provided by the pupil cameras. The proper alignment was verified before any image recording. After completing this task for the first time, the current in the tunable device belonging to the spherical refractive error corrector was modified until obtain double-pass

images with the narrowest spot. Under this configuration, the astigmatic power was obtained three consecutive times using the HS sensor. After this, the mean astigmatic power was compensated by configuring the orientation of the cylindrical lenses forming the astigmatic refractive error corrector. Then, the power of the laser source was adjusted to obtain non-saturated frames with gray-scale intensities with maxima in the range of 200 and 230.

5 series of 20 DP and HS images were recorded for each of the 14 subjects after setting up the astigmatic refractive error corrector and the power of the laser source. Within each series, first the alignment task was repeated. Then the image acquisition was requested immediately after compensating for spherical refractive errors using the auto-focus option in the remote controlled interface gMEOQmain. This process was repeated until the series of measurements had been completed. All the images were recorded using an integration time of 40ms. Regarding the refraction, the spherical and astigmatic refractive errors remained below 0.25D during measurements. If this condition was not fulfilled, the recordings were discarded and the series was initiated again to repeat the measurements.

The series of recordings were completed for each subject in a consecutive manner in a single session and under similar environment illumination conditions. The time necessary for each session depended more on the ability of the experimenter during the alignment of the instrument with the eye than on the equipment configuration and data collection. Only 3 of the 14 subjects were assessed in a binocular manner. For the rest of the cases, only the right eye was assessed. In general, the five series of measurements were carried out in around 15 minutes for the binocular cases and in around 10 minutes for the monocular measurements.

### 4.3.2 Data processing

Data processing was performed off-line after measurements using Matlab (Mathworks, 2010). First, the 20 double-pass and Hartmann-Shack images belonging to a series were averaged. In this manner, the speckle noise affecting the individual short-exposure recordings was eliminated. The resulting images were used to estimate a DP and a HS MTF per series and assessed eye.

In the case of double-pass data, the average image was Fourier transformed and corrected for residual errors of the measuring system<sup>6</sup>. Then, the MTF was obtained after proper normalization by taking the radial profile of the compensated spectral representation and

---

<sup>6</sup>The details of the compensation process can be consulted in the previous chapter of this work.

applying a peak correction [43] by extrapolating the zero frequency from a curve fitting using a two-exponential function [106]. When working with HS data, the wave aberration was estimated using the average image from spot displacements with respect to the intersections of an ideal grid using 54 Zernike coefficients. Then, the MTF was computed as the product of the autocorrelated complex pupil functions [16] for the first and second pass pupil diameters ( $MTF_{2\text{mm}} \times MTF_{4\text{mm}}$ ). The point spread function was computed by Fourier transforming both the magnitude and the phase given by the autocorrelation operation. As in the case of DP processing, HS data was compensated for residual errors before computing the radial profile of the MTF. This process is illustrated in figure 4.6.

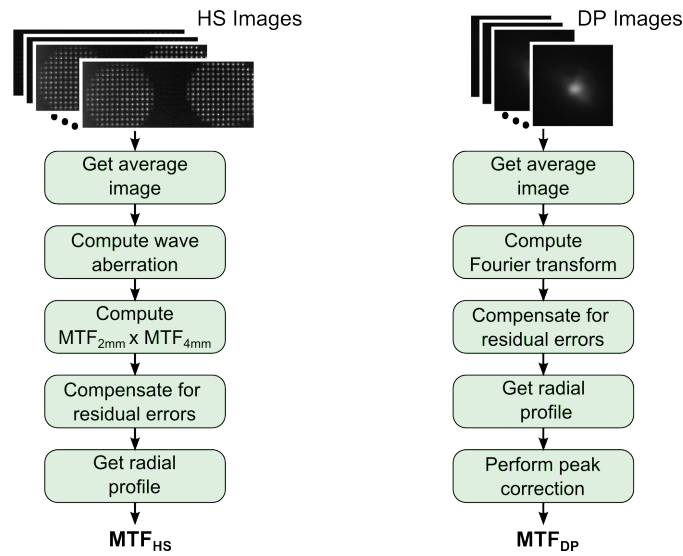


**Figure 4.6:** Flow diagram of the data processing that was followed to compute the HS (left) and DP (right) MTF for each series of 20 images.

The process described in figure 4.6 was repeated for each of the series composed by 20 recordings. At the end of this process, 5 DP and 5 HS estimations were available per eye and subject. The average curves of the 5 MTF estimations were used to compute the difference  $MTF_{Df} = MTF_{HS} - MTF_{DP}$  and the ratio  $MTF_{Rt} = MTF_{DP}/MTF_{HS}$ . Posteriorly,  $MTF_{Rt}$ , the ratio between the double-pass and the Hartmann-Shack modulation transfer functions, was fitted using both the concept of equivalent diffuser and the lateral spreading of light. In the former case, we obtained the values for correlation length  $r_I$  and standard deviations of the height fluctuations  $\sigma_I$  of an equivalent diffuser that would produce a curve  $MTF_I$  similar to the  $MTF_{Rt}$ . Equations 4.21 and 4.22 were used for this purpose considering 10 terms of the summation. On the other hand, equation 4.23 was used during the fitting process in the case of lateral spreading of light. In this manner, the resulting value for the correlation length  $r_{II}$  is the one producing the best coincidences between  $MTF_{II}$

and  $MTF_{Rt}$ . The computations were performed using a nonlinear least squares method programmed in Matlab. Additionally, the fitting process considered only those points for which the  $MTF_{DP}$  and  $MTF_{HS}$  presented values above 0.15. In this manner, the uncertainty for small magnitudes in the curves was avoided.

$$MTF_I(u) = \frac{1 + \Gamma(u)}{1 + \Gamma(0)} \quad (4.21)$$

$$\Gamma(u) = \frac{2}{mL_x''} \sum_{n=1}^{\infty} \frac{1}{n!} \frac{k^{2n} \sigma_I^{2n} r_I / n}{1 + 4\pi^2 r_I^2 u^2 / (m^2 n^2)} \quad (4.22)$$

$$MTF_{II}(u) = \exp(-2\pi r_{II} |u|) \quad (4.23)$$

Besides the MTF, there are other parameters that were obtained for each of the images belonging to a series. In the object domain, the average intensity at the edges of double-pass images ( $I_e$ ) was obtained. The DP images were processed using a cropped version of  $256 \times 256$  pixels in size. To compute  $I_e$ , the points that were considered corresponded to all those pixels whose distance from center of the image were higher than 120pixels.

The Strehl ratio was obtained for both the DP and the HS MTF. This parameter was obtained as the area under the unidimensional modulation transfer function. Because the evaluation of the scattering process is based on differences between DP and HS estimations, we computed the ratio between Strehl ratios  $SR_{Rt} = SR_{DP}/SR_{HS}$  for each series of measurements. As a result of these computations, 5 estimations of the  $MTF_{DP}$ ,  $MTF_{HS}$ ,  $I_e$ , and  $SR_{Rt}$  were available per subject and assessed eye. Although the performance of the individual estimations were similar in all the cases, the parameters presented here refer to the average of the 5 available values. In this manner, we provide a single estimate per parameter that contains the contribution of all the series of recordings for each subject.

### 4.3.3 Results and discussion

#### Differences between DP and HS responses

The point spread function for both the DP and HS techniques shows similar behaviors in all the measured cases. Figure 4.7 depicts the PSF for 4 subjects. The cases are labeled as FA,

IC, JO, and SE. Visual inspection of the images demonstrate the similarities in terms of shape between DP and HS estimations. For instance, the characteristic aspect observed for subject SE is distinguished in the images regardless the technique with which they were obtained. Another example of the similarities is observed in images for subject IC, in which a diamond-like shape is observed in both the DP and HS estimations. Although the aspect of the images follows similar patterns, it seems that DP cases include a veil surrounding the central part of the spot. This situation provokes contours for DP images less defined than for the HS estimations. This characteristic may be induced by scattering provoking angular deviations of light in the DP process, which in turn could affect the magnitude of the corresponding MTF.

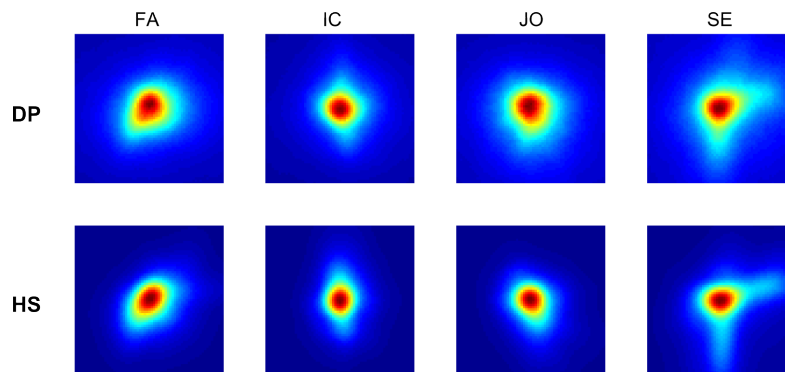


**Figure 4.7:**  $64 \times 64$  pixels cropped versions of the point spread functions obtained from DP (top) and HS (bottom) data for 4 of the 14 subjects that were measured using the MEOQ system.

Figure 4.8 presents the average DP and HS MTF curves considering the estimations for the right eye of the 14 subjects. The curves are plotted in separate figures for the sake of clarity. However, it is still possible to observe higher magnitudes of the average response for HS data. For instance, the magnitude at  $10\text{cyc/deg}$  of the HS MTF is around twice that for the DP average curve. This behavior was expected for several reasons. Among other factors, the MEOQ systems works in infrared light, which is known to be affected by scattering arising from layers of the fundus beyond the retina [3]. Moreover, HS measurements do not provide information about this phenomenon [29]. Wave aberrations were computed using nine order (54) Zernike coefficients. Since the majority of the higher order aberrations are described with eight order (42) Zernike coefficients [17], we assume that the deviations were not provoked by higher order aberrations in HS data. The subjects had an average age of 27 years and presented clear optical media. For these reasons we suppose that the effects of scattering due to the interaction of light with the surfaces of the lenses in the eye were negligible during the measurements.

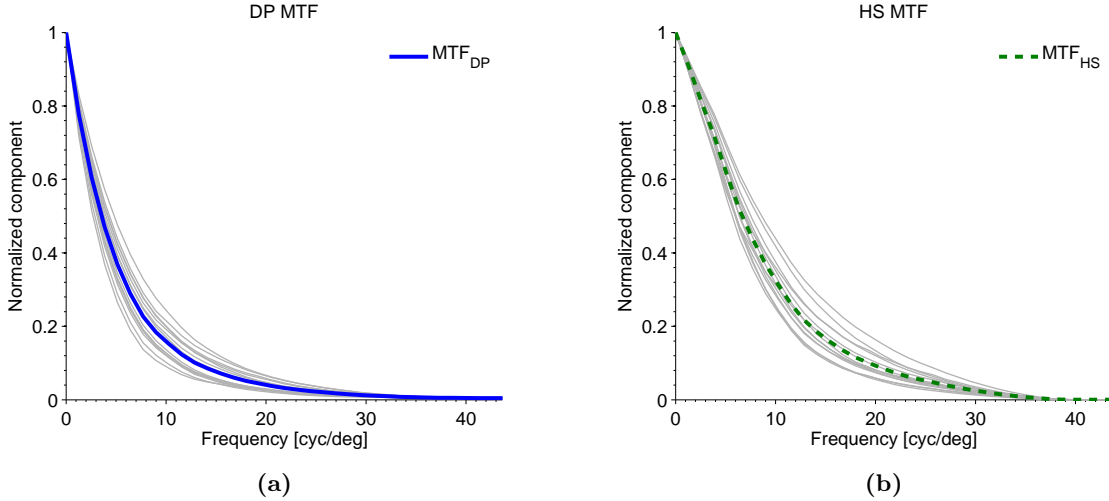


**Figure 4.8:** Average DP (solid line, left) and HS (dashed line, right) for the 14 measurements on performed on real eyes using the MEOQ system. The individual estimations are also plotted in the figures (gray solid line).

The deviations between DP and HS data are well observed in figure 4.9. Beside the average curves, the differences  $MTF_{Df} = MTF_{HS} - MTF_{DP}$  and the ratios  $MTF_{Rt} = MTF_{DP}/MTF_{HS}$  are plotted in the figure. The term  $MTF_{Df}$  shows similar behaviors for all of the measured subjects: a curve with a peak around 5cyc/deg with a magnitude fluctuating between 0.1 and 0.35. Regarding the ratios  $MTF_{Rt}$ , the curves follow a decreasing tendency around lower frequencies. Then, they present a constant behavior until reaching the cutoff frequency, were the ratio become indeterminate. There is variability among subjects in the slope of the response in the first part of the spectrum. It is also observed that the constant magnitude in the central part of the spectrum decreases with increasing slope, which could be attributed to the decrease in the magnitude of the MTF around those frequencies rather than to variations of any ocular or scattering condition among assessed eyes. This fact should be considered by giving more weight to lower frequencies during the estimation of any other parameter when using the ratio  $MTF_{Rt}$ .

Let us consider the hypothetical situation in which all eyes had been affected by the same scattering, but by different aberrations. Under this condition, the differences between the MTF curves would remain identical for all cases, regardless of the effects on  $MTF_{DP}$  and  $MTF_{HS}$  attributed to differences in aberrations. Assuming that the measuring system provides comparable data in cases without scattering<sup>7</sup>, the variations among the individual estimations

<sup>7</sup>The behavior observed during the validation of the MEOQ system suggests that the measuring instrument provides comparable data when any scattering process is present during measurements. The details can be

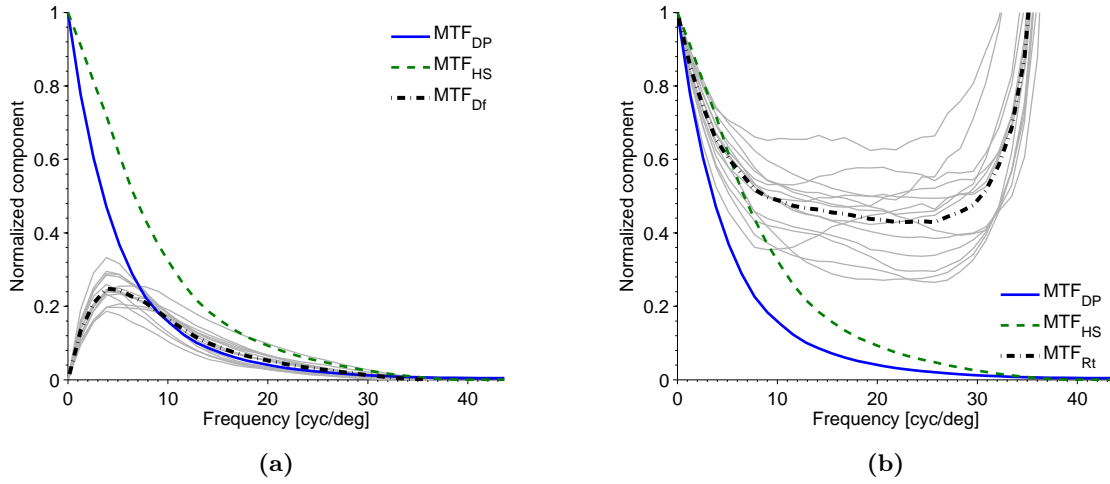


**Figure 4.9:** Average DP (solid line) and HS (dashed line) response. The average of the differences  $MTF_{Df} = MTF_{HS} - MTF_{DP}$  (a) and the ratios  $MTF_{Rt} = MTF_{DP}/MTF_{HS}$  (b) between HS and DP data are plotted in the figure (black dashed-dotted line), as well as their individual estimations (gray solid line).

observed in figure 4.9 may be attributed to changes in the amount of scattering light among the measured eyes.

### Modeling scattering

The curves  $MTF_{Rt}$  observed in figure 4.9b were fitted using the models for the equivalent diffuser (Model I,  $MTF_I$ ) and the lateral spreading of light (Model II,  $MTF_{II}$ ). The parameters of the models fitting the experimental data can be consulted in table 4.1 for the right eye of the 14 subjects. For Model I, the standard deviation of the height fluctuations  $\sigma_I$  are presented in figure 4.10a, in function of the correlation length  $r_I$ . Visual inspection of the plotted data does not reveal a clear relationship between  $\sigma_I$  and  $r_I$ . However, the tendency line fitting the results using a least squares procedure shows a small decrement in the height fluctuations of the equivalent diffuser with increments of the correlation length. On the other hand, figure 4.10b suggests a good correlation between the terms  $r_I$  and  $r_{II}$  for Models I and II, respectively. Therefore, we assume that these two parameters obtained with two different models provide information on the same phenomena, which may be related to the scattering occurring in the eye during the measurements.

The behaviors of Models I and II were obtained using  $r_I = 25.500$ ,  $\sigma_I = 0.208$ , and  $r_{II} = 4.310\mu\text{m}$ . They correspond to the average values of these parameters considering all the

---

consulted in the previous chapter of this work.

**Table 4.1:** Mean intensity at the edge of double-pass images ( $I_e$ ), Strehl ratio ( $SR_{Rt}$ ), correlation length ( $r_I$ ) and standard deviation of the height fluctuations ( $\sigma_I$ ) for Model I, and lateral spreading of light ( $r_{II}$ ) for Model II for the left eye of the 14 subjects.

Case	Label	Age	$I_e$	$SR_{Rt}$	$r_I$	$\sigma_I$	$r_{II}$
1	CC	29	5.579	0.654	22.737	0.222	3.768
2	MK	35	5.298	0.673	24.712	0.214	4.078
3	FA	30	7.389	0.713	28.114	0.193	4.538
4	XN	25	5.378	0.716	21.161	0.216	3.300
5	CY	35	7.008	0.620	30.814	0.215	5.859
6	DN	23	4.964	0.726	19.284	0.211	2.659
7	JO	28	6.153	0.703	25.524	0.198	3.783
8	BR	23	5.245	0.693	23.940	0.202	3.393
9	ST	24	6.417	0.620	26.032	0.244	4.943
10	AS	30	6.630	0.634	29.080	0.214	4.983
11	SE	26	6.131	0.749	30.789	0.171	3.673
12	IC	23	5.877	0.692	30.235	0.192	4.364
13	SL	24	7.270	0.646	37.041	0.195	7.181
14	EM	33	4.553	0.753	21.864	0.219	3.809
Average	AV	27.714	5.991	0.685	25.500	0.208	4.310

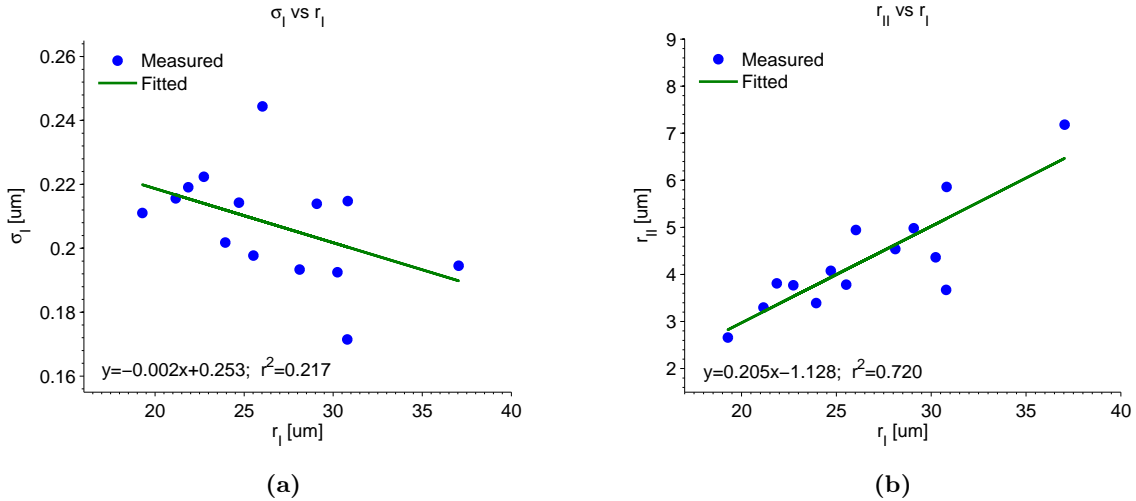


**Figure 4.10:** (a): Standard deviation of the height fluctuations  $\sigma_I$  in function of the correlation length  $r_I$  using the model for the equivalent diffuser. (b): Relationship between the correlation length  $r_{II}$  for the lateral spreading of light and  $r_I$ . The equations of the tendency lines fitting the data and the coefficients of determination are included in the figures.

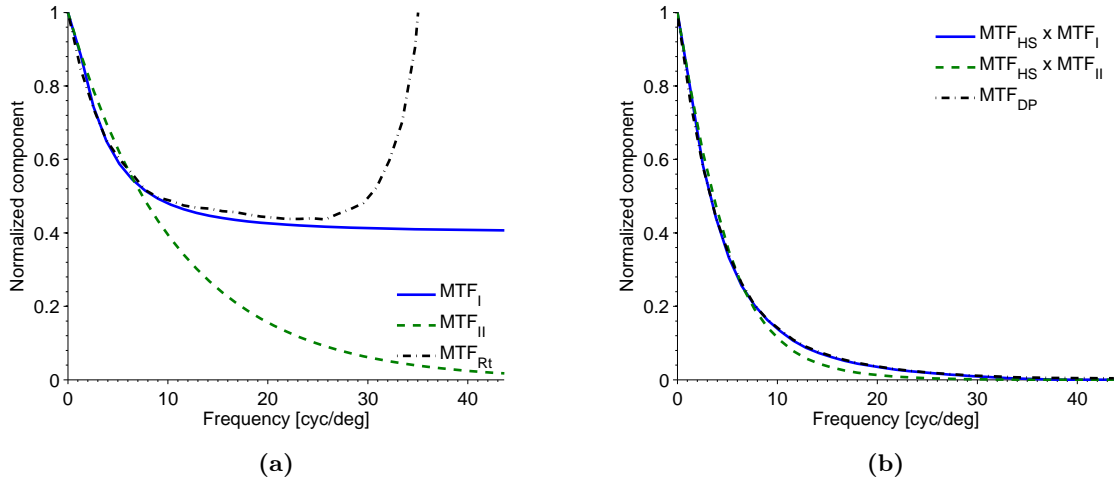


**Figure 4.11:** (a): Comparison between  $MTF_{Rt}$  and the curves  $MTF_I$  (Model I, solid line) and  $MTF_{II}$  (Model II, dashed line). (b): Comparison between  $MTF_{DP}$  (dashed-dotted line) and the curves obtained by multiplying the Hartmann-Shack response with  $MTF_I$  and  $MTF_{II}$ .

measurements. The results of the computation are observed in figure 4.11a. Curves  $MTF_I$  and  $MTF_{II}$  show good agreement with the ratio  $MTF_{Rt}$  in the lower part of the spectrum. The central part of the response is well fitted by Model I only, which presents a two-variable dependent function. While  $r_I$  dominates the decreasing trend at lower frequencies, the term  $\sigma_I$  is used to predict the magnitude around the central region of the response. However, the small magnitude of the MTF at such frequencies may be the main cause for such performance.

Figure 4.11b depicts the behavior of the Hartmann-Shack response if it was affected by scattering. To obtain the curves, the term  $MTF_{HS}$  was multiplied by  $MTF_I$  and  $MTF_{II}$  using the average values for  $r_I$ ,  $\sigma_I$ , and  $r_{II}$  presented in table 4.1. As observed, the double-pass response  $MTF_{DP}$  is practically overlapped by applying Model I to the Hartmann-Shack response. On the contrary, the expected response using Model II deviates with respect to  $MTF_{DP}$  for frequencies higher than 8cyc/deg. Nevertheless, the magnitude of the deviations is small due to the decreasing trend in the magnitude of the MTF when it approaches the cutoff frequency of the system.

The results presented in figure 4.11 suggest that both Models I and II can be used to account for differences between DP and HS data. In the former case, the average values indicate that deviations between curves may be produced by an equivalent rough surface with a correlation length of around  $26\mu\text{m}$ . This quantity is indeed higher than the expected size ( $16\mu\text{m}$ ) of a spot projected in the fundus during the double-pass process<sup>8</sup>. We suppose that the higher

<sup>8</sup>The separations between the first two minimums of the Airy patten is  $d = 1.22\lambda f / (PD/2) \approx 16\mu\text{m}$ , with

value of  $r_I$  is because the scattering process in the ocular fundus is not the result of a single surface or scatter; the correlation length computed during the curve fitting accounts for the effects of multiple scatters, which provoke an increment in the parameter due to the additive relationship among phases in composite rough surfaces [90].

The interpretation for  $r_{II}$  in Model II results easier than for  $r_I$ . For an incident ray, the parameter  $r_{II}$  denotes the lateral spreading of light provoked by the scattering process. In this manner, the average value of the fitted data suggests that each component of the incident light is spread  $4.310\mu\text{m}$  after interaction with the ocular fundus. Some authors have suggested that the interaction of light with the ocular fundus is dominated by forward scattering and the light that travels from layers beyond the retina towards the pupil comes from reflections at the boundaries of the choroid [1]. If it is true,  $r_{II}$  may also be considered an indirect estimator of the thickness of this layer because the amount of lateral spreading increases as it penetrates into the fundus.

### Effects of scattering on the DP process

The lateral spreading of light provided by Model II is shown in figure 4.12a as a function of the mean intensity observed at the edge of the double-pass images. In general, a linear relationship is observed between these two parameters among measured data. During double-pass measurements and discarding scattering from the lens of the eye, the parameter  $I_e$  could vary by changes in the environment light or in back-reflections in the optics of either the instrument or the eye. However, the measurements were performed under the same dark conditions and we did not perceive any back-reflected light that could compromise the computation of  $I_e$ . Although variations in the power of the laser source could be another factor influencing the intensity at the edge of the images, this was modified only for 3 of the 14 cases. We believe that variations of  $I_e$  in the experimental data is mainly due to scattering in the ocular fundus.

The agreement between  $r_{II}$  and  $I_e$  indicates that the constant background noise observed in double-pass images can be predicted using the model for lateral spreading of light provided by Model II. This situation suggests that  $r_{II}$  could be used to improve the accuracy of parameters in which the background noise is considered at wavelengths affected by scattering from deeper layers of the ocular fundus. For instance, the Objective Scatterer Index (OSI) proposed in [10] uses the intensities integrated by a ring between 4 and 12arcmin in the double-pass image to

---

$\lambda = 800\text{nm}$ ,  $PD = 2\text{mm}$ , and  $f = 16.3\text{mm}$ .

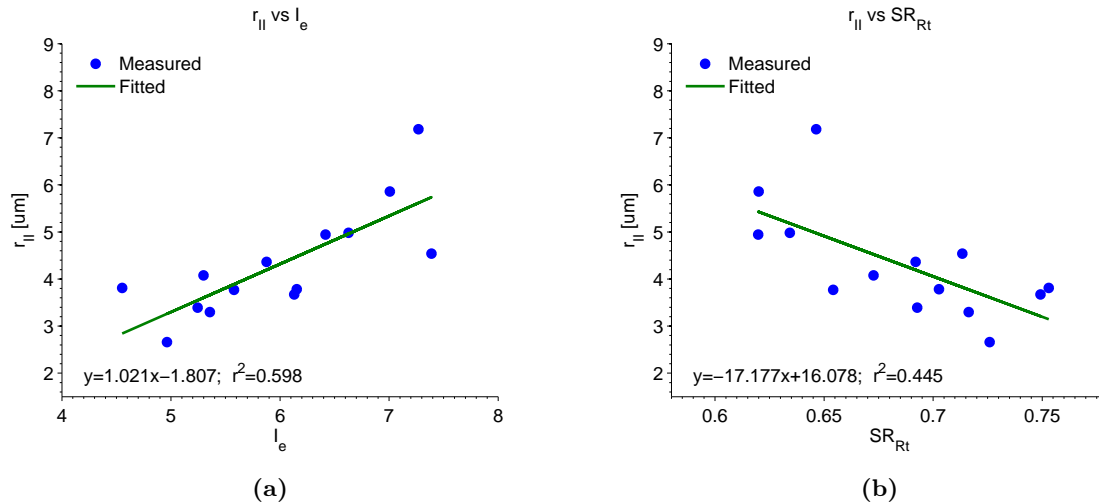


**Figure 4.12:** Lateral spreading of light  $r_{II}$  in function of the mean intensity at the edge of double-pass images  $I_e$  (a) and ratio between the DP and HS Strehl ratios  $SR_{Rt}$  (b). The equations of the tendency lines fitting the data and the coefficients of determination are included in the figures.

provide an estimator to classify cataracts. However, this region could be affected by changes in the scattering conditions in the fundus at certain wavelengths. Therefore, the uncertainty during the classification of cataracts could be reduced by introducing the lateral spreading of light in the computations.

Figure 4.12b depicts the relationship between  $r_{II}$  and the ratio  $SR_{Rt}$ . Because larger values of lateral spreading of light indicates higher deviations of DP response with respect to HS data, the inverse relationship between these two parameters was expected. Although they both vary in function of  $r_{II}$ , the light at the edges of the double-pass images  $I_e$  and the ratio between the DP and HS Strehl ratios  $SR_{Rt}$  are quantities that are not directly related with each other. The effects of the constant background noise provided by  $I_e$  are observed in the Fourier domain as an increase of the response at zero frequency, which is then compensated by the peak correction performed during the computation of the MTF [43]. Therefore, the trends observed in the plots of figure 4.12 provide information about the same phenomena, but measured in different manners.

The variations of  $r_{II}$  with age are depicted in figure 4.13. The tendency line plotted in the graph suggests a small increment in the lateral spreading of light with age within the measured range. The shorter values of  $r_{II}$  were found for younger subjects. The subject with the highest deviation with respect to the tendency line is observed in the age range of 20 to 25 years old. This situation corresponds to subject SL, who has a lateral spreading of  $7.181\mu\text{m}$ , a value higher than  $4.310\mu\text{m}$ , the mean value of the 14 estimates. Assuming that the deviation

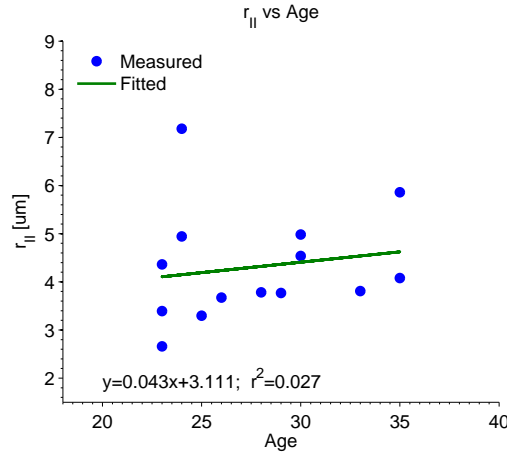


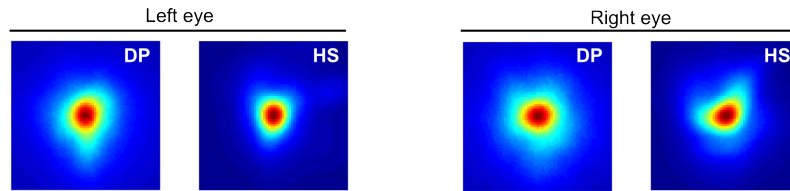
**Figure 4.13:** Lateral spreading of light  $r_{II}$  in function of age. The equation of the tendency lines fitting the data and the coefficient of determination are included in the figure.

was not provoked by scattering in the lenses of the eye, it may be related to changes in the structure of the ocular fundus for this subject with respect to a young eye.

During the measurements, the scattering arising from the interaction of light with the eye lenses was not verified by other instruments or methods because the majority of the measurements were performed on young eyes. The performance of fundal scattering could be characterized in a more accurate manner by determining with objective (or subjective) methods the influence of the eye lenses during measurements. We believe that the tendencies presented in this section reflect the influence of fundal scattering in double-pass measurements. The effects on the DP process were quantified in terms of  $r_{II}$ . From the linear relationship between this parameter and  $r_I$ , the analysis performed in this section applies also to Model I.

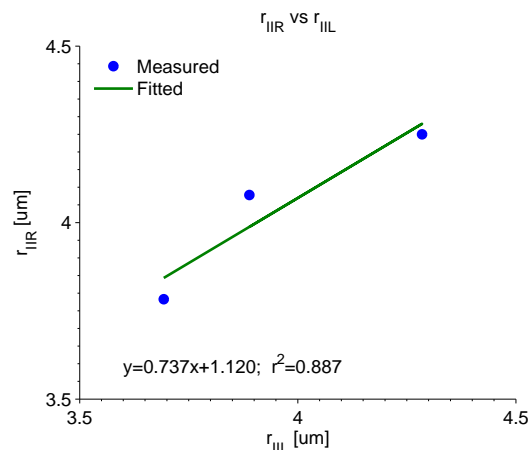
### Binocular performance of scattering

Figure 4.14 depicts the DP and HS point spread function computed from binocular measurements on subject MK. The information of both eyes was assessed simultaneously. Referring to DP images, it is observed in both eyes a kind of protuberance at the bottom part of the spot. There are some variations between the images for the left and right eye, which could arise in part from misalignments between the optical axis of the instruments and the eyes. The alignment process was an important task of the experimenter before data collection, but the movements during image recording were not controlled during experimentation. However, we expect that the computation of parameters from binocular measurements was not compromised by this situation.



**Figure 4.14:**  $64 \times 64$  pixels cropped versions of the point spread functions obtained from DP and HS data for the left and right eyes of subject MK.

The relationship between the left and right eye is shown in figure 4.15 in terms of the lateral spreading of light for Model II. It is not accurate to find a trend using three estimations only, but the results suggest that the parameters for the left and right eye follow a linear dependence. In an ideal case where both eyes had equal performance, the slope of the tendency line fitting the experimental data should approach to one. Although the slope presents a value of 0.737, we found that both eyes present similar performance for the three subjects assessed binocularly. We only present the relationship between  $r_{IIL}$  and  $r_{IIR}$ . The relationship of these parameters with  $I_e$ ,  $SR_{Rt}$ , or age can be derived from the analysis presented in previous sections.



**Figure 4.15:** Relationship between lateral spreading of light for the left ( $r_{IIL}$ ) and right ( $r_{IIR}$ ) of the 3 subjects assessed binocularly. The tendency line fitting the data, its equation, and the coefficient of determination are included in the figure.

## 4.4 Conclusions

This chapter presented an analysis on the scattering properties of the ocular fundus based on differences between DP and HS measurement. For this, we use the MEOQ system, which provides comparable data using these two techniques and works with infrared light. Two models have been introduced that incorporate the effects of fundal scattering into the double-pass process. In the first case, the concept of equivalent diffuser is used to find the statistical

characteristics of a rough surface that would produce the same effects as those observed in experimental measurements. For the second model, the scattering is expressed in terms of the lateral spreading of light produced by the ocular fundus. The experimental results suggest on the one hand that the MEOQ system may be used to provide estimates of the scattering occurring in ocular fundus, and on the other hand that the models proposed here fit well the differences between DP and HS measurements in frequencies at which the MTF contains enough information on fundal scattering.

The characterization of the scattering process occurring in the fundus may be used not only to understand the differences between double-pass and Hartmann-Shack data, but also to improve the accuracy of other parameters. For instance, the background noise affecting double-pass images may influence the computation of the Objective Scatterer Index, which has been used to classify cataracts. The results suggest that this background noise is modified with variations of fundal scattering. In this sense, the use of multimodal systems and models accounting for different phenomena in the eye can be a useful tool to separate the effects of the processes involved in double-pass measurements.

Data presented here show that ocular scattering may affect the computation of the Strehl ratio, which is a parameter usually used to provide information about the retinal image quality. We cannot assure that fundal scattering at visible light affects the perception of external scenes during the image formation process. However, deviation of the parameters with information on fundal scattering from mean values could be an indicator of other problems that could be related with vision. Nevertheless, further research is necessary to corroborate this point.

## Chapter 5

# Aberration-free index to quantify scattering in the human eye

There are different phenomena involved in the interaction between light and eye in the double-pass (DP) technique [20]. It is well known that optical quality estimators obtained with this assessment mode comprise the effects of diffraction, aberrations, and scattering that occur in the eye [10, 17, 37]. In the case of diffraction and aberrations, light is affected by apertures truncating spatially incident waves [16], by defocus and astigmatism, and by higher order aberrations in the lens of the eye [45, 123]. Regarding scattering, inhomogeneities in the structures of the eye with which light interacts deviate the incident radiation from a straight trajectory [11, 124]. This situation is perceived in double-pass images as halos surrounding the point-spread function (PSF) [109] with a magnitude and angular position of affectation that is a function of the characteristics of the scattering media [90, 125, 126].

The interaction of light with the eye lens is the main source of scattering in the double-pass process [14]. However, the ocular fundus may also contribute to scattering formation at certain wavelengths [116], as seen in chapter 4 of this work. Traditionally, the presence of inhomogeneities in the crystalline lens have been associated with cataracts [127], that may degrade the retinal image quality [40, 109, 120]. For this reason, the study of intraocular scattering has received special attention in visual optics. Some authors have suggested that scattering arising in the ocular fundus has a minimum impact in vision [84]. Anyhow, this is a wavelength dependent phenomenon [116] and its effects may be present in greater or lesser extend during the quantification of scattering by objective means [3].

The double-pass technique has arisen as an excellent tool for the objective quantification of

---

scattering. For instance, Artal *et al.* propose in Ref. [10] an objective scatter index (OSI) based on the analysis of the point spread function (PSF) of the eye at an eccentric location with information on scattering. This method is indeed used in a commercially available clinical instrument [28] and has been used to classify cataract patients [40]. However, the quantification of scattering may be compromised under the presence of uncorrected aberrations affecting regions of the PSF involved in the computation of the index [10].

Some authors have analyzed scattering by combining double-pass data with that obtained with assessment modes that are known to be unaffected by scattering. Among them, Shahidi and Yang and Díaz-Doutón *et al.* made comparisons with respect to Hartmann-Shack data to provide estimations of scattering based on the differences between the areas under the line spread function (LSF) [85] and the modulation transfer function (MTF) [29] of the multiple techniques. In the case of Rodríguez and Navarro in Ref. [86], the authors quantified the effects of scattering by finding the parameters of an equivalent diffuser producing the differences between the MTF of a double-pass instrument and a laser ray tracing aberrometer.

There have been some efforts to measure scattering using assessment modes other than the double-pass technique. Nam *et al.* analyzed the spots in Hartmann-Shack images to obtain a spatially resolved quantification of scattering at the pupil plane of the eye [57]. More recently, Ginis *et al.* proposed a method that enables to assess regions of the PSF of the eye that are often not available with the conventional double-pass technique, but with information of scattering [2]. It should be pointed out that these systems quantify scattering, but considering only those small regions of the crystalline lens with which light interact during the measurements.

This chapter aim to present a method for quantifying scattering from double-pass measurements after minimizing the influence of aberrations in the measured data. To do this, we use the information contained at lower frequencies of the modulation transfer function, which is usually eliminated under conventional data processing of double-pass information after extrapolating those values from a curve fitting using two exponential functions [43, 106]. We suggest that this process removes data containing the effects of scattering, including those arising in the crystalline lens. Therefore, we combine the raw MTF with that obtained after the peak correction to provide an aberration-free index with information on the scattering affecting the lower part of the spectrum. Measurements on an artificial eye corroborate the applicability of this concept to quantify scattering for different refractive conditions. In addition, the effects of the ocular fundus on the modulation transfer functions are also analyzed

with the ideal device modeling the eye using materials with different diffuse properties. The analysis is completed with the quantification of scattering in real eyes using the proposed method from DP images obtained with the MEOQ system.

This chapter is organized as follows. First, the effects of scattering on the double-pass response are analyzed from the point of view of the data processing performed over the images until obtaining the modulation transfer function of the eye. This information is considered to propose the method for quantifying scattering after removing the effects of aberrations in the double-pass response. The method is corroborated with measurements on an artificial eye for different refractive conditions and diffuse materials acting as ocular fundus. After presenting and discussing the results of the scattering quantification in real cases, the chapter ends with conclusions on the proposed method.

## 5.1 Scattering and double-pass data processing

In double-pass systems, the parameters describing the optical quality of the eye are derived from images recorded in a conjugate plane of a point source projected on the retina [20]. Since light passes through the optics of the eye, the images contain the effects of aberrations [13]. In addition, inhomogeneities either in the crystalline lens or in the ocular fundus impress their mark in the sense that the incident energy is oriented towards a variety of directions in function of the statistical properties of the diffuse material producing the scattering [90, 121]. Therefore, the point spread function of the eye is affected by a veiling glare from the scattered light [109]. This situation is illustrated in figure 5.1, which depicts the radial profile of two double-pass images affected by different amount of scattering. As observed, the veil is perceived as an increment in the intensity at the base of the PSF of the eye.

There are some differences in the manner in which intraocular and fundal scattering affect the PSF of the eye. Figure 5.2 presents the cumulative light distribution at different angular positions. The images were taken from the work of Ginis *et al.* in [2, 3] and correspond to reconstructions for different scattering conditions at the pupil (figure 5.2a) and fundus plane (figure 5.2b). The plots indicate that at small angles the point spread function may show higher variations for scattering caused by the fundus than for that from the crystalline lens. This situation is relevant because it suggests that in infrared light the central part of the response available in the double-pass technique could be affected by scattering arising from the complex reflection process occurring in the ocular fundus.

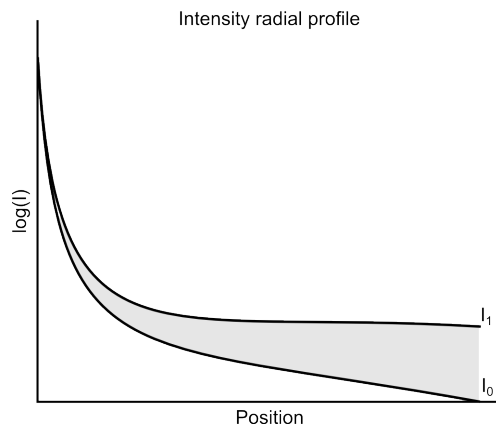


**Figure 5.1:** Illustrative representation of the radial profile of two double-pass images with different amounts of scattering. It is assumed that the profile  $I_1$  contains stronger scattering than  $I_0$ .

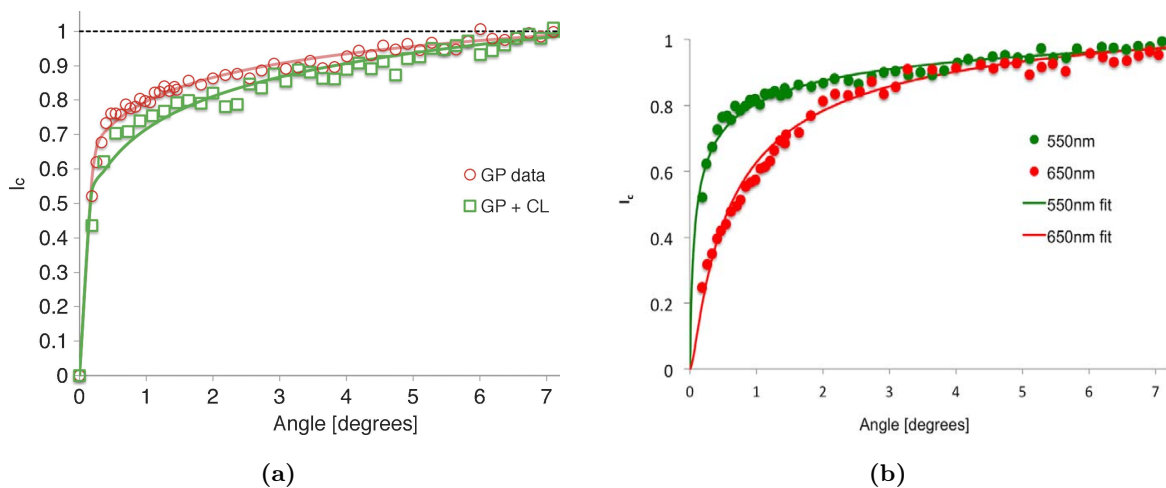


**Figure 5.2:** Cumulative intensity profile of the PSF. Measurements on a subject for different intraocular scattering (a; without scattering, red circles; with induced scattering, green squares) and for different wavelengths (b; 550nm, green circles; 650nm, red circles). The variations in function of the wavelength are attributed to different amount of scattering from the fundus. Images taken from [2] and [3].

The increment of intensity caused by scattering at the outer segment of the PSF was used by Artal *et al.* in [10] to define the so called objective scatter index (OSI). This method for quantifying scattering is defined as the ratio of the integrated light in a ring between 12 and 20arcmin to that contained within 1arcmin in the central zone of the PSF. Although the limits of the outer part of the double-pass images used during the computation allows to avoid the influence of uncorrected low-order aberrations, the authors suggest that the index may be affected by refractive errors higher than 1D [10]. The OSI has been used to classify cataract patients [10, 40]. However, it may contain contributions from scattering arising in the ocular fundus to a lesser or greater extent in function of the wavelength of the measurement system, which would be interpreted as an offset in the computed index during cataract classification [2].

Conventional data processing performed over double-pass images is shown in figure 5.3. In this process, the modulation transfer function is obtained after proper normalization as the modulus of the Fourier transformed double-pass image [37]. The radial profile of this calculation tends to present a peak at zero frequency containing information of ocular scattering and noise coming from light reflected by the cornea or by the own measuring system [13]. In this manner, the peak causes a decrease in the MTF at frequencies different from zero. These effects are usually eliminated by substituting the DC component in the spectral representation for an extrapolated value obtained from a fitting function which considers the rest of the measured data [43]. As a consequence, the peak correction may eliminate the effects of scattering contained at the zero frequency. However, the data that is eliminated may be used to provide an index with information on scattering.

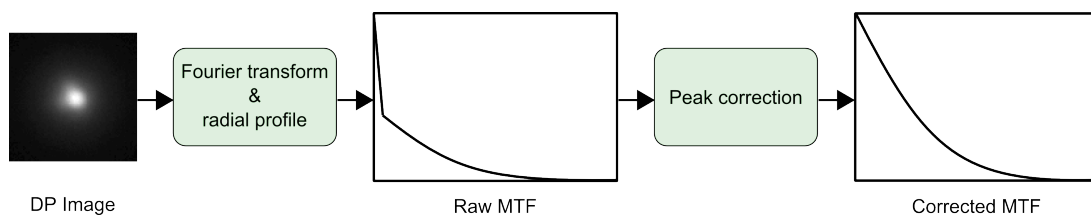


**Figure 5.3:** Conventional data processing performed over double-pass images until obtain the modulation transfer function (MTF) of the eye.

In chapter 4, the MEOQ system was used to obtain double-pass and Hartmann-Shack data. From there, data obtained during the calibration process suggest that comparable responses between techniques may be reached when scattering is not present in the measurements. Such a condition was obtained by illuminating the system with collimated light from the eye's pupil plane; that is, by avoiding scattering arising from the interaction of light with the structures

of the eye. This configuration was used to obtain data for different amounts of induced refraction. Taking those results, we can infer that double-pass data kept information about aberrations.

Besides maintaining information about aberrations [13], the double-pass MTF after peak correction may contain the effects of scattering influencing the response of the eye at frequencies larger than zero [29]. It is not possible to know with accuracy if contributions of scattering to the MTF comes from the crystalline lens or from the ocular fundus. However, we expect that the MTF after correction in infrared light would be mainly affected by fundal scattering because this type of scattering may modify the point spread function not only at the background, but also at angular positions with relevant information on diffraction and aberrations [3]. This situation will be studied in more detail in section 5.4.

## 5.2 The Aberration-Free Scatter Index (AFSI)

If the PSF of the eye computed with double-pass systems contains information on scattering [10], the MTF obtained through a Fourier transformation may also be influenced by it. Therefore, the MTF could be used to provide an index representative of the amount of scattering affecting the eye under assessment. In particular, we could use the MTF obtained after peak correction to filter, from the raw data, the effects of aberrations prior to the computation of the index. In this manner, the index would use the information contained at lower frequencies, which are known to be affected by scattering [37].

Instead of using the PSF of the eye as done for the computation of the OSI [10], we propose to use the MTF before and after peak correction to obtain the AFSI, the Aberration-free Scatter Index. We define the AFSI is defined as the average value of the ratio between the MTF before and after peak correction. The proposed index is expressed as

$$AFSI = \frac{1}{R} \int \frac{MTF_r(r)}{MTF_c(r)} dr \quad (5.1)$$

where  $MTF_r$  and  $MTF_c$  are the modulation transfer function obtained after Fourier transformation (raw MTF) and peak correction (corrected MTF),  $r$  represents radial coordinates in the frequency domain, and  $R$  stands for the length of the signal. Both  $MTF_r$  and  $MTF_c$  are curves normalized to their value at zero frequency during the computation of the index.

With  $N$  representing the set of consecutive values over which  $n$  varies, in the discrete-time case the index is expressed as

$$AFSI = \frac{1}{N} \sum_{n=1}^N \frac{MTF_r[n]}{MTF_c[n]} \quad (5.2)$$

During peak correction, only data at the lower part of the spectrum are substituted by those computed from a fitted curve [37]. The rest of the information in the MTF remains unaltered by this process. Because by definition the MTF is normalized to the magnitude at the lowest part of the spectrum [16], the computation of the ratio  $MTF_r/MTF_c$  results in a curve with a peak at zero frequency taking a value of one followed by a constant value with lower magnitude for all those frequencies that are unaffected by the extrapolation process, as illustrated in figure 5.4. The magnitude of the constant part in the response contains the information on scattering and has the highest weight during the computation of the index. From the manner in which it is obtained, the AFSI consists of a number between 0 and 1; if data do not contain any scattering, the raw and extrapolated data would be the same and the index would take a value of 1. On the contrary, the higher amounts on scattering in the response, the closer the value of the AFSI to 0.

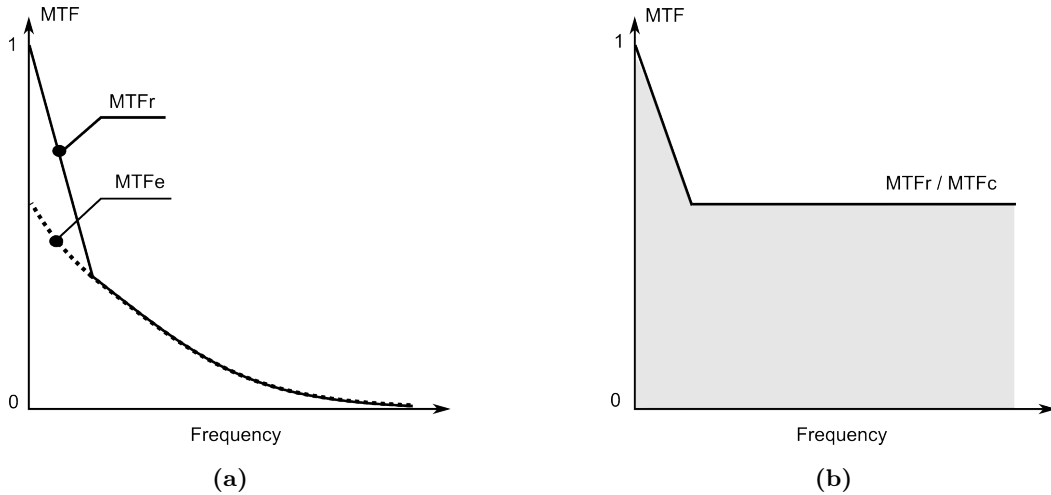


**Figure 5.4:** Illustration of the modulation transfer function before ( $MTF_r$ ) and after ( $MTF_e$ ) peak correction before normalization (a). The typical shape of the curve obtained as  $MTF_r/MTF_c$  is shown in (b).  $MTF_c$  represents the normalized version of  $MTF_e$ . The shaded area indicates the data used during the computation of the AFSI.

The method that is being proposed to compute the AFSI is illustrated in figure 5.5. A number of images are first averaged to obtain realizations that are not affected by speckle.

The resulting average image is Fourier transformed and then the radial profile of its modulus is normalized to the magnitude at zero frequency to obtain the raw MTF. The corrected MTF is obtained after proper normalization by extrapolating the lower frequencies from a fitting curve using a two-exponential function. Then, the raw and corrected MTF curves are used to compute the index as the average value of the ratio  $MTF_r/MTF_c$ . This procedure is applied off-line using Matlab (Mathworks, 2010) and corresponds to the one followed to compute the values of AFSI presented in the following sections.

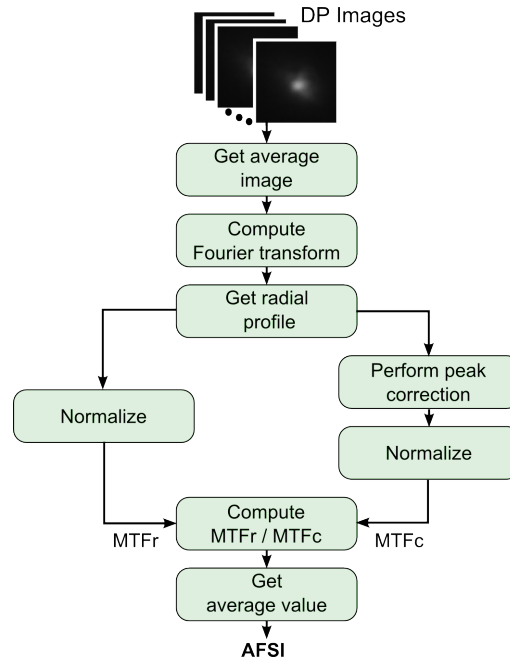


**Figure 5.5:** Proposed method to compute the AFSI from DP images.

### 5.3 The AFSI for different refractive conditions

The performance of the AFSI is analyzed in this section for different amounts of intraocular scattering induced in an artificial eye for different refractive error conditions. The device used during measurements consisted of a lens with  $f' = 50\text{mm}$  focal length followed by a cardboard acting as ocular fundus. The diffuse material was mounted on a rotating motor to break temporal coherence and to obtain images unaffected by speckle. To induce different amounts of scattering, the commercially available diffusers  $S_1$  (Tiffen, Black Pro-Mist 1 Filter) and  $S_2$  (Tiffen, Black Pro-Mist 4 Filter) were placed in front of the artificial eye. From the characteristics of the material, we expect higher light diffusion for  $S_2$  than for  $S_1$ . The refractive errors were generated by placing trial lenses  $L_1$  and  $L_2$  at around 15mm in front of the lens. Lenses  $L_1$  and  $L_2$  were used during measurements to generate a defocus of 0.25 and

0.50D, respectively.

The artificial eye was measured for the different amounts of induced scattering and refractive errors using the right-eye optical path of the MEOQ system. The characteristics of the system have been presented in chapter 3 of this work. Although the system is able to provide comparable double-pass and Hartmann-Shack data, here we used only the former technique to analyze the presence of scattering. Since we wanted to conserve the information contained in the double-pass image, the compensation for residual errors described in chapter 3 was not applied to the measured data.

The measurements were carried out in the following manner. First, the position of the spherical refractive error corrector was configured by setting up in the focus tunable lens the power with which the image with the best optical quality (smallest spot) was obtained for the artificial eye without any induced diffusion or aberration. After this, 5 images were recorded for each of the following combinations of diffusers and trial lenses:  $(S_0, L_0)$ ,  $(S_0, L_1)$ ,  $(S_0, L_2)$ ,  $(S_1, L_0)$ ,  $(S_1, L_1)$ ,  $(S_1, L_2)$ ,  $(S_2, L_0)$ ,  $(S_2, L_1)$ ,  $(S_2, L_2)$ , where  $S_0$  and  $L_0$  refers, respectively, to the cases in which no diffuser or trial lens was placed in front of the eye. Before image recording, the power of the laser source was configured in such a way that the peak intensity remained between 200 and 230 in gray levels for all the measured cases.

The average of the 5 images available for each of the combinations was used to compute the corresponding value of AFSI after following the procedure described in the flow diagram of figure 5.5. In addition, we computed the average value of both the raw and the corrected MTF to observe the performance of these parameters until the computation of the AFSI. For comparison purposes, we also provide the OSI computed directly over the double-pass image. The average value of the curves  $MTF_r$  and  $MTF_c$ , as well as the OSI were normalized to that computed over the combination  $(S_0, L_0)$ .

The behavior of both the raw and the corrected MTF can be seen in figure 5.6. In the case of  $MTF_r$ , the plotted data indicate variations in the ratio between magnitudes for the first and second point in the curves arising from the presence of either the aberrations or scattering in the measurements. In general, the higher the presence of aberrations or scattering, the lower the magnitude of the response for coordinates beyond the zero frequency. In this manner, the maximum and minimum magnitudes are found for the combinations  $(S_0, L_0)$  and  $(S_2, L_2)$ , respectively. The  $MTF_c$  curves indicate that the effects of the induced scattering are practically eliminated after peak correction. This is observed from the fact that the curves for a given diffuser are overlapped in figure 5.6b, which suggests that the presence of aberrations

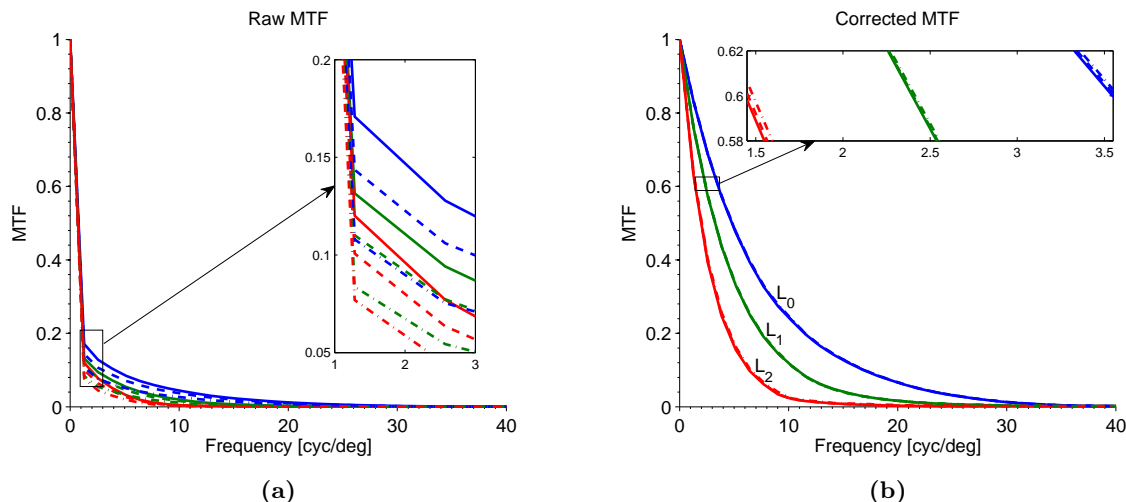


**Figure 5.6:** Raw (a) and corrected (b) MTF for diffusers  $S_0$  (solid line),  $S_1$  (dashed line), and  $S_2$  (dotted-dashed line) and refractive errors  $L_0$  (blue line),  $L_1$  (green line), and  $L_2$  (red line). The rectangles on the images indicate data in a zoomed area.

dominates the behavior of  $MTF_c$ .

The fact that the scattering effects are eliminated through the peak correction process has important implications for the quantification of this phenomenon using the MTF. Some authors have used data from multiple techniques to estimate the effects of intraocular scattering [29, 86]. Examining images reported by the authors, we suppose that they used a corrected version of the MTF during the quantification. However, if the effects of the scattering from the crystalline lens are eliminated by applying the peak correction to the measured responses, the differences between the curves should have another origin. In the case of [29], the measurements were performed with independent instruments at different times using infrared light. Therefore, variations in both the refractive conditions between measurements and the amount of scattered light from the fundus among subjects could have affected the results. On the other hand, data in [86] were obtained simultaneously using a single system in green light, which have a shorter penetration in the ocular fundus [1]. However, the correlation lengths of the equivalent diffuser computed from the differences between techniques do not match with the expected and there is a considerable variability among subjects. Nevertheless, at this moment we cannot assure that diffusers used during the experiments produced diffusion with equivalent characteristics to that observed in real eyes. In this sense, a further characterization of the diffusers would be necessary to relate their parameters to real situations.

Figure 5.7a indicates the average of the MTF curves before and after peak correction. As expected from the behavior of  $MTF_r$ , a decrease in this parameter is observed with respect

to data for  $L_0$  as a function of the defocus induced with lenses  $L_1$  and  $L_2$ . Although this performance is observed for all the diffusers, the amount of scattered light in the measurements seems to induce a shift in the average value. The variations produced by  $S_0$ ,  $S_1$ , and  $S_2$  are not observed in the average value of the MTF after peak correction. However, the impact of the induced defocus in  $MTF_c$  is more significant in this case.

The computed values of OSI and AFSI are plotted in figure 5.7. As observed, the OSI is affected by the defocus induced with lenses  $L_1$  and  $L_2$ . In this manner, this index considers increments in aberrations as variations in the amount of diffused light in the double-pass images. For a given amount of induced defocus, an increment in the index is observed. Therefore, the OSI is able to detect different amounts of scattering, but is also influenced by the presence of aberrations during measurements. On the contrary, data in figure 5.7b suggest that the AFSI provides values in which it is possible to observe differences produced by scattering alone despite the presence of aberrations.

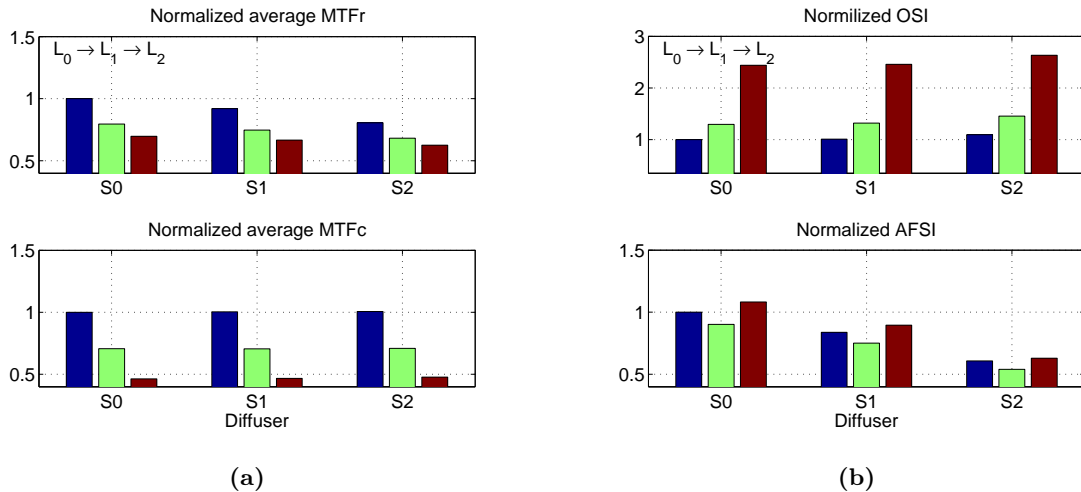


**Figure 5.7:** Bar plots indicating the average value of the raw (a, top) and corrected (a, bottom) MTF and the amount of scattering quantified through the OSI (b, top) and the AFSI (b, bottom). The data is presented for different amount of scattering and aberrations induced with diffusers  $S_0$  (left bars),  $S_1$  (middle bars), and  $S_2$  (right bars) and lenses  $L_0$  (blue bar),  $L_1$  (green bar), and  $L_2$  (red bar), respectively.

The values of AFSI presented in figure 5.7b indicate, as expected, a decrease of the parameters with increasing scattered light. There are some variations among values computed for a given diffuser. We believe that these changes are produced by different amounts of reflections in the lens of the artificial eye (corneal reflections) during measurements. Data for lenses  $L_0$  and  $L_1$  were obtained using the same power of the laser source. However, the diffuser could provoke a decrease in the amount of light reaching the eye, producing in this manner a lower amount of corneal reflections and a reduction in the AFSI. On the other hand, it was necessary to

increase the power of the laser source to maintain the intensity levels between 200 and 230 in the image during measurements for lens  $L_2$ . This situation could have induced an increase in the mean value of the  $MTF_r$ , which affects the computation of the AFSI. However, it is still possible to observe that the amount of scattering in the images dominates the behavior of the aberration-free objective scatter index, the AFSI.

Table 5.1 includes the values of AFSI computed for the different combinations of induced scattering and aberrations. As stated before, these data suggest that the AFSI can be used to quantify scattering under the presence of aberrations. The mean values presented in the table suggest a clear reduction in the AFSI for increasing scattered light. Measurements in real situations on eyes with different amounts of intraocular scattering could be used to propose ranges of the index indicating the presence of cataracts.

**Table 5.1:** Values of OSI and AFSI computed for the different combinations of diffusers ( $S_0$ ,  $S_1$ , and  $S_2$ ) and lenses ( $L_0$ ,  $L_1$ , and  $L_2$ ). The man value and standard deviation of the OSI and AFSI per diffuser is also presented in the table.

Lens	OSI			AFSI		
	$S_0$	$S_1$	$S_2$	$S_0$	$S_1$	$S_2$
$L_0$	1.000	1.011	1.097	1.000	0.839	0.608
$L_1$	1.297	1.322	1.456	0.902	0.752	0.540
$L_2$	2.441	2.459	2.636	1.080	0.895	0.629
Mean	1.579	1.597	1.730	0.995	0.829	0.592
std	0.761	0.762	0.806	0.090	0.072	0.046

## 5.4 The AFSI for ocular fundus of different characteristics

The effects of the scattering from the ocular fundus over the computation of the AFSI are analyzed in this section. To do this, we used the diffusers  $S_1$  and  $S_2$ , artificial eye, apparatus, and data processing presented in section 5.3. To induce different amount of scattering, we used cardboards  $R_1$  and  $R_2$  as ocular fundus in the artificial eye. Quantified with the 3D profiler PLu apex (Sensofar), the cardboards presented height fluctuations (standard deviations) of  $3.984$  and  $0.900\mu\text{m}$  in diffusers  $S_1$  and  $S_2$ , respectively. In this manner, we expect higher scattering for cardboard  $R_1$ , which corresponds to the one used during the measurements presented in the last section.

The methodology used during measurements for each of the cardboards acting as ocular

fundus was the following. First, the optical power in the tunable focus lens of the spherical refractive error corrector was modified until the image obtained had the best optical quality. After configuring the power in the laser source to obtain non-saturated frames with peak intensities above 200 in gray levels, 5 images were recorded for each of the induced amounts of intraocular scattering. In this manner, at the end of the session images were available for the following combinations:  $(R_1, S_0)$ ,  $(R_1, S_1)$ ,  $(R_1, S_2)$ ,  $(R_2, S_0)$ ,  $(R_2, S_1)$ , and  $(R_2, S_2)$ . During data processing, the average image for each of the combinations was used to compute the MTF before and after peak correction following the procedure described in figure 5.5. The OSI and the average value of  $MTF_r$  and  $MTF_c$  were obtained and normalized to that computed over the combination  $(R_1, L_0)$ .

Figure 5.8 shows the MTF before and after peak correction. There is a variation in the magnitude of the  $MTF_r$  from the differences in scattering from both the pupil and the fundus plane. In general, the magnitude for the non-zero frequencies shows a reduction with increasing amounts of scattering in double-pass images. The behavior of  $MTF_c$  indicates that the peak correction has information on scattering from the fundus, but not on that induced in the pupil plane of the artificial eye. Since images were obtained for both retinas for positions in the spherical refractive error corrector for the best optical quality, we assume that the differences observed between  $R_1$  and  $R_2$  are not caused by defocus coming from a shift in the plane of the fundus due to differences in thickness between cardboards. In this manner, variations in the characteristics of the ocular fundus among subjects could dominate the computation of parameters derived from the MTF after peak correction at certain wavelengths.

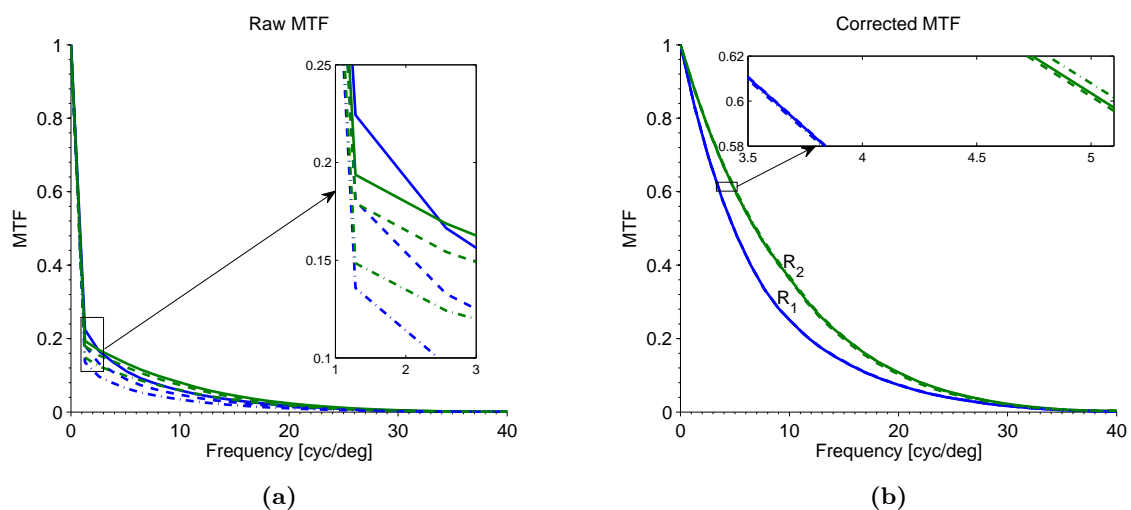


**Figure 5.8:** Raw (a) and corrected (b) MTF for diffusers  $S_0$  (solid line),  $S_1$  (dashed line),  $S_2$  (dotted-dashed line) and ocular fundus  $R_1$  (blue line) and  $R_2$  (green line). The rectangles on the images indicate a zoom over the illustrated area.

The average value of curves  $MTF_r$  and  $MTF_c$  is presented in figure 5.9a. The effects of  $S_0$ ,  $S_1$ , and  $S_2$  are observed in the average over the raw data as a decrease in the computed value. This behavior suggests that raw data contain information about scattering, but that it is also affected by that from the fundus. In turn, variations in the scattering at the pupil plane are not reflected by  $MTF_c$ , which shows variations between  $R_1$  and  $R_2$  only.

The computation of the OSI and AFSI over the images is presented in figure 5.9b. The plotted data indicate that the OSI is strongly affected by changes in the scattering arising in the ocular fundus. There is a small increase in the parameter for increasing intraocular scattering. However, these variations are almost negligible when compared to those produced between data for  $R_1$  and  $R_2$ . The AFSI is less influenced by scattering from the fundus. We believe that the peak correction eliminates part of the effects of this kind, probably because it affects regions in the MTF that are used to estimate the fitting function employed during the extrapolation process. The variations in the AFSI for a given diffuser at the pupil plane may be provoked by reflections in the lens of the artificial eye or by the presence of scattering from the fundus. However, it has to be stressed that the AFSI is able to detect differences that are related with variations of intraocular scattering during measurements. Moreover, the values of AFSI are visually equivalent to those observed in figure 5.7b for the same diffusers.

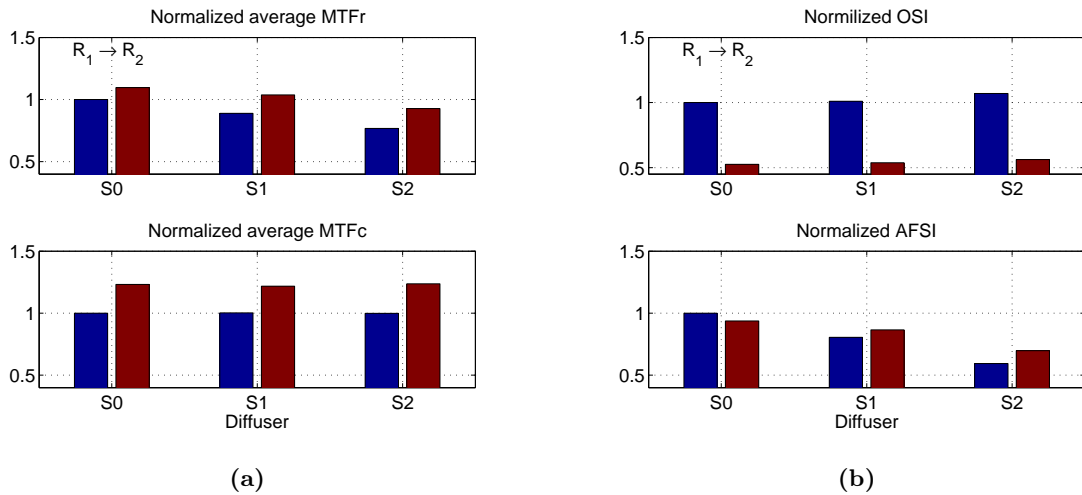


**Figure 5.9:** Bar plots indicating the average value of the raw (a, top) and corrected (a, bottom) MTF and the amount of scattering quantified through the OSI (b, top) and the AFSI (b, bottom). The data is presented for different amount of scattering induced with diffusers  $S_0$  (left bars),  $S_1$  (middle bars), and  $S_2$  (right bars) and with ocular fundus  $R_1$  (blue bar) and  $R_2$  (red bar), respectively.

Table 5.2 shows the values of both the OSI and AFSI computed over the recorded images for the different amounts of scattering induced in both the pupil and the fundus plane. The tendency observed in the data suggests that the AFSI can be used to detect differences in

the intraocular scattering contained in double-pass images. Compared with the information presented in table 5.1, the values of AFSI approaches each other for the same diffusers, despite of the presence of aberrations or changes in the characteristics of the fundus during measurements. Therefore, the AFSI may contain relevant information on intraocular scattering and could be used to detect variations of this phenomenon in real situations.

**Table 5.2:** Values of OSI and AFSI computed for the different combinations of diffusers ( $S_0$ ,  $S_1$ , and  $S_2$ ) and ocular fundus ( $R_0$  and  $R_1$ ). The mean value and standard deviation of the OSI and AFSI per diffuser is also presented in the table.

Lens	OSI			AFSI		
	$S_0$	$S_1$	$S_2$	$S_0$	$S_1$	$S_2$
$R_1$	1.000	1.001	1.070	1.000	0.806	0.595
$R_2$	0.525	0.537	0.562	0.937	0.865	0.698
Mean	0.762	0.773	0.816	0.969	0.835	0.646
std	0.336	0.334	0.359	0.044	0.042	0.073

## 5.5 Application of the AFSI in human eyes

The AFSI was computed for double-pass images of 19 real healthy eyes. 14 of these measurements correspond to those described in chapter 4, section 1.3 during the estimation of the scattering properties of the ocular fundus. All the measured cases correspond to eyes that in principle do not present intraocular scattering. Therefore, the results presented here may be considered as a starting point for the characterization of the index in scattering classification, in the sense that the computed values of AFSI corresponds to data for healthy eyes.

Following the experimental procedure described in the previous chapter, 5 series of 20 double-pass and Hartmann-Shack images were available for the right eye of the 19 measured subjects. The average double-pass image per series was then used to compute the raw ( $MTF_r$ ) and corrected ( $MTF_c$ ) modulation transfer function following the procedure described in figure 5.5. Therefore, the images were considered to quantify the scattering through the OSI and the AFSI. In the case of Hartmann-Shack images, the average of the 20 recorded frames was used to describe the wave aberrations using 54 Zernike coefficients. We use the RMS value of these coefficients normalized to the working wavelength ( $Z/\lambda$ ) as a descriptor of the eye's aberrations. At the end of this procedure 5 estimates for the  $MTF_r$ ,  $MTF_c$ , OSI, AFSI, and  $Z/\lambda$  were available per subject. The average of the 5 estimates were obtained to provide a

single value per estimator and subject.

Figure 5.10 shows the behavior of the AFSI and the OSI for the 19 real healthy eyes measured. It results difficult to make a direct comparison between the indices because, among other factors, they present different dynamic ranges to quantify the same phenomenon. While the OSI provides a number between 0 and 25 [10], the AFSI works between 1 and 0. We expect smaller increases in the AFSI for the same changes in scattering. Since it remained below 1 for all the cases, the computed values of OSI corroborate the assumption that measurements were performed for healthy eyes [10]. The tendency line included in the figure indicates that these two indices are inversely proportional, which was expected from the fact that, contrary to the behavior of the OSI, the AFSI decreases with increasing levels of scattering. There is some dispersion of the data around the tendency line. This is maybe provoked by differences in the manner in which aberrations and changes of the scattering from the fundus affects the indices.

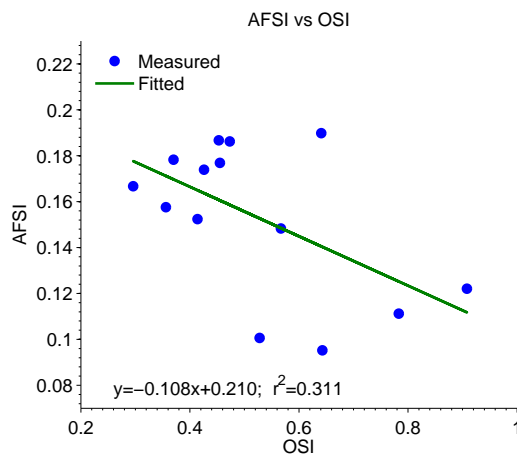


**Figure 5.10:** AFSI in function of the OSI for the 19 measured eyes. The tendency line fitting the data, its equation, and the coefficient of determination are included in the figure.

The performance of both the OSI and the AFSI as a function of aberrations are plotted in figure 5.11. From the dispersion of the data, we cannot say that the tendency line in the plots describes well the measured eyes. However, it is interesting to note that the most aberrated case ( $Z/\lambda = 0.248$ ) presents one of the maximum values of OSI (0.908). Contrary, the AFSI for this case (0.158) is close to the tendency line, around the middle of the range of the measured eyes. Therefore, the amount of aberrations in that case could influence the computation of the OSI, without implying an increase of scattering in the double-pass images. However, the value of OSI stills corresponds to a healthy eye.

The values of  $Z/\lambda$ , OSI, and AFSI are presented in table 5.3. The average value for the

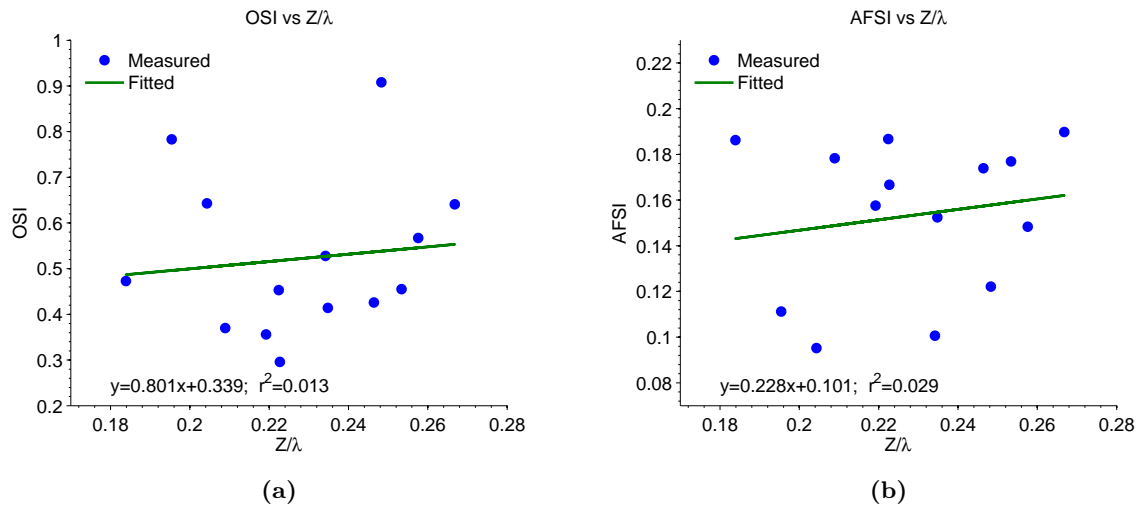


**Figure 5.11:** OSI (a) and AFSI (b) in function of the normalized RMS value of the Zernike coefficients  $Z/\lambda$  for the 19 measured eyes. The tendency lines fitting the data, its equations, and the coefficients of determination are included in the plots.

AFSI indicates that healthy eyes should present values around  $0.158 \pm 0.071$ . We expect that increased levels of scattering would be reflected as a reduction of the index. Thus, the dynamic range of the AFSI for real eyes could be limited between 0 and 0.150. In this sense, a further characterization is necessary on eyes with different amounts of scattering to define ranges for healthy eyes and those presenting deviations due to the presence of cataracts.

**Table 5.3:** Normalized RMS value of Zernike coefficients  $Z/\lambda$ , OSI, and AFSI for the left eye of the 19 subjects.

Case	Label	$Z/\lambda$	OSI	AFSI
1	CC	0.234	0.528	0.101
2	MK	0.235	0.414	0.152
3	FA	0.258	0.567	0.148
4	XN	0.204	0.643	0.095
5	CY	0.222	0.453	0.187
6	DN	0.223	0.296	0.167
7	JO	0.209	0.370	0.178
8	MX	0.268	0.539	0.176
9	BR	0.219	0.356	0.158
10	ST	0.184	0.473	0.186
11	AS	0.246	0.426	0.174
12	SE	0.248	0.908	0.122
13	MI	0.251	0.399	0.158
14	IC	0.253	0.455	0.177
15	SL	0.267	0.641	0.190
16	FS	0.205	0.593	0.165
17	EM	0.195	0.783	0.111
18	JA	0.288	0.896	0.158
19	CE	0.211	0.464	0.197
Average	AV	0.233	0.537	0.158
Std	SD	0.027	0.173	0.071

## 5.6 Conclusions

In this chapter, we have introduced the AFSI, the aberration-free scatter index. This scattering quantifier is based on the analysis of the double-pass MTF before and after peak correction. Measurements on an artificial eye suggests that the index can be used to detect changes provoked by intraocular scattering. The AFSI results less affected by the presence of aberrations than the OSI, which is an index based on the analysis of the double-pass PSF used in clinical systems. In this sense, the method for quantifying scattering proposed here could improve the classification of cataract patients in real eyes under the presence of refractive errors. In addition, it was still possible to detect changes in the scattering arising at the pupil plane for ocular fundus having different diffusion characteristics. This situation is relevant in

systems working with infrared light. In this kind of systems, the light may penetrate until the choroid, increasing the amount of scattered light in the double-pass images. Measurements on real eyes indicate that the AFSI may present values around 0.150 for healthy eyes. The analysis of images with different intraocular scattering could be used to define the values of AFSI for different conditions. Like the OSI, the AFSI may be affected by corneal reflections or residual light coming from internal reflections of the measuring instrument. However, we suggest that the index proposed here can be used in real situations to classify eyes with different levels of intraocular scattering.



## Chapter 6

# Speckle reduction in double-pass images using focus-tunable lenses

During the determination of the optical quality with double-pass (DP) instruments, the aerial image of a coherent point source projected on the retina after double-pass of light through the ocular media is analyzed [20]. In this context, the retina can be considered as an optically rough surface composed of photoreceptors that scatter light back with a random phase [100]. Therefore, DP images are affected by speckle because they rely on reflection of coherent light in a diffusing material [20].

In visual optics, speckle is treated as a noise affecting the images that are used to evaluate the optical quality of the eye. In this sense, estimations from speckled images would contain not only information of the optics of the eye, but also the influence of coherence during image recording [20]. In consequence, speckle reduction results of crucial importance to provide accurate estimations of the optical quality when the eye is evaluated with systems based on retina reflections, such as double-pass and Hartmann-Shack [22] instruments.

Speckle reduction is achieved if we add in an intensity basis a number of uncorrelated speckle patterns, which can be generated by time, space, or polarization diversity [94]. Taking advantage of the time-variant behavior of the speckle structure in the eye due to microfluctuation of accommodation and the presence of dead cells in the vitreous humor, the first methods for reducing this noise in double-pass systems were based on time diversity by taking long-exposure images and averaging a number of consecutive short-exposure frames [20]. Space diversity has also been implemented in visual optics to reduce speckle by deviating rays reaching the retina with scanning mirrors [9], rotating diffusers [38], and acoustic modulators [96]. Although

---

with inconclusive results, there have been also some attempts to reduce speckle with the space diversity produced by broadband lasers<sup>1</sup> [9].

As an alternative method for speckle reduction, we propose to vary the vergence of light entering the eye to produce uncorrelated speckle patterns during image recording. These variations are generated with a spherical refractive error corrector based on remote-controlled focus-tunable lenses [39, 128] that permits shifting longitudinally the focal position of light in relation to the retina. Similar to the use of broadband lasers where the decorrelation is partially ruled by the defocus effect of the wavelength bandwidth [101], the proposed method achieves speckle reduction from the space diversity produced by changes in the optical path of reflected light [129]. The effects of this method would be equivalent to those produced in the eye by dioptric power changes with time, but with a controlled amplitude and frequency. Although the implementation of the method modifies the performance of the measuring instrument, the determination of the optical quality is not compromised as the magnitude of the induced vergence variations is such that the system can still be considered diffraction limited. Similar concepts have been used in other areas of research, as in digital holography [130]. However, to the best of our knowledge the proposed method is its first use in visual optics.

This chapter presents an extended version of the results included in the article "*Speckle reduction in double-pass retinal images using variable-focus lenses*" published in the Journal of the European Optical Society [131]. First, section 6.1 explains the influence of illumination conditions, reflecting surface, and system response in the formation of speckle. Then, the effects on the optical quality as a consequence of the vergence variations on which the method is based are analyzed in section 6.2 from simulations of a model that mimics the configuration used during experimentation. Section 6.3 introduces the experimental platform used during measurements, the method followed during experimentation, and the process performed over recorded images to obtain parameters with information on both speckle and optical quality. The results of measurements on an artificial and two real eyes are presented in section 6.4. Finally, the last part of this chapter gives general conclusions about the method for speckle reduction and its applicability in double-pass systems.

---

<sup>1</sup>As indicated in chapter 3, the MEOQ system uses a light source with a bandwidth of around 20nm. However, this was not enough to reduce speckle in the system in short-exposure images. It means that laser sources of broader spectrum would be necessary to reach the reduction in systems bases on reflections of light in the ocular fundus.

## 6.1 Speckle and its behavior

Speckle arises when coherent light is reflected by optically rough surfaces. The granularity perceived in images affected by this phenomenon is a consequence of the interference between independent randomly phased scatters resulting from the relative delays introduced by the reflecting surface [94]. In systems based on retina reflections, speckle appears as a consequence of the complex, random perturbation of reflected light derived from the microscopic characteristics of the retina, such as foveal cone spacing (correlation length) and optical path differences between one cone and the surrounding media (roughness) [100].

There are a number of parameters that define the characteristics of speckle. Besides the correlation length and roughness of the reflecting surface, it is well known that speckle depends on the illumination conditions [132] and the position of the observation plane [101, 133]. When measured at the image plane, speckle is affected by the response of the imaging system, including defocus [134].

Defined as the ratio of the standard deviation  $\sigma_I$  in the pattern to the average intensity  $\langle I \rangle$ , the speckle contrast  $SC_I = \sigma_I / \langle I \rangle$  is usually used to quantify this phenomenon [94]. Pedersen [4] provides general relations that can be employed to depict the performance of the speckle contrast for different object roughness  $\sigma_\phi$ , illumination conditions  $\beta = (\sigma_h / \sigma_c)^2$ , and normalized defocusing  $\varsigma = z / (k\sigma_h^2)$ . In the latter case,  $z$  and  $k = 2\pi/\lambda$  represent the defocus and the wavenumber, respectively. Regarding  $\beta$ , it accounts for the number of incoherent contributions in a focused image point and depends on the radius of the Gaussian illumination  $\sigma_c$  and the impulse response  $\sigma_h$  of the system. The derivation of the relations is beyond the scope of this work and can be consulted in [4]. However, the behavior of the speckle contrast is depicted in figure 6.1 for complex random objects with circ-function phase correlations  $c_\phi(\xi) = \text{circ}(|\xi|/r_c)$ , where  $\xi$  is the distance between two point in a random surface with correlation lengths  $r_c$ .

Curves in figure 6.1 show that, under certain conditions, the speckle contrast is reduced as a function of the defocus. The magnitude of the reduction depends on both the phase differences imposed by the rough surface and the number of incoherent contributions in the image. Considering that the retina imposes phase differences of  $\sigma_\phi < 0.5\lambda$  [102], we would expect to vary the speckle structure for any value of  $\beta$  by changing the focal position of the system. In the case of a double-pass system with unequal entrance and exit pupils of 2mm and 4mm in diameter, the radius of the illumination (first-pass) is twice that of the impulse

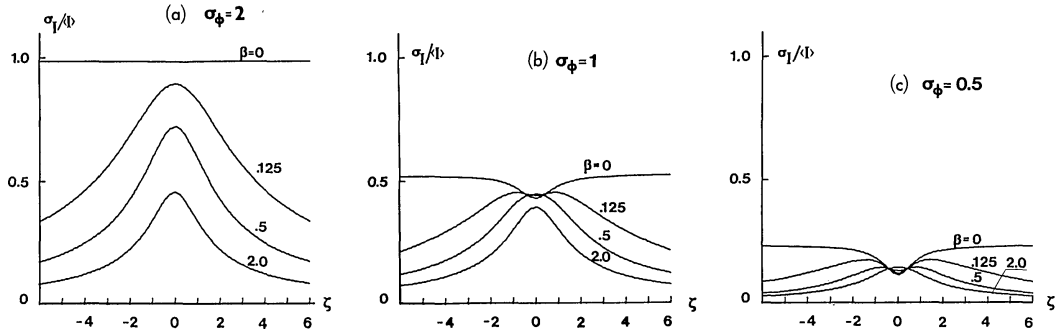


**Figure 6.1:** Speckle contrast as function of defocusing  $\zeta$  for different illumination conditions  $\beta$  and object roughness  $\sigma_\phi$ . Image taken from [4].

response (second-pass) of the system, leading in this manner to a value of  $\beta = 0.5$ .

When double-pass configurations are used to assess the optical quality of the eye we do not have control on the conditions imposed by the retina. However, it is possible to vary the vergence of the beam entering the eye to compensate for the defocus of the eye. Therefore, the results presented here suggest that speckle patterns observed in double-pass images could be modified in function of an induced defocus. If uncorrelated patterns were produced during the integration time of the imaging device, it would be possible to reach a speckle reduction by a combined influence of space and time diversity.

## 6.2 Effects of vergence variations in double-pass response

As explained, we propose to reduce the speckle noise in double-pass instruments by varying the vergence of the beam entering the eye during image recording. However, the performance of the measuring system may be degraded due to the alterations to the instrument transfer function provoked by the induced defocus. Despite these variations, the system must be able to provide representative estimations on the eye's optical quality. In this regard, the effects that vergence variations impose to the system performance are treated here. This information is used to define the range for the magnitude of variation within which the system operates under a diffraction limited regime. The selected threshold is based on the Marechal criterion for image quality [12] to permit a maximum degradation of 0.2 in terms of the Strehl ratio.

The effects of the proposed method for speckle reduction were estimated based on simulations in Zemax (Zemax Development Corporation, 2013). To do this, vergence variation of different amplitudes were induced in an eye model proposed by Navarro *et al.*[121]. Changes in the light entering the eye were generated by modeling the spherical refractive error corrector used

during the implementation of the method. This variable device is composed by a focus-tunable lens followed by a compensating lens of fixed optical power that shifts the range of correction and keeps the tunable device and the eye in conjugated planes [39]. The parameters of the corrector correspond to those presented later in section 6.3.1 during the description of the experimental platform. The configuration of the simulated system is depicted in figure 6.2.

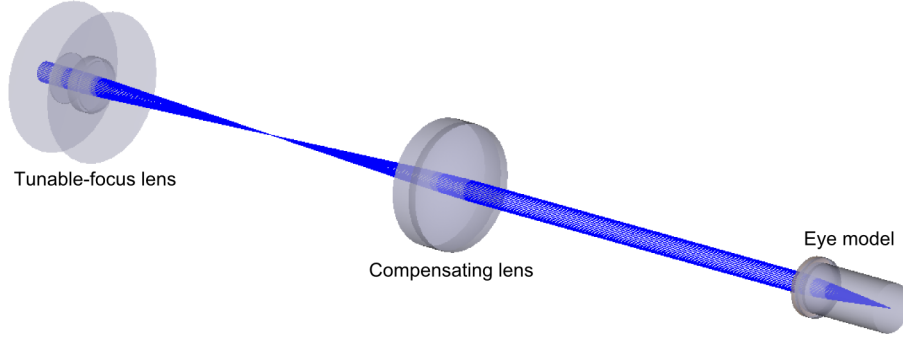


**Figure 6.2:** Zemax model used to simulate the effects of vergence variations in DP response.

The variations induced during image recording were estimated by averaging a number of double-pass point spread functions (PSF) for different values of vergence within the desired range of fluctuations. In this manner, the expected response was computed as the average of 50 estimates for input optical powers of the form  $P = p \sin(2\pi 50/n)$ , where  $n = 1, 2, \dots, 50$  for each of the following values of  $p$ : 0.125, 0.250, 0.500, and 1.000D. Regarding the double-pass response, first the PSF was estimated on the retina of the eye model for pupils of 2 and 4mm in diameter, then the desired curve was computed as  $PSF_{DP} = PSF_{2mm} \otimes PSF_{4mm}$ , where  $\otimes$  denotes convolution. Once calculated as the Fourier transform of the PSF, the modulation transfer function (MTF) was used to estimate the degradation induced by the variations in terms of the Strehl ratio (SC). This last parameter was obtained as the ratio between areas under the MTF [27] of the current case and the system without induced variations.

The PSF for variations of different magnitude is presented in figure 6.3. As observed, the periphery of the curves tends to increase as a function of the variations. This fact is reflected in the MTF as a reduction of its magnitude. The computed curve is the result of changes in the focal position during image recording. In this manner, the overall effects of the induced vergence variations are similar to those produced by defocus. The Strehl ratios in table 6.1 reflects that the simulated system can be considered as diffraction limited when the peak amplitude of the variations remain lower than 0.250D. Therefore, this value was used during the implementation of the method in real scenarios as threshold for the maximum amplitude of induced vergence variations.

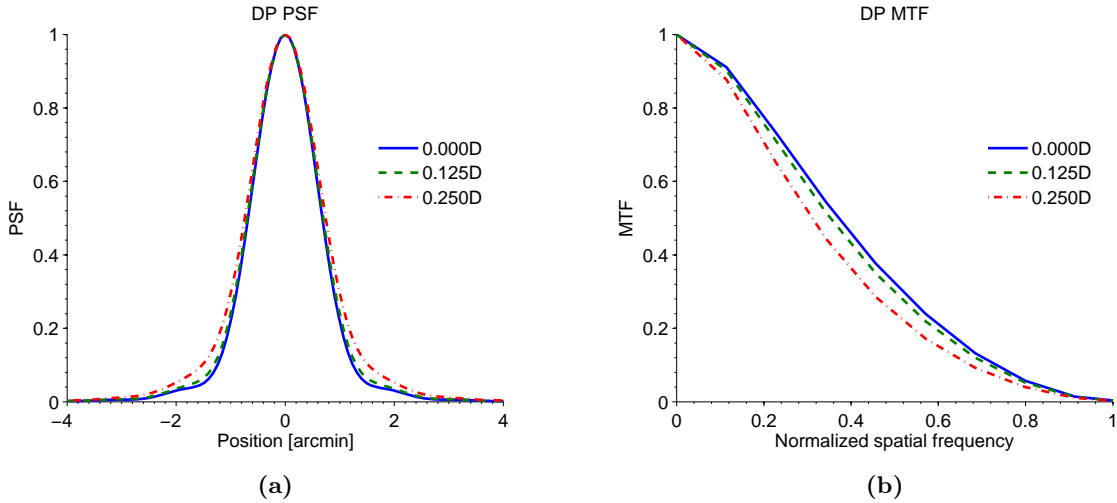


**Figure 6.3:** Double-pass PSF (a) and MTF (b) for vergence variations of different amplitudes. The horizontal axis of the MTF is normalized to the cutoff frequency for a pupil diameter of 2mm.

**Table 6.1:** Strehl ratio (SC) for vergence variations of different amplitudes.

	0.000D	0.125D	0.250D	0.500D	1.000D
SC	1.000	0.964	0.876	0.768	0.727

## 6.3 Materials and methods

The behavior of speckle in double-pass systems and the effects of the vergence variations with which we propose to reduce speckle have been discussed above. In this section, we present the experimental setup and the methodology that was followed to probe the concept in real situations by applying the method for speckle reduction in measurements on both artificial and real eyes.

### 6.3.1 Experimental platform

The double-pass configuration used for the measurements is depicted in figure 6.4. Collimated light from a laser diode (Monocrom MC7805U-M-7A15,  $\lambda = 780\text{nm}$ ) passes through the 2mm diaphragm  $P_1$  before reaching the spherical refractive error corrector composed of the focus-tunable lens  $L_T$  (Optotune EL-10-30-NIR-LD) and the lens of fixed optical power  $L_C$ . The focal distance of  $L_T$  varies from 36 to 132mm, while the one of  $L_C$  is 50mm. The distance between lenses  $L_T$  and  $L_C$  and between  $L_C$  and the pupil plane of the eye is 100mm, twice the focal distance of lens  $L_C$ . As explained by Sanabria et al. in [39], the function of the lens of fixed optical power is to shift the range of correction and to keep the focus-tunable

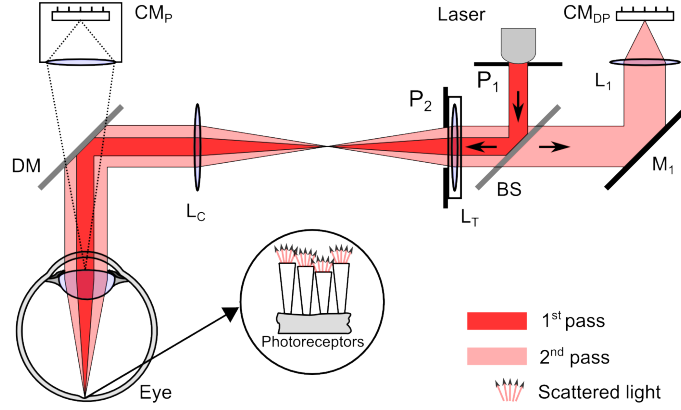


**Figure 6.4:** Scheme of the double-pass system used during the experiments. Pupils:  $P_1$ ,  $P_2$ ; beam splitter:  $BS$ ; focus-tunable lens:  $L_T$ ; lenses:  $L_C$ ,  $L_1$ ; dichroic mirror:  $DM$ ; mirror:  $M_1$ ; cameras:  $CM_{DP}$ ,  $CM_P$ .

lens and the pupil  $P_2$  in a plane conjugated to the pupil of the eye. After being reflected by the dichroic mirror  $DM$  and passing through the optics of the eye, the light is focused on the retina. There, part of the incident light is scattered or re-radiated back towards the pupil by different structures forming the retina [100], thus defining the starting point of the second pass. Following an optical path identical to the first pass, light goes through the 4mm diaphragm  $P_2$  and reaches beam splitter  $BS$ . Afterwards, light is reflected by  $M_1$  towards lens  $L_1$ . Such a lens has a focal distance of 100mm and its function is to focus light on the sensor of camera  $CM_{DP}$ , which records the double-pass images.

The spherical refractive error corrector formed by the lens pair  $L_T - L_C$  was used to generate periodic variations of small amplitude on which the proposed method relies to reach the speckle reduction. The configuration of the corrector allows to set vergences in the beam entering the eye between  $+7.77$  and  $-12.42D$  [39] by varying the current of the tunable device with a sensitivity of  $0.05D/mA$ .  $L_T$  is controlled remotely using a commercially available driver (Optotune Electrical Lens Driver 4) capable of setting sinusoidal signals up to  $\nu_s = 100KHz$ .

The dichroic mirror  $DM$  that is located in front of the eye has a double function: on the one hand, it monitors the eye's position using the camera  $CM_P$ , and on the other, it breaks coherence of light when acting as scanning mirror. For the latter,  $DM$  was mounted on a vibrating motor. The non-speckled images that were obtained with the scanning mirror turned-on were used for comparison purposes during the quantification of the speckle reduction.

### 6.3.2 Experimental procedure

A series of measurements in artificial and real eyes were carried out to corroborate the speckle reduction and the viability of the method. In the first series, the speckle was quantified for vergence variations having different amplitudes in an artificial eye that consisted of a lens with 50mm focal length followed by a cardboard acting as retina. For the real cases, the noise was evaluated for variations of single amplitude in two healthy right-eyes of subjects looking at infinity. While the performance of speckle in function of the induced variations was studied using the artificial eye, the applicability of the method in real scenarios was analyzed from results in real eyes.

Before the measurements, the central optical power  $C_0$  of the spherical refractive error was determined for the eye under assessment. To do so, the current in the focus-tunable lens was varied until finding the double-pass image with the best optical quality with the scanning mirror turned on. Therefore, the task of the experimenter was to search by visual inspection in real time for the image with the narrowest spot. After completing this, the power of the laser source was configured to obtain non-saturated frames with peak intensities higher than 200 of 255 possible gray-level values. Under this configuration, six images denoted as  $I_0$  were recorded with the scanning mirror turned on. Next, six other recordings labeled as  $I_S$  were registered, but with the scanning mirror turned off. In this manner, frames  $I_0$  were considered without speckle and used as reference during the computation of the speckle reduction. On the other hand, frames  $I_S$  refer to full speckle images. After recording  $I_0$  and  $I_S$ , a number of images denoted as  $I_R$  were registered. These images corresponds to those obtained following the implementation of the method with the scanning mirror turned off. Each conjunct of reduced speckle images  $I_R$  were formed by six consecutive recordings, as proceeded for the determination of both the reference and the full speckle cases.

The acquisition of images  $I_0-I_S-I_R$  was performed in a single session for each of the assessed eyes. To generate the vergence variations, we used the functionality of the spherical refractive error corrector that permits setting optical power at different frequencies. In this manner, optical powers in the beam entering the eye of the form  $C = C_0 + c \sin(2\pi\nu_s t)$  were configured, where  $C_0$  and  $c$  are, respectively, the central optical power and the peak amplitude of the variations,  $\nu_s$  is the frequency of the periodic signal, and  $t$  represents time. A frequency  $\nu_s = 50\text{Hz}$  was used during the determination of images  $I_R$ . These variations were produced during the integration time of the imaging device. When data acquisition was requested, six consecutive images were recorded with an integration time of 40ms. This value allowed to

record images that contained the effects of two cycles of the varying signal.

For the artificial eye, two sets of images  $I_R$  were recorded. They correspond to vergence variations of amplitudes  $c = 0.150\text{D}$  and  $0.250\text{D}$ . Since  $c$  is the only difference between image parameters, changes in speckle patterns were related directly to the amplitude of the induced variations. Regarding measurements in real eyes, a single set of images  $I_R$  was recorded for each subject. The amplitude of the variations was set to  $0.250\text{D}$ . Because Strehl ratios higher than  $0.8$  were expected for the induced amplitudes (see section 6.2), it was considered that the system worked in a diffraction limited regime.

Double-pass images were available in real time video through a user interface developed in C++. After measurements, the recorded data were post-processed in Matlab (Mathworks, 2010) following the procedure described later in section 6.3.3 of this chapter.

### 6.3.3 Data processing

During data processing,  $\bar{I}_0$ ,  $\bar{I}_S$ , and  $\bar{I}_R$  were computed as the average of the six frames forming images  $I_0$ ,  $I_S$ , and  $I_R$ , respectively. Next, a series of parameters with information on both speckle and optical quality were obtained from the individual images and the corresponding averages following the flow chart in figure 6.5. In particular, the parameters that were computed correspond to the speckle contrast SC, the double-pass modulation transfer function MTF, the effective cut-off frequency  $\nu_c$ , and the Strehl ratio SR. Of the entire set of images,  $\bar{I}_0$  is considered as the one less affected by speckle because it represents the average of frames recorded with the scanning mirror turned on. For this reason,  $\bar{I}_0$  is used as benchmark and its parameters are taken as reference to quantify deviations produced by speckle.

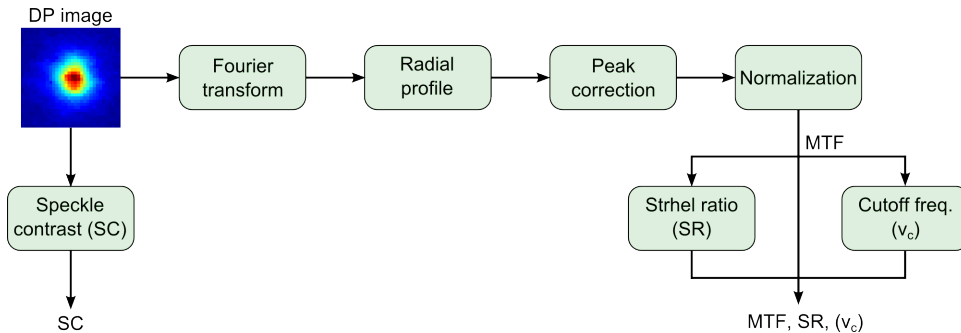


**Figure 6.5:** Flow diagram of the process to determine  $SC$ ,  $MTF$ ,  $\nu_c$ , and  $SR$  from double-pass images.

The granularity provoked by reflection of coherent light in the retina was quantified using the speckle contrast  $SC_I = \sigma_I / \langle I \rangle$  [94]. As mentioned in section 6.1, such a metric is usually used to quantify this phenomenon and is defined as the ratio of the standard deviation  $\sigma$  in

the pattern to the average intensity  $\langle I \rangle$ . Based on the fact that double-pass images contain speckle in small areas, that in diffracted limited cases with circular pupils they present circular symmetry, the SC was computed radially. Before its quantification, the center of mass of the images was estimated. Next, the mean and standard deviation of the intensities were obtained for all pixels whose round distances from the center were equal to  $d$  (in units of pixels). This task was done for integer distances  $d$  from 0 to 16; in this manner the computation covered regions of  $9.13 \times 9.13$  arcmin where the effects of speckle were concentrated. This methodology provided a value for SC in function of integer distances. Then, the mean value of the contrast was computed to provide in a single number for all the contributions of speckle in the image. Differences in SC between images were quantified using the relative error  $e_C = (SC_I - SC_{\bar{I}_0})/SC_{\bar{I}_0}$ , where  $SC_I$  and  $SC_{\bar{I}_0}$  represent the speckle contrast in the current image and that in the average image  $\bar{I}_0$ , respectively.

Regarding the parameters with information on the optical quality, first the radial profile of the MTF was computed and then it was used to obtain  $\nu_c$  and  $SR$ . In this manner, the modulation transfer function was estimated by Fourier transformation of the images. When applied to double-pass images captured with aperture diameters of 2 and 4mm for the first and the second pass response, the Fourier transform represents the product of the MTF for such pupil diameters ( $MTF_{2mm} \times MTF_{4mm}$ ) [13]. The influence of the constant background in the images was compensated by applying a peak correction to the MTF [89]. This procedure consists in substituting the value at zero frequency from a curve fitting using two exponential functions as proposed by Artal and Navarro in [106]. After curve normalization, the cutoff value of  $\nu_c$  was estimated by finding the frequency at which the MTF had a magnitude of 0.01. A normalized value of SR was calculated as the ratio between areas under the MTF [27] of the image and that of the reference case  $\bar{I}_0$ , which was considered as the benchmark.

Deviations produced by the presence of speckle in the images were determined by computing the errors in the parameters relative to those for  $\bar{I}_0$ , the average of the six images forming the reference conjunct  $I_0$ . Thus, we computed relative errors for the MTF ( $e_M(\nu)$ ), the mean value of  $e_M(\nu)$  ( $e_M$ ), the cut-off frequency ( $e_\nu$ ), and the Strehl ratio ( $e_S$ ) for  $I_0$ ,  $I_S$ , and  $I_R$  and the averages  $\bar{I}_0$ ,  $\bar{I}_S$ , and  $\bar{I}_R$ . In all cases, the relatives errors were computed as  $e_X = (X_I - X_{\bar{I}_0})/X_{\bar{I}_0}$ , where  $X$  represents the parameters being calculated.

## 6.4 Results and discussions

The results of the implementation of the method are presented in this section. Data included here was obtained through a series of measurements in an artificial and real eyes following the procedure described above.

### 6.4.1 Speckle reduction in an artificial eye

Measurements on the artificial eye show that there was a speckle reduction in function of vergence variations. Figure 6.6 presents cropped versions ( $9.13 \times 9.13$  arcmin) of double-pass images for induced variations of different amplitudes and conditions of the scanning mirror. Visual inspection of images  $I_R$  (reduced speckle) shows that not only the granularity observed in  $I_S$  (full speckle) was reduced, but also the shape of the spots tends to that of  $I_0$  (reference image) when the optical power of the beam entering the eye is varied during image recording. In overall, the larger the amplitude of the variations, the lower the visual effects of speckle in the images. For instance, the best coincidence between images  $I_R$  and  $I_0$  is found for variations of  $0.250D$  in peak amplitude. Comparing the images, there are no considerable differences between individual frames and average images  $\bar{I}_0$ ,  $\bar{I}_S$ , and  $\bar{I}_R$ . This fact is attributed to the stable behavior of the artificial eye during measurements. Under this assumption, it can be assured that changes in the granularity come from vergence variations and not from modifications of either aberrations conditions or speckle structure in the artificial eye.

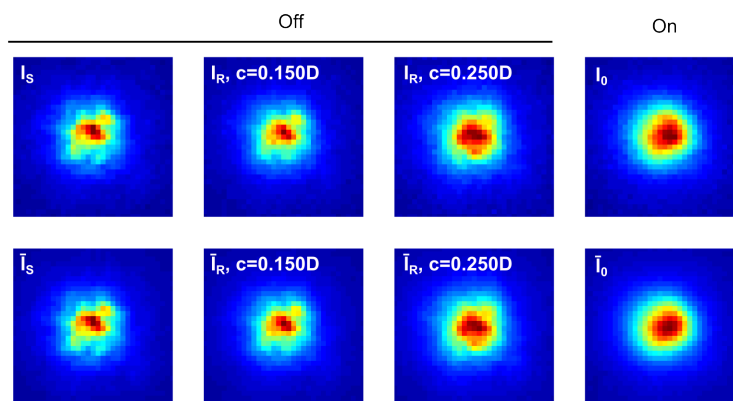


**Figure 6.6:** First recorded ( $I_S$ ,  $I_R$ , and  $I_0$ ; top) and average ( $\bar{I}_S$ ,  $\bar{I}_R$ ,  $\bar{I}_0$ ; bottom) double-pass images for the artificial eye.  $c$  refers to the peak amplitude of the induced vergence variations during image recording. *On* and *Off* indicate states of the scanning mirror.

The computation of the speckle contrast corroborates the noise reduction observed in double-pass images of figure 6.6. The mean value of SC was reduced from 0.202 (0.197) in images

$I_S$  ( $\bar{I}_S$ ) to 0.189 (0.184) and 0.171 (0.167) in images  $I_R$  ( $\bar{I}_R$ ) for vergence variations of 0.150 and 0.250D in peak amplitude, respectively. These values reflect a decreasing trend of the metric towards 0.124 (0.112), which coincides with the average speckle contrast of images  $I_0$  ( $\bar{I}_0$ ). The corresponding values of SC measured for the individual frames represent a shifted version of those computed for the average images. The presence of this shift could indicate small differences between the individual recordings producing deviations with respect to the average. These variations may originate in the sensor noise of the recording device [135] or undesirable vibrations in the system during measurements. This fact could invalidate the assumption of stable behavior of the artificial eye. However, the magnitude of the differences is small and, more important, the decreasing trend is observable in both the images and the averages.

Figure 6.7 presents the double-pass MTF for  $\bar{I}_0$  along with the mean relative error  $e_{MS}$  and  $e_{MR}$  for images  $I_S$  and  $I_R$ , respectively. In the case of reduced speckle images, the errors were obtained for the different induced vergence variations. Thus, the figure contains curves  $e_{MR}$  for  $c = 0.150$  and  $0.250$ D. The relative errors were computed as  $e_{MI} = (MTF_I - MTF_0)/MTF_0$ , where sub-index  $I$  represents the image under assessment. In this manner, the curves are a direct comparison of the MTF with respect to the benchmark case until the cutoff frequency  $\nu_c = 44.75\text{cyc/mm}$  for the first-pass pupil of 2mm in diameter. Referring to the plotted errors, the negative values of  $e_{MS}$  and  $e_{MR}$  indicates a decrease in the MTF at lower frequencies due to the presence of speckle. This behavior is reversed at higher frequencies, where the relative errors go above zero and the MTF shows the highest deviations. Overall, the curves reflect a decreasing behavior in the magnitude of the errors as a function of the induced variations, which is accentuated in the second part of the spectrum. This fact is well observed in  $e_{MR}$ . It represents the mean absolute value of the relative errors for images  $I_R$ , and reached values of 1.094 and 0.837 for vergence variations of amplitudes  $c = 0.150$  and  $0.250$ , respectively.

Despite the magnitude that relative errors reach for images with full speckle, it should be highlighted that the MTF tends to zero around the frequencies with higher affectations. However, it may also indicate that the presence of speckle can affect the computation of the effective cutoff frequency of the assessed eye. Computed as the frequency at which the MTF had a value of 0.01, mean variations were found in terms of the cutoff  $\nu_c$  of 1.221 (1.211) for images with full speckle  $I_S$  ( $\bar{I}_S$ ) and of 1.180 (1.158) and 0.869 (0.864) for vergence variations of  $c = 0.150$  and  $0.250$  in images with reduced speckle  $I_R$  ( $\bar{I}_R$ ). Furthermore, the lower values for images  $I_R$  ( $\bar{I}_R$ ) are closer to the cut-off frequency 0.691 (0.686) obtained for the MTF of the benchmark image  $I_0$  ( $\bar{I}_0$ ), which we consider with lower amount of speckle. Observing

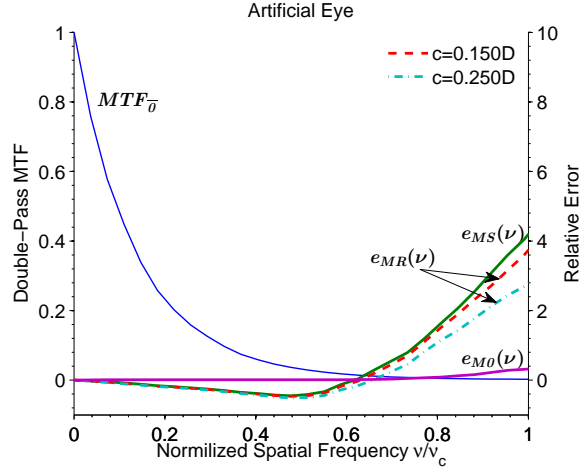


**Figure 6.7:** MTF of the benchmark image  $\bar{I}_0$  (continued narrow line, left axis) and relative errors in the MTF for  $I_0$  ( $e_{M0}(\nu)$ ),  $I_S$  ( $e_{MS}(\nu)$ ), and  $I_R$  ( $e_{MR}(\nu)$ ) (right axis). In the latter case, the curves are presented for three different amplitudes  $c$  of the induced vergence variations.

the tendency of the values, the overestimation of the cut-off frequency is reduced when the method proposed in this work for speckle reduction is applied.

The Strehl ratios show a decreasing tendency in function of the amplitude of the variations. The values of this parameter with respect to that of the reference image ranged from 0.966 (0.960) in image  $I_S$  ( $\bar{I}_S$ ) to 0.952 (0.935) and 0.923 (0.930) in image  $I_R$  ( $\bar{I}_R$ ) for  $c = 0.150$  and 0.250, respectively. Contrary to the performance of all the other parameters, the value of SR deviates from the benchmark in function of the induced variations. This behavior can be inferred from curves in figure 6.7. Errors in images  $I_S$  and  $I_R$  reflect that the MTF suffers a decrease in the lower part of the spectrum, which has the highest impact on the computation of the Strehl ratio. The increase observed in the second part of the spectrum is not enough to compensate for the initial performance, reducing in this manner the SR with respect to the reference. In addition, the overall effect of applying the method for speckle reduction is a kind of defocus, which tends to attenuate the modulation transfer function. However, the Strehl ratio of 0.923 for the worst case computed with respect to the benchmark is still above the Marechal criterion for image quality.

Table 6.2 summarizes the mean relative errors for images  $I_S$ ,  $I_R$ , and  $I_0$ , as well as the relative error for the averages  $\bar{I}_S$ ,  $\bar{I}_R$ , and  $\bar{I}_0$ . Since in the artificial eye the speckle pattern and aberrations were fixed, there are not significant differences in the errors computed from the images or from the averages. Reading data from top to bottom, the errors present a decreasing tendency as a function of the induced defocus, except in those for the Strehl ratio. This behavior implies that the majority of the deviations produced by speckle can be reduced

with the implementation of the method.

**Table 6.2:** Absolute relative errors of the speckle contrast ( $e_C$ ), MTF ( $e_M$ ), cut-off frequency ( $e_\nu$ ), and Strehl ratio ( $e_S$ ) for the full speckle ( $I_S$  and  $\bar{I}_S$ ), reduced speckle ( $I_R$  and  $\bar{I}_R$ ), and reference images ( $I_0$  and  $\bar{I}_0$ ).

	$ e_C $	$ e_M $	$ e_\nu $	$ e_S $
$I_S$	0.804	1.199	0.780	0.034
$I_R _{c=0.15D}$	0.688	1.090	0.720	0.048
$I_R _{c=0.25D}$	0.527	0.837	0.267	0.077
$I_0$	0.107	0.093	0.007	0.012
$\bar{I}_S$	0.759	1.172	0.765	0.040
$\bar{I}_R _{c=0.15D}$	0.643	1.034	0.688	0.067
$\bar{I}_R _{c=0.25D}$	0.491	0.836	0.260	0.070
$\bar{I}_0$	—	—	—	—

### 6.4.2 Speckle reduction in real eyes

In this section measurements in real eyes are presented. The images were recorded following the implementation of the method for speckle reduction for subjects CE and MK. The first recorded and the average images are shown in figure 6.8 for both subjects. As expected from the results on the artificial eye, the granularity observed in the full speckle cases  $I_S$  is visually diminished in images  $I_R$  as a consequence of the spatial diversity produced by the focusing changes during the image recording. This fact is clearer in data for CE, where the speckle is easily distinguished in the individual frame  $I_S$ , but not in  $I_R$  and  $I_0$ . On the other hand, the benefits of time diversity are observed when comparing  $I_S$  and the average  $\bar{I}_S$ ; since in the case of the real eye the speckle pattern changes with time, the averaging of short exposure images resulted in speckle reduction. Although in a lower magnitude, a decreased granularity is reached in images  $\bar{I}_R$  with respect to  $I_R$ . This evidence implies the presence of non-controlled factors leading to a noise reduction during the experiment, such as microfluctuations of accommodation. However, the shape of the spots is always closer to that of the reference cases in images recorded under the influence of vergence variations. In this manner, the observable changes in the speckle pattern in the images are attributed to the application of the method for speckle reduction here proposed.

Quantification of the granularity through the speckle contrast reflects contrary behaviors in the assessed eyes. On the one hand, measurements on CE represent a reduction in this metric

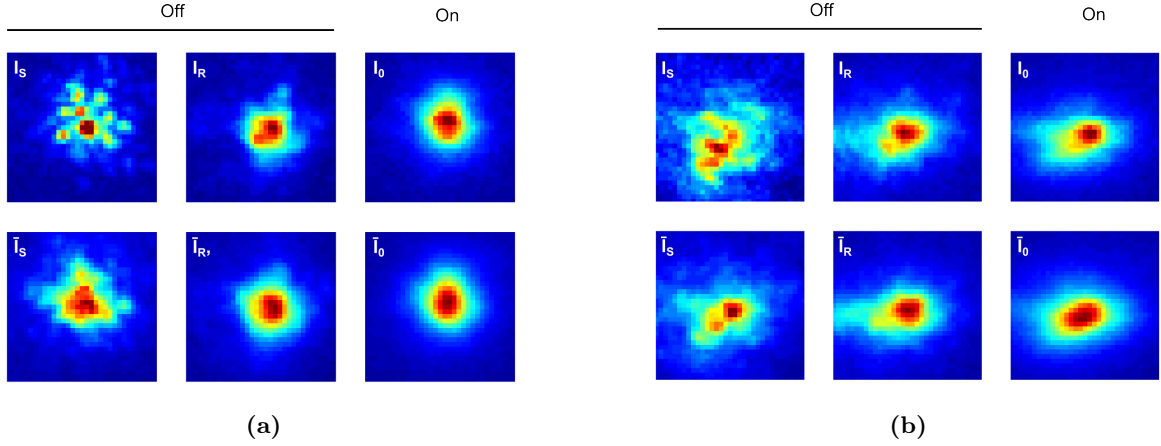


**Figure 6.8:** First recorded ( $I_S$ ,  $I_R$ , and  $I_0$ ; top) and average ( $\bar{I}_S$ ,  $\bar{I}_R$ ,  $\bar{I}_0$ ; bottom) double-pass images for CE (a) and MK (b). *On* and *Off* indicate states of the scanning mirror.

from 0.479 (0.318) in images  $I_S$  ( $\bar{I}_S$ ) to 0.378 (0.283) in images  $I_R$  ( $\bar{I}_R$ ). In this manner, there is a modification in the speckle contrast towards 0.295 (0.282), which corresponds to the value computed in images  $I_0$  ( $\bar{I}_0$ ). On the other hand, quantification of the speckle contrast in recordings on MK reflects a slight increment in the reduced speckle cases. They presented SC values of 0.440 (0.402), a number higher than 0.413 (0.333) and 0.386 (0.377) corresponding respectively to full speckle and reference images. Such contrary behavior can be explained from the spot shapes observed in figure 6.8. Since it is computed radially, radial asymmetries in the images arising from eye aberrations may increase the magnitude of SC, without implying the presence of speckle. Due to its configuration, this fact did not play an important role in the artificial eye. In the case of the real eye, visual inspection of the images with the scanning mirror turned on does not reveal asymmetries that could compromise the computation of the metric in measurements on CE. Therefore, the reduction in the speckle contrast is attributed to the vergence variations. On the contrary, some amount of asymmetries is observed in double-pass images for MK, which may invalidate the quantification of the noise through the used metric.

Following a similar procedure as for the artificial eye, deviations in the MTF were computed using errors relative to the curve for the benchmark image  $\bar{I}_R$ . Figure 6.9 depicts the behavior of the errors for subjects CE and MK. Although at different scales, it can be said that responses present similar performances in both of the assessed eyes. In the first part of the spectrum, the negative values of  $e_{MS}(\nu)$  indicates a decrease in the MTF in images with full speckle. This behavior is less marked in errors  $e_{MR}(\nu)$  obtained from images following the implementation of the method. The decreasing trend is reversed in the second part of the spectrum, where

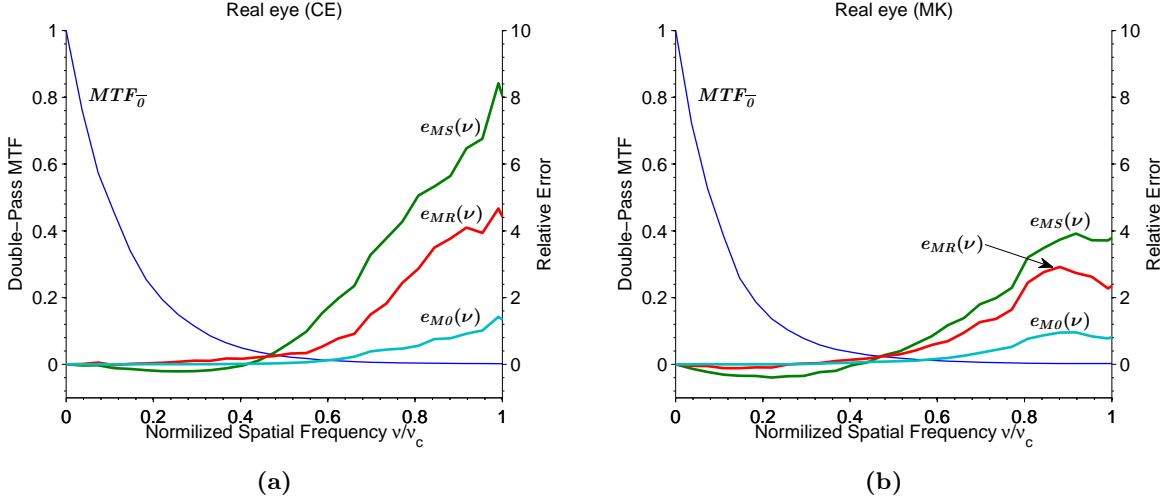


**Figure 6.9:** MTF of the benchmark image  $\bar{I}_0$  (continued narrow line, left axis) and mean relative errors in the MTF for  $I_0$  ( $e_{M0}(\nu)$ ),  $I_S$  ( $e_{MS}(\nu)$ ), and  $I_R$  ( $e_{MR}(\nu)$ ) (right axis) for subjects CE (a) and MK (b).

the errors present positive values and the highest deviations. The differences between  $e_{MS}(\nu)$  and  $e_{MR}(\nu)$  reveal a reduction of the relative error for the measured eyes in images under the effects of vergence variations. The performance of  $e_{M0}(\nu)$  indicates a small deviation of the MTF for images  $I_0$  that is accentuated around the cut-off frequency, which may imply presence of speckle in the images despite the fact that they were recorded with the scanning mirror switched on. These tendencies are well reflected by  $e_{MS}$ ,  $e_{MR}$ , and  $e_{M0}$ . They represent respectively the mean of the absolute value of the relative errors for images  $I_S$ ,  $I_R$ , and  $I_0$  from zero until the cutoff frequency imposed by the first pass pupil diameter of 2mm. The values for the reduced speckle images were 1.966 and 1.451 for subjects CE and MK, respectively, which are lower than 3.119 and 1.934 computed in the full speckle cases and closer to 0.475 and 0.525 obtained for the reference images.

As mentioned in section 6.4.1, the increasing tendency in the errors plotted in figure 6.9 may lead to deviations during the computation of the effective cutoff frequency of the assessed eye. In this sense, mean variations were found in terms of the cutoff frequency  $\nu_c$  for subject CE ranging from 1.350 (0.759) to 1.108 (0.655) for images  $I_S$  ( $\bar{I}_S$ ) and  $I_R$  ( $\bar{I}_R$ ). Moreover, the lower value found for images with reduced speckle are closer to the cutoff frequency 0.673 (0.633) computed for the reference case  $I_0$  ( $\bar{I}_0$ ), which is less affected by speckle. Data computed for subject MK presented a similar behavior. The cutoff frequency computed for the full, reduced, and reference images were 1.083 (0.801), 0.907 (0.685), and 0.669 (0.621), respectively. Therefore, the tendency observed in the results reflect that the computation of the effective cutoff frequency may have benefited by the implementation of the method for

speckle reduction in the sense that deviations from reference data were reduced.

The computation of the Strehl ratio relative to that of image  $\bar{I}_0$  did not reveal a clear tendency in the results. The mean relative SR for images  $I_S$  and  $I_R$  were, respectively, 1.021 and 1.107 for CE and 0.900 and 1.101 for MK; there is an increment in the Strehl ratio in function of the induced variations and the values represent curves with areas higher than that of the benchmark  $\bar{I}_0$ . This behavior is opposed to that found in the artificial eye, where SC was decremented. The errors  $e_{MR}(\nu)$  and  $e_{MS}(\nu)$  plotted in figure 6.9 suffers a decrement in the part of the spectrum with the highest impact in the computation of the Strehl ratio. Then, the relative errors have such magnitude at the higher part of the spectrum for the real eye that the areas under the MTF experimented an overall increment with respect to the area for the reference image  $\bar{I}_0$ , leading to relative Strehl ratios above one. A possible explanation for the increase of the Strehl ratio in the first half of the spectrum for images  $I_R$  is related to a possible defocus during the recording of images  $I_0$ . It is possible to improve the MTF of a defocused lens by introducing certain amount of longitudinal vibrations [136]. If it was the case, the vergence variations during the recording improved the optical quality of the eye, which is quantified as an increase of the Strehl ratio.

Table 6.3 summarizes the mean relative errors for images  $I_S$ ,  $I_R$ , and  $I_0$ , as well as the relative error for averages  $\bar{I}_S$ ,  $\bar{I}_R$ , and  $\bar{I}_0$ . Since real eyes present speckle patterns varying with time, errors for the average images present lower magnitudes. Discarding the Strehl ratio and the speckle contrast for subject MK based on the discussion presented before, the tendency in the errors indicates that the implementation of the method produced a speckle reduction.

**Table 6.3:** Absolute relative errors of the speckle contrast ( $e_C$ ), MTF ( $e_M$ ), cut-off frequency ( $e_\nu$ ), and Strehl ratio ( $e_S$ ) for the full speckle ( $I_S$  and  $\bar{I}_S$ ), reduced speckle ( $I_R$  and  $\bar{I}_R$ ), and reference images ( $I_0$  and  $\bar{I}_0$ ).

	CE				MK			
	$ e_C $	$ e_M $	$ e_\nu $	$ e_S $	$ e_C $	$ e_M $	$ e_\nu $	$ e_S $
$I_S$	0.703	3.119	1.134	0.021	0.095	1.934	0.743	0.100
$I_R$	0.341	1.966	0.751	0.107	0.112	1.451	0.460	0.067
$I_0$	0.049	0.475	0.064	0.032	0.023	0.523	0.076	0.035
$\bar{I}_S$	0.129	0.820	0.200	0.066	0.082	1.040	0.289	0.046
$\bar{I}_R$	0.004	0.623	0.035	0.003	0.066	0.542	0.103	0.022
$\bar{I}_0$	—	—	—	—	—	—	—	—

## 6.5 Conclusions

The results on both, the artificial and real eyes confirmed that speckle can be reduced in double-pass images by inducing periodic defocus of small magnitudes with a variable-focusing lens. Assuming that aberrations and speckle patterns were fixed during measurement on the artificial eye, a reduction in the majority of the computed parameters was found depending on the amplitude of the vergence variations. Moreover, data on real eyes suggest that this method for speckle reduction can be applied in real conditions. The variety of focal positions induced in this method during image recording is to some extent similar to that obtained for the different frequency components of broadband lasers, but produced with a lower cost. Compared to the use of scanning mirrors mounted on vibrating motors, the proposed technique does not produce mechanical vibrations that can be perceived by the subject and, with the time, misalign the optical components of the measuring system. The decreasing trends were observed for the artificial and the real eye. These results suggest that this method can be used in double-pass systems measuring the optical quality of the eye, since changes in focus did not compromise the optical characterization of the eye when they are lower than the 0.25 D peak. It is necessary to study the effects of the vergence variations in the resultant spot position to know if the method is applicable to Hartmann-Shack systems. Although the granularity in the images was reduced, it was not completely suppressed. To increase the magnitude of the reduction, more uncorrelated speckle patterns should be generated by either increasing the amplitude of the vergence variations or by extending the image recording time. To deal with the reduction in image quality arising from the overall effects of the method, the resultant defocus could be compensated during data processing by numerical focusing as done in digital holography [130]. However, further research is needed to check the applicability of these methods.

## Chapter 7

# General conclusions and future work

As stated during the introduction in chapter 1, this dissertation summarizes the MEOQ project, which had as its main objective the implementation of a binocular open-view system based on the double-pass and the Hartmann-Shack techniques for the optical characterization of the eye. The last chapters have presented the work done during the development of the project, including the design of the system and the results of measurements performed with the implemented instrument. This chapter summarizes the more significant conclusions of this work and presents a series of proposals for future work that can be performed with the MEOQ system.

### 7.1 Conclusions

#### **Implementation of a system based on multiple techniques**

A system based on multiple techniques (multimodal system) was designed and implemented. The final design integrates a double-pass instrument and an Hartmann-Shack wavefront sensor to assess the optical quality of the eye. The system is binocular and measures patients in normal viewing conditions through an open field configuration. Moreover, astigmatic and spherical refractive errors are corrected during measurements using devices of configurable optical powers. Instead of element duplication, the system assesses both eyes using single elements along the majority of the optical path. For instance, a single light source and Hartmann-Shack camera are employed to deliver light and to record information of both eyes simultaneously. Since the left and right eyes may present different performances, the MEOQ system integrates a refractive error corrector per eye. Measurements carried out during the

calibration process suggest that the system is able to provide comparable double-pass and Hartmann-Shack estimations when scattering is not present in the process.

During measurements, the most important issue to obtain comparable data is related to the alignment of the optical axis of the eye with that of the system. The parameters that can be controlled in the MEOQ system are the interpupillary distance and the orientation of the light reaching the eye, done by controlling the position of a pair of hot mirrors placed in front of the eye. When measuring, the task of the experimenter consists of bringing the patient to the right position with respect to the system. This process becomes more restricted in the case of binocular measurements. In this sense, this aspect represents the main disadvantage of the current version of the system. However, once the correct alignment is reached, the rest of the processes are practically automatized and can be easily performed through the user interfaces specially developed for the MEOQ system.

### **Quantification of scattering in the ocular fundus**

Due to the nature of the techniques that make up the MEOQ system, it can be used to quantify scattering in the human eye. For this purpose, two models were developed to account for the differences between double-pass and Hartmann-Shack data. In particular, a conventional data processing method was used to obtain the MTF curves from both techniques. The differences between responses are used in the first model to provide the parameters of an equivalent diffuser that would produce similar effects as those measured. The second model is used to provide an estimation of the lateral light spreading produced by scattering. The selection of healthy young subjects permitted the attribution of the differences to phenomena occurring in the ocular fundus. The results suggest that this type of scattering may explain some of the differences between double-pass and Hartmann-Shack responses and that it may be a source of deviation between subjects in double-pass data using infrared light.

The computation of the parameters defining the models was possible because the MEOQ system is able to provide comparable estimations between techniques. In this sense, it would not be possible to perform this analysis in independent systems using measurements at different time instants due to the dynamic behavior of the eye. The analysis assumed that no intraocular scattering was present during measurements. However, the computation of the parameters took into account all the scattering affecting the double-pass data after peak correction, which may contain diffusion appearing in other structures of the eye. In this sense, a further analysis is necessary in subjects under a variety of conditions, such as with the presence of cataracts

in the eye lens.

### **Quantification of intraocular scattering**

An index for scattering quantification was proposed in this work. We have called this Aberration-Free Scatter Index (AFSI). The index quantifies scattering using the information contained in the lower part of the MTF that is usually eliminated during the analysis of double-pass images through the peak correction process. The advantage of this method relies in the fact that it can be applied directly over double-pass images. That is, without comparison with data from other techniques, such as Hartmann-Shack estimations. Data on an artificial eye suggests that the AFSI is not affected by the presence of aberrations in the eye during measurements, which is advantageous when determining scattering in subjects suffering considerably amounts of higher order aberrations that are usually not corrected during the assessment of the eye. Data for different amounts of induced intraocular scattering suggests that the information in the MTF after peak correction lost the majority of the effects produced by this phenomenon in the eye lens. In this manner, variations in the MTF after peak correction may be mainly affected by scattering from the ocular fundus.

The AFSI was able to detect intraocular scattering in an artificial eye. However, we cannot assure that the characteristics of the diffusers used during the experiments are representative of that in real eyes with cataracts. The same situation applied to the diffusers used as ocular fundus. The optical characteristics of the patients that participated in the study did not allow us to obtain conclusive results on the applicability of the methods for cataract classification. Since the measurements were performed on healthy young eyes, the amount of diffusion was expected to be small. The index has to be applied onto subjects with classified cataracts in order to find a relationship between the amount of diffusion in the eye and the index provided by the proposed quantification method. Nevertheless, the work presented here can be used as an starting point for the application of the AFSI into real situations for future studies.

### **Speckle reduction using focus-tunable lenses**

A method for speckle reduction in systems based on reflection of light in the retina was presented in this work. The method consisted in generating periodic changes in the optical power of the beam entering the eye during image recording. These variations in dioptric power generate uncorrelated patterns that can be used to reach speckle reduction. To some

extent, the effects of this method could be seen as those produced by microfluctuations of accommodation happening in the eye, but with controlled amplitude and frequency. Following the implementation of the method, it was possible to reduce speckle in double-pass images in measurements using both an artificial and real eyes.

Although the speckle was reduced, it was not possible to reach a complete suppression of this noise using the proposed method. Changes in the vergence of higher amplitudes should be explored to increase the reduction. The impact on the optical quality of the measuring systems was small in terms of Strehl ratio. If the amplitude is increased, the decrease in Strehl ratio should be considered. Since the overall effects of the method are similar to the ones produced by defocus, the effects of the method they could be compensated during data processing. However, a further analysis has to be performed in this area.

## 7.2 Future Work

The binocular open-field configuration makes it possible to use of the MEOQ system to study accommodation and the correlation in the response between eyes. Moreover, the information of the Hartmann-Shack would allow the analysis of pupillary dynamics. However, it would be necessary to automatize the manner in which the orientation of the optical axis is modified in the system. At present, it is done manually. A series of rotating motors could be incorporated to control the orientation of the hot mirrors that direct the light to the eye.

The current version of the MEOQ system uses a double-pass configuration with unequal pupils of fixed diameters. The use of configurable pupil diameters would allow the determination of the impact of aberrations with respect to the aperture sizes. Moreover, pupils of larger diameters would permit the estimation of parameters of structures forming the eye. Presently, the information is limited by the small pupil size of the first-pass pupil. However, the pupils could be increased until a diameter is reached that allows obtaining information on the spacing between photoreceptors at the fovea by analyzing short exposure images using speckle interferometry [102]. In this manner, the information on the optical quality may be complemented with data on the structures of the eye.

The use of the Hartmann-Shack sensor is limited to the determination of wave aberrations in the implemented system. The scattering quantification performed by the combined data analysis of double-pass and Hartmann-Shack data could be complemented by the analysis of the data contained in the images of the wavefront sensor. In addition to the overall estimates

provided by the MEOQ system, the individual analysis of spots could be used to give spatially resolved estimates for the effects of scattering, as done in [57]. Moreover, the analysis of spot intensities may be used as an estimator of the directionality of retina reflections [95]. This information could be considered during measurements using pupils of larger diameters.

In summary, the MEOQ system can be used to understand the origin of the differences between double-pass and Hartmann-Shack data. This knowledge can be used to estimate the properties of structures involved in the process, such as the scattering that appears in the ocular fundus. The MEOQ system has a series of potentials in the study of the eye in a variety of conditions, such as the assessment of the optical quality in subjects with cataracts or dry eye.



# Appendix A

## Image formation in double-pass systems

Referring to the first-pass geometry of figure A.1a, suppose that an object  $U(x, y)$  located at an object distance  $s$  is imaged behind the lens at an image distance  $s'$ . We represent the first-pass exit pupil as  $P_1(\xi_1, \eta_1)$  and the image amplitude as  $U'(x', y')$ , which would be located on the retina in the case of the eye. The wave aberration  $W_1(\xi_1, \eta_1)$  accounts for path length errors between the wavefront leaving the system and an ideal spherical wavefront at the exit pupil plane. The image formation process of the second pass has an equivalent behavior as that of the first pass<sup>1</sup> and is depicted in figure A.1b. In this case, light coming from  $U'$  passes through the exit pupil  $P_2$  at plane  $(\xi_2, \eta_2)$  with a wave aberration  $W_2$  before being imaged on plane  $(x'', y'')$  to form the amplitude field  $U''$ . The purpose of this section is to analyze the image formation in double-pass systems.

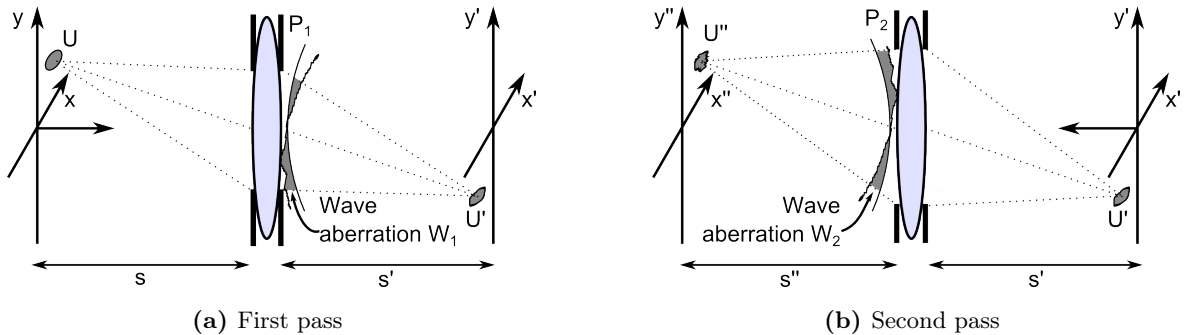


**Figure A.1:** Image formation in the double-pass process.

<sup>1</sup>It is assumed that the first and second passages can be separated when analyzing double-pass systems for measuring the eye, as done by Artal *et al.* in [13]

From the fact that the optical properties of an image system are completely defined by its impulse response [16], we can express the amplitude fields  $U'$  and  $U''$  by the following superposition integrals,

$$U'(x', y') = \iint_{-\infty}^{\infty} h(x', y'; x, y) U(x, y) dx dy \quad (\text{A.1})$$

$$U''(x'', y'') = \iint_{-\infty}^{\infty} h(x'', y''; x', y') U'(x', y') dx' dy' \quad (\text{A.2})$$

where the terms  $h(x', y'; x, y)$  and  $h(x'', y''; x', y')$  represent the first-pass and second-pass amplitude point-spread functions of the system and contain the effects of the pupil and wave aberration at the exit pupil plane of the respective passage. We can write these amplitude point-spread functions as

$$\begin{aligned} h(x', y'; x, y) &\approx \frac{1}{\lambda^2 s s'} \iint P_1(\xi_1, \eta_1) \exp\{jkW(\xi_1, \eta_1)\} \times \\ &\quad \times \exp\left\{-j\frac{k}{s'}[(x' + mx)\xi_1 + (y' + my)\eta_1]\right\} d\xi_1 d\eta_1 \quad (\text{A.3}) \\ &= h_{P1}(x' + mx, y' + my) \end{aligned}$$

$$\begin{aligned} h(x'', y''; x', y') &\approx \frac{1}{\lambda^2 s s'} \iint P_2(\xi_2, \eta_2) \exp\{-jkW(\xi_2, \eta_2)\} \times \\ &\quad \times \exp\left\{-j\frac{k}{s}\left[\left(x'' + \frac{1}{m}x'\right)\xi_2 + \left(y'' + \frac{1}{m}y'\right)\eta_2\right]\right\} d\xi_2 d\eta_2 \quad (\text{A.4}) \\ &= h_{P2}^*\left(x'' + \frac{1}{m}x', y'' + \frac{1}{m}y'\right) \end{aligned}$$

with  $m = |s'/s|$ ,  $k = 2\pi/\lambda$ , and  $\lambda$  representing, respectively, the modulus of the magnification, the wave number, and wavelength of the incident light, while the asterisk \* means complex conjugation.

Considering that wave aberrations are the same for both of the passages, but opposites in sign, the first-pass and second-pass amplitude point-spread functions should be the same [13], except for the extension of the pupil at which they are integrated. Pupils  $P_1$  and  $P_2$  are unity inside and zero outside the projected aperture. Therefore,  $h_{P1}$  and  $h_{P2}^*$  can be expressed in terms of the first-pass amplitude point-spread function  $h$  evaluated at the corresponding pupil, as given by the following equations,

$$\begin{aligned}
 h_{P1}(x' + mx, y' + my) &= h(x' + mx, y' + my)|_{P1} \\
 &= h_1(x' + mx, y' + my)
 \end{aligned}
 \tag{A.5}$$

$$\begin{aligned}
 h_{P2}^*\left(x'' + \frac{1}{m}x', y'' + \frac{1}{m}y'\right) &= h(x' + mx, y' + my)|_{P2} \\
 &= h_2(x' + mx'', y' + my'')
 \end{aligned}
 \tag{A.6}$$

In double-pass systems, a point source (Dirac delta function) is imaged as  $U'(x', y') = h_{P1}(x', y')$  on the fundus. Therefore, the amplitude distribution formed on the fundus is given by the point spread function of the eye. The light that is reflected by the scatter surface is affected by the amplitude reflection factor  $R_i(x', y')$ . After its second pass through the optics of the eye, the light forms the instantaneous (short exposure) amplitude field  $U_i''(x'', y'')$  given by,

$$\begin{aligned}
 U_i''(x'', y'') &= \iint [h_2(x' + mx, y' + my)] \times \\
 &\quad \times [h_1(x', y') R_i(x', y')] dx' dy'
 \end{aligned}
 \tag{A.7}$$

With the additional change of variables  $\bar{x}' = -(1/m)x'$  and  $\bar{y}' = -(1/m)y'$ , equation A.7 takes the form of a convolution integral so that the instantaneous (short exposure) amplitude  $U_i''$  and intensity  $I_i''$  can be expressed as

$$\begin{aligned}
 U_i''(x'', y'') &= m^2 [h_2(mx'', my'')] \otimes \\
 &\quad \otimes [h_1(-mx'', -my'') R_i(-mx'', -my'')]
 \end{aligned}
 \tag{A.8}$$

$$\begin{aligned}
 I_i''(x'', y'') &= |U_i''(x'', y'')|^2 \\
 &= m^4 |h_2(mx'', my'') \otimes \\
 &\quad \otimes h_1(-mx'', -my'') R_i(-mx'', -my'')|^2
 \end{aligned}
 \tag{A.9}$$

$R_i$  is a complex function that stands for the effects of reflections at the first-pass image plane at time  $t = i$ . In the case of the eye, this factor represents the random process happening when light is reflected by the ocular fundus. The speckle pattern observed at double-pass

---

images is in fact provoked by these reflections so that the characteristics of such pattern depend directly on the ones of  $R_i$ . The incoherent double-pass image  $\langle I \rangle$  is obtained by averaging coherent images [13]. Usually, the scattering process in the fundus is considered as  $\delta$ -correlated [13, 117]. Under this assumption, the double-pass intensity can be written as the correlation between the point-spread functions for the first and second pass pupil diameters, as expressed by equation A.10.

$$\begin{aligned}
\langle I \rangle &= I''(x'', y'') \\
&\propto |h_2(mx'', my'')|^2 \otimes |h_1(-mx'', -my'')|^2 \\
&= PSF_2(mx'', my'') \otimes PSF_1(-mx'', -my'')
\end{aligned} \tag{A.10}$$

## Appendix B

# Zernike polynomials

Zernike polynomials are a set of orthogonal (independent) functions that permit to represent the wavefront using terms that can be related to types of aberrations that are usually observed in optical tests [48, 49], such as defocus, astigmatism, among others. Zernike polynomials are defined over the interior of a unit circle and present rotational symmetry every  $2\pi$  radians [48]. In polar coordinates  $(\rho, \theta)$ , the polynomials of radian degree  $n$  and azimuthal frequency  $m$  [137] are defined as

$$Z_n^m(\rho, \theta) = \begin{cases} N_n^m R_n^{|m|}(\rho) \cos(m\theta) & \text{if } m \geq 0 \\ -N_n^m R_n^{|m|}(\rho) \sin(m\theta) & \text{if } m < 0 \end{cases} \quad (\text{B.1})$$

where  $N_n^m$  and  $R_n^m$  are a normalization factor and a radial-dependent component, respectively. These terms are expressed as follows

$$R_n^{|m|}(\rho) = \sum_{s=0}^{(n-|m|)/2} \frac{(-1)^s (n-s)!}{s! [0.5(n+|m|)-s]! [0.5(n-|m|)-s]!} \rho^{n-2s} \quad (\text{B.2})$$

$$N_n^m = \sqrt{\frac{2(n+1)}{1+\delta_m}} \quad (\text{B.3})$$

where  $\delta_m$  is a delta function equal to 1 for  $m = 0$  and 0 for  $m \neq 0$ . Table B.1 shows the expansion of the first 15<sup>th</sup> Zernike polynomials and their meaning with respect the type of aberration being described. The term  $j$  used in the table is related to the mode of the Zernike terms and can be computed as  $j = [n(n+2) + m]/2$ .

**Table B.1:** First 15<sup>th</sup> terms of the Zernike polynomials.

Mode	Order	Frequency	$Z_n^m(\rho, \theta)$	Meaning
j	n	m		
0	0	0	1	Piston
1	1	-1	$2\rho\sin(\theta)$	Tilt in y
2	1	1	$2\rho\cos(\theta)$	Tilt in x
3	2	-2	$\sqrt{6}\rho^2\sin(2\theta)$	Astigmatism at $\pm 45^\circ$
4	2	0	$\sqrt{3}(2\rho^2 - 1)$	Defocus
5	2	2	$\sqrt{6}\rho^2\cos(2\theta)$	Astigmatism at 0 or 90deg
6	3	-3	$\sqrt{8}\rho^3\sin(3\theta)$	
7	3	-1	$\sqrt{8}(3\rho^3 - 2\rho)\sin(\theta)$	Coma in y
8	3	1	$\sqrt{8}(3\rho^3 - 2\rho)\cos(\theta)$	Coma in x
9	3	3	$\sqrt{8}\rho^3\cos(3\theta)$	
10	4	-4	$\sqrt{10}\rho^4\sin(4\theta)$	
11	4	-2	$\sqrt{10}(4\rho^4 - 3\rho^2)\sin(2\theta)$	Secondary astigmatism
12	4	0	$\sqrt{5}(6\rho^4 - 6\rho^2 + 1)$	Spherical aberration
13	4	2	$\sqrt{10}(4\rho^4 - 3\rho^2)\cos(2\theta)$	Secondary astigmatism
14	4	4	$\sqrt{10}\rho^4\cos(4\theta)$	

During wavefront reconstruction, it is necessary to find the coefficients  $C_j$  of the  $Z_j$  modes fitting the RMS wavefront error produced by the optical system under assessment. Once estimated, the coefficients and the Zernike polynomials may be used to reconstruct the wavefront using equation B.4 [49, 50].

$$W(\rho, \theta) = \sum_j C_j Z_j(\rho, \theta) \quad (\text{B.4})$$

# References

- [1] I. J. Hodgkinson, A. C. B. Molteno, and P. B. Greer. Point-spread function for light scattered in the human ocular fundus. *J. Opt. Soc. Am. A*, 11(2):479–486, February 1994.
- [2] H. Ginis, G. M. Pérez, J. M. Bueno, and P. Artal. The wide-angle point spread function of the human eye reconstructed by a new optical method. *Journal of Vision*, 12(3):1–10, March 2012.
- [3] H. S. Ginis, G. M. Pérez, J. M. Bueno, A. Pennos, and P. Artal. Wavelength dependence of the ocular straylight. *IOVS*, 54(5):3702–3708, May 2013.
- [4] H. M. Pedersen. Theory of speckle dependence on surface roughness. *J. Opt. Soc. Am.*, 66(11):1204–1210, November 1976.
- [5] M. Langelaan, M. R. de Boer, R. M. A. van Nispen, B. Wouters, A. C. Moll, and G. H. M. B. van Rens. Impact of Visual Impairment on Quality of Life: A Comparison With Quality of Life in the General Population and With Other Chronic Conditions. *Ophthalmic Epidemiology*, 14(3):116–126, May-June 2007.
- [6] D. A. Atchison and G. Smith. *Optics of the human eye*. Butterworth-Heinemann, 2000.
- [7] N. J. Wade. Image, eye, and retina (invited review). *Vision, color, and visual optics*, 24(5):1229–1249, May 2007.
- [8] W. N. Charman. *Handbook of Optics: Devices, Measurements and Properties*, chapter 24: Optics of the eye, pages 24.3–24.54. McGraw-Hill, 1995.
- [9] H. Hofer, P. Artal, B. Singer, J. L. Aragón, and D. R. Williams. Dynamics of eye’s wave aberrations. *J. Opt. Soc. Am. A*, 18(3):497–506, March 2001.

- [10] P. Artal, A. Benito, G. M. Pérez, E. Alcón, A. de Casas, J. Pujol, and J. M. Marín. An objective scatter index based on double-pass retinal images of a point source to classify cataracts. *PLoS ONE*, 6(2):e16823, February 2011.
- [11] E. Hecht. *Optics*. Addison Wesley, fourth edition, 2002.
- [12] W. J. Smith. *Modern Optical Engineering*. McGraw-Hill, 2000.
- [13] P. Artal, S. Marcos, R. Navarro, and D. R. Williams. Odd aberrations and double-pass measurements of retinal image quality. *J Opt. Soc. Am. A*, 12(2):195–201, February 1995.
- [14] D. P. Piñero, D. Ortiz, and J. L. Alio. Ocular scattering. (review). *Optometry and Vision Science*, 87(9):E682–E696, September 2010.
- [15] F. W. Campbell and R. W. Gubisch. Optical quality of the human eye. *The Journal of Physiology*, 186(3):558–578, March 1966.
- [16] J. W. Goodman. *Introduction to Fourier Optics*. McGraw-Hill, second edition, 1998.
- [17] J. Liang and D. R. Williams. Aberrations and retinal image quality of the normal human eye. *J. Opt. Soc. Am. A*, 14(11):2873–2883, November 1997.
- [18] M. Lombardo and G. Lombardo. Wave aberration of human eyes and new descriptors of image optical quality and visual performance. *Journal of Cataract and Refractive Surgery*, 36(2):313–331, September 2010.
- [19] F. Flamant. Etude de la répartition de lumière dans l' image rétinienne d'une fente. *Rev. Opt.*, 34, 1955.
- [20] J. Santamaría, P. Artal, and L. Bescós. Determination of the point-spread function of human eyes using a hybrid optical-digital method. *J. Opt. Soc. Am. A*, 4(6):1109–1114, June 1987.
- [21] B. C. Platt and R. Shack. History and Principles of Shack-Hartmann Wavefront Sensing. *Journal of Refractive Surgery*, 17(5):573–577, September 2001.
- [22] J. Liang, B. Grimm, S. Goelz, and J. F. Bille. Objective measurement of wave aberrations of the human eye with the use of a Hartmann-Shack wave-front sensor. *J Opt. Soc. Am. A*, 11(7):1949–1957, July 1994.

- [23] J. J. Rozema, D. E. M. Van Dyck, and M.-J. Tassignon. Clinical comparison of 6 aberrometers. Part 1: Technical specifications. *J. Cataract Refract. Surg.*, 31(6):1114–1127, July 2005.
- [24] J. D. Marsack, L. N. Thibos, and R. A. Applegate. Metrics of optical quality derived from wave aberrations predict visual performance. *Journal of Vision*, 4(4):322–328, April 2004.
- [25] P. Artal, M. Ferro, I. Miranda, and R. Navarro. Effects of aging in retinal image quality. *J. Opt. Soc. Am. A*, 10(7):1656–1662, July 1993.
- [26] M. Vilaseca, A. Padilla, J. Pujol, J. C. Ondategui, P. Artal, and J. L. Güell. Optical Quality One Month After Verisyse and Veriflex Phakic IOL Implantation and Zeiss MEL 80 LASIK for Myopia From 5.00 to 16.50 Diopters. *Journal of Refractive Surgery*, 25(8):689–698, August 2009.
- [27] M. Vilaseca, A. Padilla, J. C. Ondategui, M. Arjona, J. L. Güell, and J. Pujol. Effect of laser in situ keratomileusis on vision analyzed using preoperative optical quality. *Journal of Cataract and Refractive Surgery*, 36(11):1945–1953, May 2010.
- [28] J. L. Güell, J. Pujol, M. Arjona, F. Díaz-Doutón, and P. Artal. Optical Quality Analysis System; Instrument for objective clinical evaluation of ocular optical quality. *J. Cataract. Refract. Surg.*, 4(7):1109–1114, July 2004.
- [29] F. Díaz-Doutón, A. Benito, J. Pujol, M. Arjona, J. L. Güell, and P. Artal. Comparison of the Retinal Image Quality with a Hartmann-Shack Wavefront Sensor and a Double-Pass Instrument. *IOVS*, 47(4):1710–1726, April 2006.
- [30] Brien Holden Vision Institute Foundation. Vision Correction Needs. <http://www.brienholdenvision.org>, Accessed in May 2014.
- [31] Transparency Market Research. Ophthalmology Diagnostics and Surgical Devices Market. Global Industry Analysis, Size, Share, Growth, Trends and Forecast, 2013 - 2019. <http://www.transparencymarketresearch.com>, Accessed in May 2014.
- [32] World Health Organization. International Classification of Diseases ICD-10. <http://apps.who.int/classifications/icd10/browse/2010>, Accessed in May 2014.
- [33] World Health Organization. Universal eye health: a global action plan 2014-2019. WHO Library Cataloguing-in-Publication Data, 2013.

- 
- [34] J. N. Mait. A History of Imaging: Revisiting the Past to Chart the Future. *Opt. Photon. News*, 17(2):22–27, February 2006.
- [35] M. Lombardo and G. Lombardo. New methods and techniques for sensing the wave aberrations of human eyes. *Clinical and Experimental Optometry*, 92(3):1444–0938, December 2009.
- [36] X. Cheng, N. L. Himebaugh, P. S. Kollbaum, L. N. Thibos, and A. Bradley. Validation of a clinical Shack-Hartmann aberrometer. *Optometry and Vision Science*, 80(8):587–595, August 2003.
- [37] P. Artal, I. Iglesias, N. López-Gil, and D. G. Green. Double-pass measurements of the retinal-image quality with unequal entrance and exit pupil sizes and the reversibility of the eye’s optical system. *J. Opt. Soc. Am. A*, 12(10):2358–2366, October 1995.
- [38] K. M. Hampson, S.S. Chin, and E. A. H. Mallen. Binocular Shack-Hartmann sensor for the human eye. *Journal of Modern Optics*, 55(4-5):2007, February-March 2008.
- [39] F. Sanàbria, F. Díaz-Doutón, M. Aldaba, and J. Pujol. Spherical refractive correction with an electro-optical liquid lens in a double-pass system. *J. Europ. Opt. Soc. Rap. Public.*, 8(0):13062, September 2013.
- [40] M. Vilaseca, M. J. Romero, M. Arjona, S. O. Luque, J. C. Ondategui, A. Salvador, J. L. Güell, P. Artal, and J. Pujol. Clinical science: Grading nuclear, cortical and posterior subcapsular cataracts using an objective scatter index measured with a double-pass system. *British Journal of Ophthalmology*, 96(9):1204–1210, September 2012.
- [41] J. C. Ondategui, M. Vilaseca, M. Arjona, A. Montasell, G. Cardona, J. L. Güell, and J. Pujol. Optical quality after myopic photorefractive keratectomy and laser in situ keratomileusis: comparison using a double-pass system. *Journal of Cataract and Refractive Surgery*, 38(1):16–27, July 2012.
- [42] P. Artal and R. Navarro. Simultaneous measurement of two-point-spread functions at different locations across the human fovea. *Applied Optics*, 39(19):3646–3656, July 1992.
- [43] A. Guirao and P. Artal. Off-axis monochromatic aberrations estimated from double pass measurements in the human eye. *Vision Research*, 39(2):207–217, April 1999.
- [44] A. Benito, J. M. Pérez, S. Mirabet, M. Vilaseca, J. Pujol, J. M. Marín, and P. Artal. Objective optical assessment of tear-film quality dynamics in normal and mildly symp-

- tomatic dry eyes. *Journal of Cataract and Refractive Surgery*, 37(8):1481–1487, March 2011.
- [45] M. Aldaba, M. Vilaseca, F. Díaz-Doutón, M. Arjona, and J. Pujol. Measuring the accommodative response with a double-pass system: Comparison with the Hartmann-Shack technique. *Vision*, 62(0):26 – 34, April 2012.
- [46] S. Marcos, E. Moreno, and R. Navarro. The depth-of-field of the human eye from objective and subjective measurements. *Vision Research*, 39(12):2039–2049, October 1999.
- [47] G. Yoon. *Adaptive Optics for Vision Science*, chapter 3, pages 63–81. John Wiley and Sons, Inc, 2006.
- [48] J. C. Wyant and K. Creath. *Applied Optics and Optical Engineering*, chapter 1, pages 1–53. Academic Press, 1992.
- [49] J. Y. Wang and D. E. Silva. Wave-front interpretation with Zernike polynomials. *Applied Optics*, 19(9):1510–1518, May 1980.
- [50] P. M. Prieto, F. Vargas-Marín, S. Goelz, and P. Artal. Analysis of the performance of the Hartmann-Shack sensor in the human eye. *J. Opt. Soc. Am. A*, 8(17):1388–1398, August 2000.
- [51] G.-Y. Yoon and D. R. Williams. Visual performance after correcting the monochromatic and chromatic aberrations of the eye. *J. Opt. Soc. Am. A*, 19(2):266–275, February 2002.
- [52] M. A. Lawless and C. Hodge. Wavefront’s role in corneal refractive surgery. *Clinical and Experimental Ophthalmology*, 33(2):199–209, April 2005.
- [53] E. Gamba, L. Sawides, C. Dorronsoro, and S. Marcos. Accommodative lag and fluctuations when optical aberrations are manipulated. *Journal of Vision*, 9(6):1–15, June 2009.
- [54] E. J. Fernández, P. M. Prieto, and P. Artal. Binocular Adaptive Optics Simulator. *Optics Letters*, 34(17):2628–2630, September 2009.
- [55] N. Doble and D. T. Miller. *Adaptive Optics for Vision Science*, chapter 4, pages 83–117. John Wiley and Sons, Inc., 2006.
- [56] E. Moreno-Barriuso, S. Marcos, R. Navarro, and S. A. Burns. Comparing Laser Ray Tracing, Spatially Resolved Refractometer And Hartmann-Shack Sensor To Measure

- The Ocular Wave Aberration. *Optometry and Vision Science*, 78(3):152–156, March 2001.
- [57] J Nam, L. N. Thibos, A. Bradley, N. Himebaugh, and H. Liu. Forward light scatter analysis of the eye in a spatially-resolved double-pass optical system. *Optics Express*, 19(8):7417–7438, April 2011.
- [58] M. J. Cox, D. A. Atchison, and D. H. Scott. Scatter and its implications for the measurement of optical image quality in human eyes. *Optometry and Vision Science*, 80(1):58–68, January 2003.
- [59] R. Navarro and M. A. Losada. Aberrations and Relative Efficiency of Light Pencils in the Living Human Eye. *Optometry and Vision Science*, 74(7):540–547, July 1997.
- [60] E. Moreno-Barriuso and R. Navarro. Laser Ray Tracing versus Hartmann-Shack sensor for measuring optical aberrations in the human eye. *J. Opt. Soc. Am. A*, 17(6):974–985, June 2000.
- [61] M. Mrochen, M. Kaemmerer, P. Mierdel, H.-E. Krinke, and T. Seiler. Principles of Tscherning Aberrometry. *Journal of Refractive Surgery*, 16(5):S570–S571, September 2000.
- [62] M. Kaemmerer, M. Mrochen, P. Mierdel, H.-E. Krinke, and T. Seiler. Clinical Experience With the Tscherning Aberrometer. *Journal of Refractive Surgery*, 16(16):S584–S587, September 2000.
- [63] R. Sekine, K. Ukai, S. Komatsu, M. Hattori, T. Mihashi, N. Nakazawa, and Y. Hirohara. Measurement of wavefront aberrations of human eyes using a 2-dimensional grating and Fourier analysis. In *Frontiers in Optics 2004/Laser Science XXII/Diffractive Optics and Micro-Optics/Optical Fabrication and Testing*, page FWT3, 2004.
- [64] R. Sekine, T. Shibuya, K. Ukai, S. Komatsu, M. Hattori, T. Mihashi, N. Nakazawa, and Y. Hirohara. Measurement of Wavefront Aberration of Human Eye Using Talbot Image of Two-Dimensional Grating. *Optical Review*, 13(4):207–211, April 2006.
- [65] I. Iglesias, R. Ragazzoni, Y. Julien, and P. Artal. Extended source pyramid wavefront-sensor for the human eye. *Optics Express*, 10(9):419–428, May 2002.
- [66] S. Chiesa and J. C. Dainty. Calibration and performance of a pyramid wavefront sensor for the eye. *Journal of Modern Optics*, 59(16):1–13, September 2012.

- [67] E. M. Daly and C. Danity. Ophthalmic wavefront measurements using a versatile pyramid sensor. *Applied Optics*, 49(31):G67–G77, November 2010.
- [68] F. Díaz-Doutón, Pujol, M. Arjona, and S. Luque. Curvature sensor for ocular wavefront measurement. *Optics Letters*, 35(5):2245–2247, August 2006.
- [69] S. Barbero. Wavefront aberration reconstruction from tangential refractive powers measured with spatial dynamic skiascopy. *Applied Optics*, 51(36):8599–8605, December 2012.
- [70] D. Zadok, Y. Levy, O. Segal, Y. Barkana, Y. Morad, and I. Avni. Ocular higher-order aberrations in myopia and skiascopic wavefront repeatability. *Journal of Cataract and Refractive Surgery*, 31(6):1128–1132, June 2005.
- [71] J. Canales, S. Barbero, J. Portilla, and J. M. López-Alonso. Wavefront reconstruction from tangential and sagittal curvature. *Applied Optics*, 53(35):8268–8275, December 2014.
- [72] F. W. Campbell. Correlation of Accommodation between the Two Eyes. *J. Opt. Soc. Am.*, 50(7):738–738, July 1960.
- [73] J. J. Castro, J. R. Jiménez, E. Hita, and C. Ortiz. Differences in interocular differences in the Strehl ratio of binocular summation. *Ophthalmic and Physiological Optics*, 29(3):370–374, December 2008.
- [74] S. Marcos and S. A. Burn. On the symmetry between eyes of wavefront aberration and cone directionality. *Vision Research*, 40(18):2437–2447, August 2000.
- [75] G. Heron, B. Winn, J. R. Pugh, and A. S. Eadies. Twin Channel Infrared Optometer for Recording Binocular Accommodation. *Optometry and Vision Science*, 66(2):123–129, February 1989.
- [76] F. Okuyama, T. Tokoro, and M. Fujieda. Binocular infrared optometer for measuring accommodation in both eyes simultaneously in natural-viewing conditions. *Applied Optics*, 33(22):4147–4154, August 1993.
- [77] S. S. Chin, K. M. Hampson, and E. A. H. Mallen. Binocular correlation of aberration dynamics. *Optics Express*, 16(19):14731–14745, September 2008.
- [78] M. Kobayashi, N. Nakazawa, T. Yamaguchi, T. Otaki, Y. Hirohara, and T. Mihashi. Binocular open-view Shack-Hartmann wavefront sensor with consecutive measurements of near triad and spherical aberration. *Applied Optics*, 47(25):4619, 4626 2008.

- [79] E. Chirre, P. M. Prieto, and P. Artal. Binocular open-view instrument to measure aberrations and pupillary dynamics. *Optics Letters*, 39(16):4773–4775, August 2014.
- [80] L Warden, Y. Liu, P. S. Binder, A. W. Dreher, and L. Sverdrup. Performance of a New Binocular Wavefront Aberrometer Based on a Self Imaging Diffractive Sensor. *Journal of Refractive Surgery*, 24(2):188–196, February 2008.
- [81] C. Schwarz, P. M. Prieto, E. J. Fernández, and P. Artal. Binocular adaptive optics vision analyzer with full control over the complex pupil functions. *Optics Letters*, 36(24):4779–4781, December 2011.
- [82] E. J. Fernández, P. M. Prieto, and P. Artal. Adaptive optics binocular visual simulator to study stereopsis in the presence of aberrations. *J. Opt. Soc. Am. A*, 27(11):A48–A55, November 2010.
- [83] R. Sabesan, L. Zheleznyak, and G. Yoon. Binocular visual performance and summation after correcting higher order aberrations. *Biomedical Optics Express*, 3(12):3176–3789, December 2012.
- [84] D. R. Williams, D. H. Brainard, M. J. McMahon, and R. Navarro. Double-pass and interferometric measures of the optical quality of the eye. *J. Opt. Soc. Am. A*, 11(12):3123–3135, December 1994.
- [85] M. Shahidi and Y. Yang. Measurements of ocular aberrations and light scatter in healthy subjects. *Optometry and Vision Science*, 81(11):853–857, November 2004.
- [86] P. Rodríguez and R. Navarro. Double-pass versus aberrometric modulation transfer function in green light. *Journal of Biomedical Optics*, 12(4):044018, July/August 2007.
- [87] J. M. Bueno, E. Berrio, M. Ozolinsh, and P. Artal. Degree of polatization as an objective method of estimating scattering. *J. Opt. Soc. Am. A*, 21(7):1316–1321, July 2004.
- [88] M. Vinas, C. Dorronsoro, D. Cortes, D. Pascual, and S. Marcos. Longitudinal chromatic aberration of the human eye in the visible and near infrared from wavefront sensing, double-pass and psychophysics. *Biomedical Optics Express*, 23(4):948–962, February 2015.
- [89] A. Guirao, C. González, M. Redondo, E. Geraghty, S. Norrby, and P. Artal. Average Optical Performance of the Human Eye as a Function of Age in a Normal Population. *IOVS*, 40(1):203–213, January 1999.

- 
- [90] P. Beckmann. Scattering by composite rough surfaces. *Proceedings of the IEEE*, 53(8):1012 – 1015, February 1965.
- [91] R. Navarro, J. A. Méndez-Morales, and J. Santamaría. Optical quality of the eye lens surfaces from roughness and diffusion measurements. *J. Opt. Soc. Am. A*, 3(2):228–234, February 1996.
- [92] H. Ginis, O. Sahin, A. Pennos, and P. Artal. Compact optical integration instrument to measure intraocular straylight. *Biomedical Optics Express*, 15(9):3036–3041, September 2014.
- [93] A. V. Larichev, P. V. Ivanov, I. G. Iroshnikov, and V. I. Shmal'gauzen. Measurements of wave aberrations in a speckle field. *Quantum Electronics*, 31(12):1108, 1112 2001.
- [94] J. W. Goodman. Some fundamental properties of speckle. *J. Opt. Soc. Am.*, 66(11):1145–1150, November 1976.
- [95] W. Gao, R. S. Jonnal, B. Cense, O. P. Kocaoglu, Q. Wang, and D. T. Miller. Measuring directionality of the retinal reflection with a Shack-Hartmann wavefront sensor. *Optics Express*, 17(25):23085–23097, December 2009.
- [96] V. Albanis, E. N. Ribak, and Y. Carmon. Reduction of speckles in retinal reflection. *Appl. Phys. Lett.*, 91(5):054104, July 2007.
- [97] E. N. Ribak. Harnessing caustics for wave-front sensing. *Optics Letters*, 26(23):1834–1836, December 2001.
- [98] C. E. García-Guerra, M. Aldaba, M. Arjona, and J. Pujol. Binocular open-view system to perform estimations of aberrations and scattering in the human eye. *Applied Optics*, 54(32):9504–9508, November 2015.
- [99] J. Arines and E. Acosta. Low-cost adaptive astigmatism compensator for improvement of eye fundus camera. *Optics Letters*, 36(21):4164–4166, November 2011.
- [100] S. Marcos, S. Burns, and J. C. He. Model for cone directionality reflectometric measurements based on scattering. *J. Opt. Soc. Am. A*, 8(8):2012–2022, August 1998.
- [101] I. Yamaguchi, A. Yamamoto, and S. Kuwamura. Speckle decorrelation in surface profilometry by wavelength scanning interferometry. *Applied Optics*, 32(28):6721–6728, October 1998.

- [102] S. Marcos and Navarro. Imaging the foveal cones in vivo through ocular speckle interferometry: theory and numerical simulations. *J. Opt. Soc. Am. A*, 13(12):2329–2340, December 1996.
- [103] M. Liu, Z.-K. Wang, Y. Wang, T. Zuo, and Y. Wang. The study of wavelength-dependent wavefront aberrations based on individual eye model. *Optik*, 119(0):383–387, January 2008.
- [104] N. Heussner, L. Holl, T. Nowak, T. Beuth, M. S. Spitzer, and W. Stork. Prediction of temperature and damage in an irradiated human eye—Utilization of a detailed computer model which includes a vectorial blood stream in the choroid. *Computers in Biology and Medicine*, 51(0):35–43, April 2014.
- [105] American National Standard for safe use of lasers. Laser Institute of America ANSI Z136.1 , 2007.
- [106] P. Artal and R. Navarro. Monochromatic modulation transfer function of the human eye for different pupil diameters: an analytical expression. *J. Opt. Soc. Am. A*, 11(1):246–249, January 1994.
- [107] Optotune AG. *Datasheet: EL-10-30-Series*, 2014. Update 02.07.2014.
- [108] J. Wei and L Thibos. Design and validation of a scanning Shack Hartmann aberrometer for measurements of the eye over a wide field of view. *Optics Express*, 18(2):1134–1143, January 2010.
- [109] G. Westheimer and J. Liang. Influence of ocular light scatter on the eye’s optical performance. *J. Opt. Soc. Am. A*, 12(7):1417–1424, July 1995.
- [110] F. C. Delori and K. P. Pflibsen. Spectral reflectance of the human ocular fundus. *Applied Optics*, 28(6):1061–1077, March 1989.
- [111] A. Unterhuber, B. Povazay, H. Sattmann, A. Chavez-Pirson, and W. Drexler. In vivo retinal optical coherence tomography at 1040 nm - enhanced penetration into the choroid. *Optics Express*, 13(9):3252–3258, May 2005.
- [112] S. A. Burns, S. Wu, F. Delori, and A. E. Elsner. Direct measurement of human-cone-photoreceptor alignment. *J. Opt. Soc. Am. A*, 12(10):2329–2338, October 1995.
- [113] B. Vohnsen. Directional sensitivity of the retina: A layered scattering model of outer-segment photoreceptor pigments. *Biomedical Optics Express*, 5(5):1569–1587, April 2014.

- [114] D. T. Miller, D. R. Williams, G. M. Morris, and J. Liang. Images of cone photoreceptors in the living human eye. *Vision Research*, 36(8):1067–1079, August 1995.
- [115] S. Marcos and R. Navarro. Determination of the foveal cone spacing by ocular speckle interferometry: limiting factors and acuity predictions. *J. Opt. Soc. Am. A*, 14(4):731–740, April 1997.
- [116] N. López-Gil and P. Artal. Comparison of double-pass estimates of the retinal-image quality obtained with green and near-infrared light. *J. Opt. Soc. Am. A*, 14(5):961–971, May 1997.
- [117] L. Diaz-Santana and J. C. Dainty. Effects of retinal scattering in the ocular double-pass process. *J. Opt. Soc. Am. A*, 18(7):1437–1444, July 2001.
- [118] J. C. Dainty. The statistics of speckle patterns. In E. Wolf, editor, *Progress in Optics XIV*, pages 1–46, 1976.
- [119] A. Pintó, F. Laguarda, R. Artigas, and C. Cadavall. Non-contact measurement of aspherical and freeform optics with a new confocal tracking profiler. In *Optical Fabrication, Testing, and Metrology IV*, volume 8169, page 81690V, September 2011.
- [120] J. A. Martínez-Roda, M. Vilaseca, J. C. Ondategui, A. Ginner, F. J. Burgos, G. Cardona, and J. Pujol. Optical quality and intraocular scattering in a healthy young population. *Clinical and Experimental Optometry*, 94(2):223–229, June 2010.
- [121] R. Navarro. Incorporation of intraocular scattering in schematic eye models. *J. Opt. Soc. Am. A*, 2(11):1891–1894, November 1985.
- [122] S. Haykin and B. Van Veen. *Signals and Systems*. Wiley, second edition, 2002.
- [123] N. López-Gil, I. Iglesias, and P. Artal. Retinal image quality in the human eye as a function of the accommodation. *Vision Research*, 38(19):2897–2907, October 1997.
- [124] H. C. van de Hulst. *Light Scattering by Small Particles*. Dover Publications, 2012.
- [125] C. Beckman, O. Nilsson, and L.-E. Paulsson. Intraocular light scattering in vision, artistic painting, and photography. *Applied Optics*, 33(2):4749–4753, July 1994.
- [126] L. Tsang, J. A. Kong, and K.-H. Ding. *Scattering of Electromagnetic Waves: Theories and Applications*. John Wiley and Sons, 2000.

- 
- [127] M. J. Costello, S. Johnsen, K. O. Guilliland, C. D. Freil, and W. C. Fowler. Predicted light scattering from particles observed in human age-related nuclear cataracts using mie scattering theory. *IOVS*, 48(1):303–312, January 2007.
- [128] F. Sanàbria, M. Aldaba, Díaz-Doutón, C. E. García-Guerra, and J. Pujol. Technical improvements applied to a double-pass setup for performance and cost optimization. *Optical Engineering*, 53(6):061710, June 2014.
- [129] D. P. Kelly, J. E. Ward, U. Gopinathan, and J. T. Sheridan. Controlling speckle using lenses and free space. *Optics Letters*, 32(23):3394–3396, December 2007.
- [130] C. C. Yu, I. Matsubara, and W. J. Dallas. Speckle noise reduction for digital holography using longitudinal shifting. In *Biomedical Optics and 3-D Imaging*, page DM4C.4. Optical Society of America, 2012.
- [131] C. E. García-Guerra, M. Aldaba, M. Arjona, and J. Pujol. Speckle reduction in double-pass retinal images using variable-focus lenses. *J. Eur. Opt. Soc.-Rapid*, 10(0):15001, January 2015.
- [132] H. M. Escamilla, E. R. Méndez, V. Ruiz-Cortés, and J. A. Landgrave. Speckle contrast in the diffraction field of weak and strong diffusers in the presence of spherical aberrations. *Optics Communications*, 313(0):195–203, October 2014.
- [133] D. Li, P. Kelly, and J. T. Sheridan. Three-dimensional static speckle fields. Part I. Theory and numerical investigation. *J. Opt. Soc. Am. A*, 28(9):1896–1903, September 2011.
- [134] D. Kang, E. Clarkson, and T. D. Milster. Effect of optical aberration on Gaussian laser speckle. *Optics Express*, 17(5):3084–3100, March 2009.
- [135] G. E. Healey and R. Kondepudy. Radiometric CCD Camera Calibration and Noise Estimation. *IEEE Transactions on Pattern Analysis and Machine Intelligence*, 16(3):267–276, March 1994.
- [136] A. W. Lohmann and D. P. Paris. Influence of longitudinal vibrations on image quality. *Applied Optics*, 4(4):393–397, April 1965.
- [137] L. Thibos, R. A. Applegate, J. T. Schwiegerling, and R. Webb. Standards for reporting the optical aberrations of eyes. In *Vision Science and its Applications*, page SuC1. Optical Society of America, 2000.